University of Nevada, Reno

Electrochemically Controllable Biomimetic Actuator

A dissertation submitted in partial fulfillment of the
requirements for the degree of Doctor of Philosophy in
Mechanical Engineering

by

Doyeon Kim

Dr. Kwang J. Kim/Dissertation Advisor

December, 2006

University of Nevada, Reno
Statewide · Worldwide

THE GRADUATE SCHOOL

We recommend that the dissertation
prepared under our supervision by

DOYEON KIM

Entitled

Electrochemically Controllable Biomimetic Actuator

be accepted in partial fulfillment of the
requirements for the degree of

DOCTOR OF PHILOSOPHY

Kwang J. Kim, Ph.D., Advisor

Alan Fuchs, Ph.D., Committee Member

Shen-Yi Luo, Ph.D., Committee Member

Yanyao Jiang, Ph.D., Committee Member

Benjamin T. King, Ph.D., Graduate School Representative

Marsha H. Read, Ph. D., Associate Dean, Graduate School

December, 2006

ABSTRACT

Ionic Polymer-Metal Composites (IPMCs) are soft electroactive polymers based upon ion-exchange membranes. IPMC actuators are capable of operating in both water and air environments. The main objectives of this research are: 1) to investigate the fundamental issues regarding the actuation mechanism in connection with the relaxation problem associated with IPMCs; 2) to attain improved performance of an IPMC as an effective actuator; 3) to explore a new feature of IPMC operation for further applications.

A number of experimental techniques, including electrochemical and electromechanical analyses, were performed to investigate the actuation characteristics of IPMCs. The resulting data revealed that the relaxation phenomena of the IPMC actuators are primarily caused by the overpotential of the surface electrodes. Overpotential values of approximately +1 V were clearly noted for the platinum-IPMC. As an alternative solvent of IPMC, a room temperature ionic liquids (RTIL) was investigated. When an IPMC was solvated with an effective RTIL, it not only showed a much improved bending motion but also seemingly eliminated the relaxation phenomena. Within appropriate operating conditions, unwanted electrochemical reactions on the surface were not observed in the RTIL system. As a result, the efficiency of IPMCs in an RTIL system was significantly improved because the input power was mostly used in actuation. Further, a surface modification technique provoking the self-oscillatory motion of IPMCs was investigated. The platinum-IPMC showed a kinetically-driven oscillatory bending motion in the presence of small organic molecules under applied DC inputs. The general

behavior of self-oscillatory IPMC was highly repeatable and showed regular periodic phenomena. The self-oscillatory behavior of IPMCs under specific conditions could be a useful means to minimize the use of complex electronics in many small-scale applications.

An analytical model, which accounts for the electrochemical and electromechanical phenomena of the self-oscillatory IPMC was developed using an equivalent circuit, beam theory, and surface chemistry. The physical phenomena of the system were described in coupled differential equations. Seemingly, the model can accurately predict the self-oscillatory and non-linear behavior of the IPMC actuator.

DEDICATION

To my dear wife;

Jeeyoung Park

Her love and support is my inspiration.

ACKNOWLEDGEMENTS

First of all, I am deeply grateful to my advisor, Professor Kwang J. Kim, for his guidance and support during this work. It has been an honor and a pleasure for me to work with him. I would like to give my special thanks to Dr. Shen-Yi Luo, Dr. Benjamin T. King, Dr. Yanyao Jiang, Dr. Alan Fuchs, and Dr. Ji Su for their serving on my dissertation committee and for their valuable advice on my research.

I would like to express my deepest gratitude to Dr. Yongsug Tak for his continuous advice and encouragement. Special thanks are extended to Jongtae Lim for his encouragement. I would also like to thank Dr. Woosoon Yim, Dr. Yong-Du Jun, Dr. Joon. S. Lee, and Dr. Il-Seok Park for valuable discussions and unconditional assistance in this work. I wish to give my thanks to the members of Active Materials and Processing Laboratory who have been working with me throughout this project. Particular thanks go to Kiyoung Choe, Dr. Srinivas Vemuri, Jason Paquette, and Arun Puddipeddi for their friendship and kind help which made my research a lot easier. In particular, I appreciate the partial financial support from the Doctoral Fellowship Program of the KOSEF.

Above all, I would like to thank my family and my wife's family for their support and emotional encouragement, which led to my decision to pursue the best education possible. I especially want to thank my dear wife, Jeeyoung Park, for her understanding, patience, encouragement, and unconditional love.

TABLE OF CONTENTS

LIST OF FIGURES

LIST OF TABLES

LIST OF SYMBOLS

Roman letters

a	half thickness of Nafion™
aq	aqueous phase
b	half thickness of IPMC
c	concentration
c_{mod}	modeling parameter
C	capacitance, F
C_f	quartz crystal constant, Hz/g
d	mobility coefficient, $m^2/V \cdot s$
D	diffusion coefficient, m^2/s
e	efficiency, %
E	electric potential or voltage, V
E^*	tensile modulus, Pa
E'	storage modulus, Pa
E''	loss modulus, Pa
$\vec{E}$	electric field
f	frequency, Hz
F	Faraday constant, 96,485 C/mol
F_B	blocking force, N
g	gas phase

h	thickness, m
i	current, A
I_0	exchange current density, A/m^2
j	current density, A/m^2
K	Darcy permeability
l	length, m
L	inductance, H
L_{ij}	cross coefficient
m	mass, g
M	momentum
N	ionic species flux, mol/m^2s
p	pressure, Pa
P	power, W/m^3
Q	charge, C
Q_f	flux
r	radius of curvature, m^{-1}
R	resistance, Ω
s	solid phase
S	the number of sites
t	time, s
T	temperature, ˚C
u	strain-energy density, J/m^3
U_x	measure of individual uncertainty

V	volume, m^3
w	width, m
Y	Young's modulus, Pa
z	charge number
Z	impedance, Ω

Greek letters

α	transfer coefficient, $mol/m^2 \cdot s$
δ	deflection, mm
ε	stain, %
ε'	dielectric constant
η	overpotential, V
κ	conductivity, S/m
$\kappa(t)$	curvature, m^{-1}
λ	water molecules per sulfonic group
ν	velocity, m/s
ν_p	Poisson's ratio
ρ	density, kg/m^3
σ	stress, N/m^2
σ_δ	standard deviation of the deflection
τ	time constant, s
ϕ	phase angle, °

ψ	sulfonic group per cation

Superscripts

*	active site
0	standard
TM	trademark

Subscripts

a	anode
A	actuation
ads	adsorbed
c	cathode
CO	carbon monoxide
e	electrolyte
in	input
IR	ohmic drop
max	maximum
N	Nafion™
OH	hydroxyl
out	output
Pt	platinum
rev	reverse

Abbreviations

AC	alternating current
Ag/AgCl	silver/silver chloride electrode
ASTM	American standard test methods
CA	chronoamperometry
CCD	charge-coupled device
CP	chronopotentiometry
CV	cyclic voltammetry
DC	direct current
DI	distilled
DMA	dynamic mechanical analysis
DSC	differential scanning calorimeter
EAP	electroactive polymer
EQCM	electrochemical quartz crystal microbalance
EW	equivalent weight
IEC	ion exchange capacity
IPMC	ionic polymer-metal composite
MD	machine direction
RSS	root-sum-square
RTIL	room temperature ionic liquid
SCE	saturated calomel electrode
SEM	scanning electron microscopy
TD	transverse direction

Tg	glass transition temperature
Tm	melting temperature
YP	yield point
TS	tensile strength, Pa

CHAPTER 1:

INTRODUCTION

Ionic Polymer-Metal Composites (IPMCs) have been extensively studied over the past decade. Some of the reasons why IPMCs are considered promising candidates for soft actuators are their large, electrically-induced bending strains, low power requirements, ease of processing, and mechanical flexibility that offer advantages over traditional electroactive ceramic materials [1].

Research on IPMCs as soft actuators has been conducted in two broad areas. The first of these is the study of physicochemical phenomena, where the goal is to better understand the fundamental mechanisms and various factors that control the process and to develop materials that have properties suited for the required performance characteristics. The second is the application of a device, where the goal is to create a design for various applications. The quality of the solution can be defined in many different approaches, depending on the requirements of specific applications. Although many researchers have had strong expectations for IPMCs as an actuator, there have been a number of unsolved critical issues. It is the belief in the engineering community that, despite high promise, the main reason for the vulnerable deployment of IPMCs is due to poor understanding of their actuation mechanism. Similarly, the electrochemical behavior of IPMCs have been studied less, or even overlooked, although the underlying principle for the actuation is based on electrochemical reactions. This research is intended to

provide better an understanding of IPMC behavior including performance degradation during actuation and several new findings related to them.

1.1. Overview of IPMC technology

IPMCs are electroactive polymers (EAPs) which have actuatory capabilities under low driving voltages as well as sensory capabilities under low applying forces. IPMCs deform quickly by applying a low electric field between the electrodes across the membrane. Conversely, IPMCs generate electrical signals by an applied stress [2]. The operation mechanism of IPMCs is somewhat complex in terms of its full operation and capabilities; significant progress has been made, leading to the belief that IPMCs will be capable of being used in advanced actuation and sensing applications. In 1992, the Oguro group in Japan [3] first reported that Nafion™-platinum composite bent quickly in response to a low voltage (under +1.5 V). They showed that mechanical deformation is produced when an electric field is applied across the thickness of a Nafion™. In the same time period, Sadeghipour *et al*. [4] presented experimental data for a Nafion™-based accelerometer as a vibration sensor. They fabricated a wafer-like cell that applied pressure across an IPMC, and they measured the voltage output. After the first discovery of IPMCs as actuators, the primary focus of the IPMC research community has been on materials study and engineering devices since IPMCs show great potential as soft robotic actuators and artificial muscles in the micro-to-macro size range. Guo *et al*. [5] started developing an active catheter for neurosurgery based on the IPMC. Later, they developed a micropump based on the IPMC [6]. Asaka *et al*. [7] empirically derived an expression for the deflection response to a step current. Early work, using an IPMC as artificial

muscles for robotic application, was led by Shahinpoor *et al*. [8]. Abe *et al*. [9] first introduced the important concept of the influence of the counter ions in the actuation behavior of ionic polymer. They also studied the effect of the water content of Nafion™ using various cations for the actuation. Asaka *et al*. and Onish *et al*. also reported these effects [10, 11]. Asaka and Oguro [12] discussed the bending of the polyelectrolyte membrane-platinum composites due to electric stimuli and presented a theory on actuation mechanisms in IPMC by considering the electro-osmotic drag term in the transport equations. Shahinpoor and Kim [13] have experimentally demonstrated that the ionic polymer actuator performance depends on the type of cation. Henderson *et al*. [14] performed an experimental frequency-domain analysis of the output voltage with a tip deflection input for a cantilevered bender. They also attempted to evaluate the suitability of ionic polymer transducers for use in near-DC accelerometers. Fujiwara *et al*. [15] developed a gold electroding technique onto Nafion™. Shahinpoor and Kim [16] developed a two-step fabrication method for platinum-IPMC. Uchiad and Taya [17] introduced a copper ion as a counter ion in the membrane and observed an enhanced deflection of the IPMC with an electrochemical oxidation of copper. Asaka and Fujiwara [18] used an anion-exchange membrane in order to clarify the response mechanism of the IPMC. The composite was found to bend toward the cathode side and the specific deflection was observed to be proportional to the amount of charge accumulated in the electrode. Lu *et al*. [19] reported that conducting polymer actuators and electrochromic devices in ionic liquids showed enhanced stability over traditional devices. Bennett *et al*. [20, 21] introduced the use of ionic liquid as a solvent for in-air operation of the IPMC.

1.2. Overview of theoretical models in IPMC

IPMC's multiphysical behavior makes the material's predictability and modeling increasingly difficult. The overall behavior of the material is still not fully agreed upon by researchers; consequently, there have been many proposed models to explain the behavior of materials based on many different parameters associated with IPMCs. Several models attempt to explain various physical behavior of an IPMC actuator. They range from equivalent circuit models, to beam theory, to micromechanics, among others [1, 2, 7, 22-31]. The proposed models have tried to quantify the forces, the deflections, and the curvatures mostly.

An empirical model of IPMC, developed by Kanno *et al*. [29], was modified by studying the step response of the actuators and was empirically modeled as a linear combination of real poles. Shahinpoor [30] proposed a mechanical model based upon an Euler-Bernoulli beam. He presented the finite curvature as a function of the arc length and time, using Hookes' law related to the equivalent moment. Similar work was reported by Bar-Cohen and Leary [1] using a model based solely upon beam theory. Enikov and Nelson [32] developed a continuum mechanical model of an IPMC. Global integral postulates were written for the conservation of mass, momentum, energy, charge, Gauss' law, and the second law of thermodynamics. Tadokoro [27] presented an actuator model of IPMC for robotic applications on the basis of physicochemical phenomena. Asaka and Oguro [12] proposed a model for the bending of IPMCs by electric stimuli and applied the model to the kinetics of the bending response. Xiao and Bhattacharya [33] presented a multi-scale approach to modeling the electro-mechanical behavior of ionic polymers. They chose to develop a mesoscopic model for the optimal design formulation

of polymers such as IPMCs. It is impossible to separate the deformation mechanism from the existing structure. Nemat-Nasser and Li [28, 34] have proposed a model to explain the transduction phenomenon within an IPMC and to predict its response, using a micromechanical model that accounts for the coupled ion transport, electric field, and elastic deformation. The model was based on the structure of the clusters within the polymer matrix. The electromechanical coupling that the Nafion™ exhibits has been investigated by several others. De Gennes *et al*. [35] first developed a linear irreversible thermodynamic relationship for charge transport and solvent transport to describe this electromechanical coupling of IPMCs. Recently, Toi and Kang [36] introduced a finite element analysis based on Galerkin's method for the two-dimensional electrochemical-mechanical behavior of IPMC beams.

1.3. Research objectives

The main objectives of this research are to interpret electrochemical and electromechanical phenomena of IPMCs, to investigate the fundamental actuation mechanism, including the relaxation problem that is caused by a back diffusion of free water that is carried with the cations to the cathode side of the actuator, and to attain improved performance of IPMCs as an effective actuator. This dissertation focuses on the following: 1) study of the underlying mechanisms of IPMC actuators with emphasis on the electrochemical reactions occurring at the electrodes via the coupled electrochemo-mechanical process; 2) characterization of the materials' performance during underwater and in-air operations; 3) the investigation of another operational advantage, a self-oscillatory manner; and 4) an engineering model of the bending behavior of an IPMC as

developed combining equivalent circuit model, beam theory, and surface chemistry to explain the self-oscillatory motion of IPMC. In order to investigate the electrochemo-mechanical characteristics of the IPMCs, various experimental methods, including a) electrical measurement, b) electrochemical interpretation, and c) mechanical analyses, were carried out in water and air environments. The use of ionic liquids as alternative solvents was also investigated. In order to predict the physical behavior of the IPMC, it is necessary to develop an appropriate model for the actuation characteristics of the IPMC. This model could be a suitable one for actuator applications and for the design of a new IPMC actuator that deforms to a desired shape.

Chapter 1 of this dissertation introduces the material and recent work in the field of IPMCs. Fundamentals of IPMCs, their components, and actuating mechanisms as a background for the subject of this research are reviewed in Chapter 2. Experimental details for IPMCs, including material preparations and testing methods, are described in Chapter 3. The electrochemical and electromechanical characteristics of IPMC are discussed in Chapter 4. Underwater and in-air operations of IPMC actuators are investigated in Chapter 5. In addition, one of the shortcomings, *i.e.* the relaxation phenomena of IPMC actuation, is investigated in Chapter 5. In order to improve the actuation performance of IPMCs and to operate them in the air environment, ionic liquid as a solvent of IPMC is also studied in chapter 5. An intriguing new feature of the IPMC, "rhythmic motion," is introduced in Chapter 6. The oscillatory behavior of IPMC is investigated in the presence of small organic compounds. Numerical modeling and computational simulation are presented in Chapter 7. Finally, the main results and

conclusions are summarized and recommendations for future study of IPMCs through experimental results are made in Chapter 8.

CHAPTER 2:

IONIC POLYMER-METAL COMPOSITE

General introduction of the Ionic Polymer-Metal Composites (IPMC) and prior works was presented in Chapter 1. This chapter is devoted to the components and their mechanisms related to the actuation of IPMCs. Important elements of an IPMC are the ion-exchange membrane, the electrodes, and the solvent. Accordingly, prior efforts on the fundamental properties/principles of these materials are also reviewed.

2.1. Polymer electrolyte as a base material

Polymer electrolyte is a critical component of an IPMC, one that affects the design, operating conditions, and voltage losses. The main requirements for high performance membranes in the IPMC application are chemical stability in the required solvents, sufficient mechanical strength, low electrical conductivity, high selectivity to the desired ionic species, and high ion-exchange capacities (IECs). Note that Nafion™ 117 has 0.89 of IEC [37, 38]. Nafion™, as one polymer electrolyte, satisfies the above requirements. Moreover, Nafion™ has been extensively used in electrochemical cells, including electrolytic cells and galvanic cells, due to outstanding chemical, mechanical, and thermal properties [39]. Yeo and Eisenberg [40] reported that the glass transition temperature (Tg) of Nafion™ is approximately 111˚C. Thus, the mechanical stability is compromised at elevated temperatures. Because of these properties, Nafion™ has been

widely used as the base material of IPMCs. From its development by DuPont in the 1960s, it has etched applications in liquid and gas separations, fuel cells, and the chlor-alkali industries. Nafion™ has ionic properties [38, 41], which were created by adding sulfonic acid groups, a chemical with very strong ionic properties, into the bulk polymer matrix. The hydrophilic sulfonic acid groups are randomly dispersed within Nafion™ and allow Nafion™ to work as a cation-exchange membrane [42]. The amount of ionic groups in the membranes is conventionally expressed in terms of the equivalent weight (EW) of the polymer. EW is defined as the weight of polymer which will neutralize one equivalent of base. The EW is inversely proportional to the IEC according to the following relationship [43]:

$$EW = \frac{1,000}{IEC} \quad \left(IEC = \frac{V \cdot M}{m_{dry}} \right) \tag{2.1}$$

where IEC is given in terms of milliequivalents per gram (meq/g) of polymer; V is the added titrant volume at the equivalent point in ml; M is the molarity of the titrant; and m_{dry} is the dry mass of the sample in g.

As for the sulfonate membrane, the range of EW for electrochemical applications is 1,100 to 1,350, corresponding to 0.741 ~ 0.909 meq/g [44]. The researchers in the field of polymer electrolytes [45] reported that the properties of polymer electrolytes are strongly influenced by the EW, water content, nature of solvent, exchanged cations, and temperature. Good wettability is essential for membranes that serve as separators in electrochemical cells. While fluorocarbon polymers are generally known to be quite

hydrophobic substances, Nafion™ is certainly an exception. Nafion™ absorbs water rapidly even at room temperature and the diffusion of solvents in Nafion™ is very rapid. For diluted electrolytes, Nafion™ is one order of magnitude smaller than the self-diffusion of water. The diffusion rate decreases with increasing concentration due to the dehydration of the membrane [44]. Nafion™ has a microphase-separated structure with a hydrophobic perfluorinated region (the backbone) interspersed with ion-rich hydrophilic domains. Nafion™ swells in the presence of water because the latter is taken up by these ion-rich domains. When swollen by water, Nafion™ undergoes phase separation, *i.e.* clustering, on a supermolecular structure [46]. Increasing water clusters in swollen membranes aids the proton transport phenomena; the water clusters are more easily transported or dragged across the membrane by the movement of cations [47]. When the Nafion™ membranes are swollen, it has been pictured that hydrophobic zones around the fluorocarbon backbones and hydrophilic zones around the fixed ionic groups coexist. Therefore, the ionic groups attract water and can move water under an electric voltage though nanoscale pores and channels where ions, along with water, migrate within the polymer matrix. The pore structure of Nafion™ was explored by Divisek *et al*. [48] using a thermodynamic method of standard porosimetry. Their measurements showed that there is a wide range of pore sizes in Nafion™ with an average value on the order of 2 nm. The general chemical formula of Nafion™ is shown in Figure 2.1. It has hydrophobic (-CF_2-CF_2-) and hydrophilic (-SO_3^-) regions in its polymeric structure. The index x, y, and z varies for commercially-available Nafion™. For example, a Nafion ™ of 1,100 EW with x=6.5 is Nafion™ 117 [8].

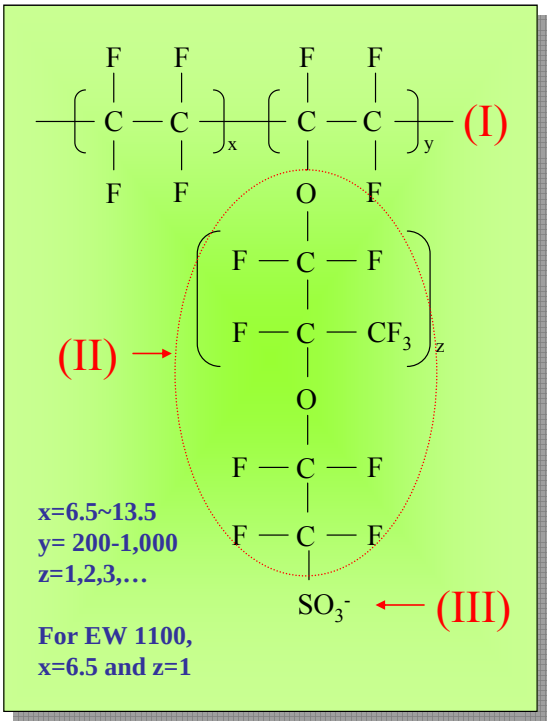

(a)

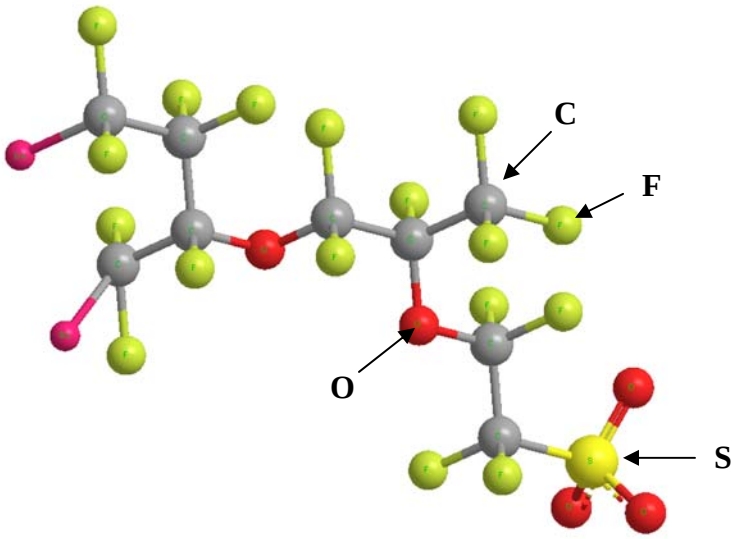

(b)

Figure 2.1. The general chemical formula (a) and three-dimensional structure (b) of Nafion™ [8].
*Note that (I) is hydrophobic part; (II) and (III) are hydrophilic part.

High ionic conductivity at the current densities typically required in IPMCs is one of the key parameters for attaining a high performance. The conductivity of a dried membrane is several orders of magnitude lower than a fully saturated membrane. The ionic conductivity in the membrane is determined by the product of ion mobility and ion concentration in the aqueous phase of the membrane. Thus the integral and local water content, commonly expressed as λ= number of H_2O/SO_3H, is of extreme importance for the membrane conductivity. The number of water molecules carried through the membrane per cation is a central factor in determining the performance of IPMCs. It is reported that dried Nafion™ with an EW of 1,100 g/mol H^+ can absorb as much as 22 water molecules per sulfonic group (λ= 22) [49]. The specific conductivity increases by nearly an order of magnitude with the increasing water content. The protonic conductivity of Nafion™ is 0.0316 S/cm (almost independent of temperature) and the specific conductivity of a fully hydrated Nafion™ is about 0.10 S/cm at 25˚C, 0.12 S/cm at 40˚C, and 0.20 S/cm at 80˚C [50]. These high conductivities provide the basis for the high efficiency and improved response time achievable in IPMCs. The Nafion™ 117 used in an IPMC contributes only 0.2 Ω/cm^2 to cell resistance (voltage loss of only 50 mV at 1 A/cm^2) [51], if the water level can be sustained at full hydration through the thickness of the membrane. In addition, Nafion™ has the lowest diffusion coefficient for gases such as oxygen and hydrogen and still allows the cations to diffuse. A decrease of the resistances and increase of the capacitances can be understood in terms of ionic conductivity and the dielectric constant [52]. Paddison *et al*. measured the dielectric constant of the Nafion™ membrane as a function of water content [53]. They found that the dielectric constant of the Nafion™ increases with increasing hydration and decreases

with increasing frequency. The dielectric constant of dried Nafion™ was found to be 4 which compares to a literature value of 2.05 for the pure Teflon™ [54]. Note that it is known that free water has a dielectric constant of 78.85 at room temperature [55] and this value can be reduced by an order of six for hydrated water bound to ions in the solvents [52]. Dielectric constant of Nafion™ 1100 as a function of membrane water content is shown in Table 2.1.

Table 2.1. Dielectric constant of Nafion™ as a function of water content [53] .

Water vapor activity	Water content	Dielectric constant (ε')
0.964	13	20
0.748	6	13
0.414	3	8
0.139	2	5
0	1	4

The difference between the water uptake of Nafion™ 117 from liquid and vapor phases has been attributed by Zawodzinski *et al.* [49] to differences in the adsorption processes in liquid water and water vapor. They suggest that all the pores are filled by the liquid, whereas water uptake from the vapor phase relies on capillary condensation, which is hindered by the hydrophobic surface of the Nafion™ materials.

The early work of Yeo and Eisenberg [40] reported the existence of ion clustering in perfluorosulfonate membranes. This proposal was further supported by Gierke and Hsu [56, 57] with X-ray diffraction studies on hydrolyzed Nafion™. Ion clusters are commonly observed in the ionized forms of the perfluorinated membranes. This work culminated in a microstructure model where the morphology of the system was asserted to be an inverted micelle with the sulfonic acid groups forming hydrated clusters embedded in the fluorocarbon phase with diameters of 40 ~ 50 Å. The size of the clusters appears to be larger for the sulfonate than for carboxylate membranes. The size increases in the order H^+, Na^+ and Cs^+ and decreases with increasing number of functional groups per chain and with increasing temperature [40, 44]. One interesting feature is the cation dependency of water content in Nafion™, in general, $H^+ > Li^+ > Na^+ > K^+ > Cs^+$ [58]. This can also be interpreted by their moduli, $H^+ < Li^+ < Na^+ < K^+ < Cs^+$. Physicochemical and other properties of Nafion™ 117 used in this study are summarized in Table 2.2.

Table 2.2. Physicochemical and other properties of Nafion™ 117.

Properties	Value	Reference
Fully dried thickness, mm	0.178 ~ 0.183	[38, 51]
Fully hydrated thickness, mm	0.200	[51]
Water uptake, % water	35-38	[38, 51]
Basis Weight, g/m^2	360	[38]
Area resistance, Ω/cm^2	0.2 ~ 0.25	[51]
Density, g/cm^3	2.0	[38]
Conductivity, S/cm	0.083 ~ 0.1	[38, 51, 59]
Average pore sizes, nm	2	[48]
H_2O/SO_3H (λ)	21 ~ 22	[50, 59]
$[SO_3^-]/M$ (ψ)	1.05	[59]
Ion-exchange capacities, meq/g	0.741 ~ 0.89	[38, 44]
Dielectric constant (ε')	4	[53]
Tensile Modulus, MPa 50% RH, 23˚C water soaked, 23˚C	 249 114	[38]
Tensile Strength, max, MPa 50% RH, 23˚C water soaked, 23˚C	 43 in MD*, 32 in TD** 34 in MD, 26 in TD	[38]
Elongation at Break, % 50% RH, 23˚C water soaked, 23˚C	 225 in MD, 310 in TD 200 in MD, 275 in TD	[38]

* MD: machine direction, ** TD: transverse direction

2.2. Electrocatalyst as a conductor

Electrocatalysis may be defined as the acceleration of an electrode reaction by a substance that is not consumed in the overall reaction. The substance is generally the catalytically-active electrode surface; although, to a lesser extent, the influence of the electrolyte solution may also require consideration. Reaction rates varied with the different electrodes due to their catalytic activities and overpotentials of specific reactions. The main requirement for high catalytic activity is a large surface (porosity). The reactants are adsorbed at the catalyst surface and react at the interface. The IPMCs were deposited with a number of different metals including nickel, copper [60], silver [61, 62], gold [15, 63, 64], iridium [65], palladium [66], iron [67, 68], ruthenium oxide [69], etc. Formation of cadmium sulfide clusters within Nafion™ membranes has been reported [70]. As electrocatalysts in the electrolyte solution with the reactants, precious metals tend to possess higher activity and they operate at mild conditions. Because of this property, platinum-group metals are the most widely used electrocatalyst material for IPMC's conductors. Platinum and gold as electrode materials of IPMCs are still the only catalysts that provide stable, low overpotential, and acceptable reactions in aqueous environment. Selectivity for the wanted reaction is a prime requirement for the electrocatalyst of IPMCs to avoid unwanted reactions which do not affect actuation.

The hydrogen evolution reaction is very important in the understanding of electrode reactions [71] and in the actuation in a hydrated IPMC.

In acid solution the overall reaction is the following:

$$2H^{+}(aq) + 2e^{-} \rightarrow H_2(g) \qquad (2.2)$$

and in neutral and basic media:

$$2H_2O + 2e^- \rightarrow H_2(g) + 2OH^-(aq) \tag{2.3}$$

The absorbed hydrogen atom is formed by the reaction:

$$H^+(aq) + e^- \rightarrow H_{ads} \tag{2.4}$$

This reaction plays a key role in the mechanism and kinetics of the hydrogen evolution reaction [71]. Reduction of absorbed hydrogen atoms at the metal surface is most favored when metal-hydrogen (M-H) bonds are of intermediate strength so that the hydrogen is weakly bound to the metal during electron transfer, but not so strongly bound as to prevent the formation and escape of H_2. Figure 2.2 accounts for the vigorous hydrogen gas evolution on platinum, moderate hydrogen gas evolution on gold and copper, and for the absence of hydrogen gas formation on lead and cadmium. This graph can be useful for material choice for the IPMC. Base on this graph, platinum has better properties in IPMC applications than for gold because hydrogen ions can be absorbed and desorbed on platinum quickly.

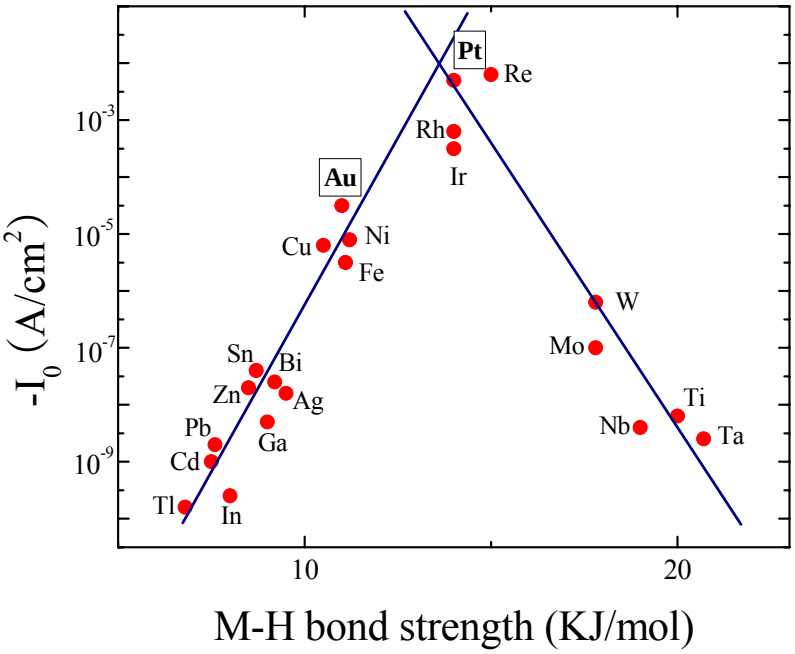

Figure 2.2. A plot of the exchange current density for hydrogen evolution *vs*. M-H (metal-hydrogen) bond strength [71].

2.3. Actuation mechanisms

The proposed mechanisms of IPMC bending from prior works [16, 28, 72] take into account the electroosmosis, the electrophoresis, and the ionic diffusion of various species. When an IPMC is fully hydrated by a solvent, the morphology of the membrane structure exhibits a nanosize pore structure [28]. The actuation mechanism of IPMC is commonly believed that hydrated cations are scattered in order to balance the negative charge of water molecules. The hydrated cations then migrate through the nanochannels toward the cathode side like electrophoresis in a fluid medium under an electric field. A new asymmetrical arrangement results in a pressure differential causing a bending stress which translates into a bending toward the anode side of the IPMC. This is due to the cathode surface expansion and anode surface contraction, simultaneously [73]. According to Verbrugge *et al.* [74], the ion transport inside of the membrane can be expressed using the following equation:

$$N_i = \underbrace{-D_i \nabla c_i}_{1} - \underbrace{z_i F d_i c_i \nabla E}_{2} + \underbrace{c_i v}_{3} \tag{2.5}$$

where N_i is the ionic species flux, D_i is the species diffusion coefficient, c_i is the molar concentration, z_i is the charge number, F is the Faraday constant, d_i is the species mobility coefficient, E is the electric potential, and v is the pore-fluid velocity. From the equation 2.5, the flux of each species through the membrane consists of three terms: 1) diffusion due to concentration gradients, 2) migration due to electric gradients, and 3) convection due to electric and pressure gradients. Thus, the actuation mechanism of

IPMC can be explained by examining the overall solvent flux within the complex network of the polymer under electric field.

A study by de Gennes *et al.* [16, 35] has presented the standard Onsager formulation on the fundamental principle of IPMC actuation/sensing phenomena using linear irreversible thermodynamics: when static conditions are imposed, a simple description of mechanoelectric effect is possible based upon two forms of transport, *i.e.* ion transport and electrophoretic solvent transport. It can be assumed that this term is water flux. The conjugate forces include the electric field and the pressure gradient. The resulting equation can be simplified as follows:

$$j = \sigma \vec{E} - L_{12} \nabla p \tag{2.6}$$

and

$$N_i = L_{21} \vec{E} - K \nabla p \tag{2.7}$$

where j is the current density, σ is the stress, $\vec{E}$ is the electric field, L_{ij} is cross coefficient, ∇p is the pressure gradient, N_i is the ionic species flux, and K is the material conductance and the Darcy permeability. A cross coefficient is usually $L_{12} = L_{21}$, experimentally measured to be of the order of 10^{-8} (m/s)/(V/m). The simplicity of the above equations provides a compact view of the fundamental principles of actuation of IPMC. Nemat-Nasser [34] has examined in some detail hydraulic, osmotic, electrostatic, and elastic forces that may affect actuation of a fully hydrated Nafion™-based IPMCs in various cation-forms. The team concluded that the electrostatic and osmotic forces within

the clusters and the elastic resisting force of the backbone ionomer basically control the actuation, with water flowing into or out of the clusters as a response to these forces. The underlying actuation mechanism for most water-saturated IPMC in cantilevered configuration placed under a positive electric field is illustrated in Figure 2.3.

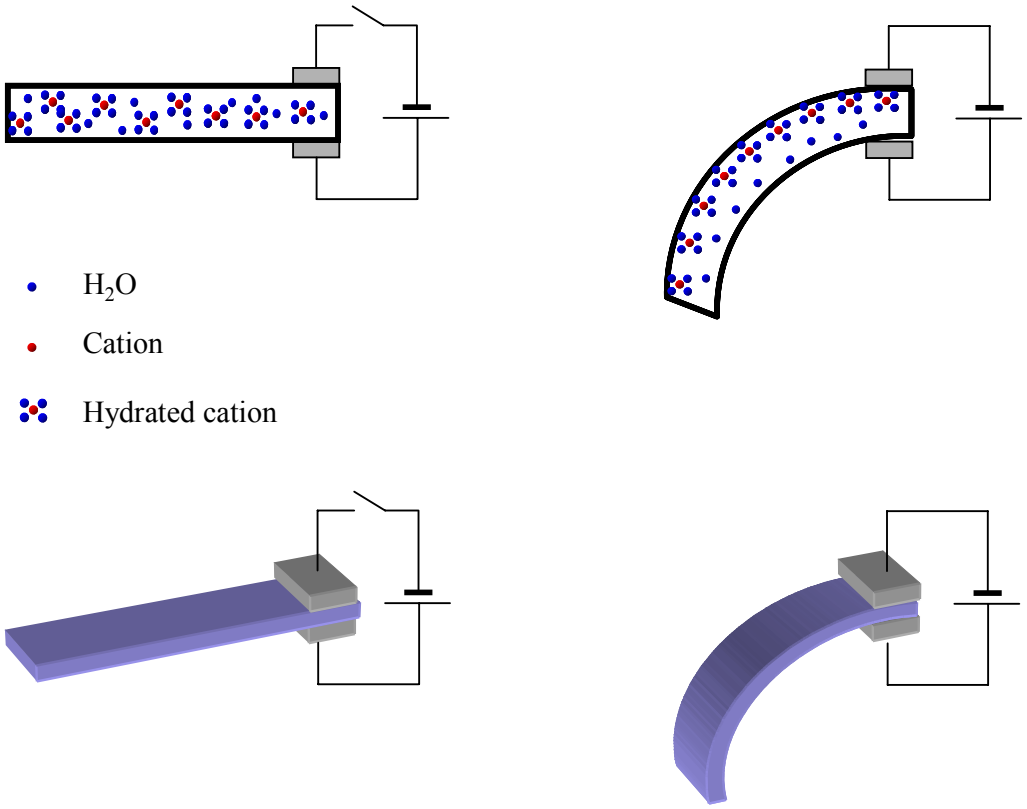

Figure 2.3. Actuation mechanism of a typical IPMC. IPMC cross-section with no applied voltage (left) and IPMC cross-section with an applied electric field (right)

CHAPTER 3:

MATERIALS AND EXPERIMENTAL METHODS

This chapter describes the materials used in this work and the experimental setups and methods used to investigate electric responses, electrochemical phenomena, and electromechanical behavior of the IPMC during actuation. The standard electrochemical techniques, including voltammetries and electrochemical impedance spectroscopy, were carried out in various environments. In addition, the blocking force and the deflection of IPMCs during actuation were measured using a load cell and an image-processing technique, respectively.

3.1. Material preparation

IPMC samples were prepared using standard electroless deposition techniques. The IPMC manufacturing techniques [16, 75-79] incorporate two distinct preparation processes: first the initial compositing process and then the surface electroding process. Due to different preparation processes, morphologies of coated metal are significantly different.

Slade *et al*. [51] reported the proton conductivity of a series of extruded Nafion™ membranes. The results showed that Nafion™ 117 has thicknesses of 0.178 mm and the thickness increased after swelling to approximately 0.20 mm. The thickness of an IPMC

sample after deposition processes were measured by a microscope. The IPMC solvated with water showed approximately 0.21 ~ 0.22 mm of thickness.

Nafion™ 117 has more durability among commercial Nafion™ membranes [80]. By reason of this property, Nafion™ 117 was used as a base material in this study. Standard IPMC samples of 40.45 mm-length × 5 mm-width were used in accordance with the golden ratio [81] (refer to Figure 3.1). The electric contact part was 7 mm-length × 5 mm-width.

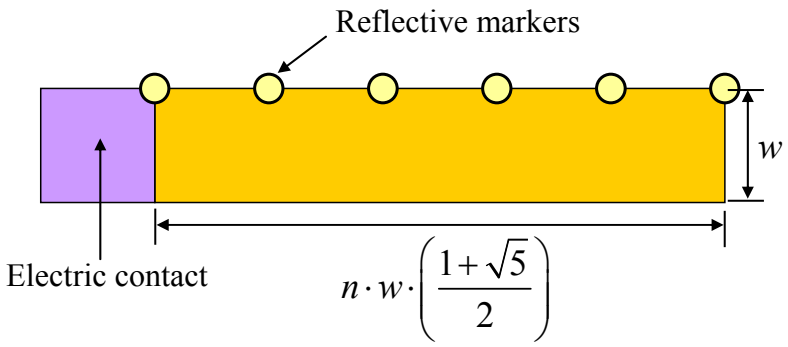

Figure 3.1. Standard IPMC sample size according to the golden ratio [81].

The Nafion™ membranes were supplied by Ion Power Inc. Pretreatment processes of Nafion™ in 3 % hydrogen peroxide (H_2O_2, Sigma-Aldrich) for elimination of organic impurities and in 0.5 ~ 1 M sulfuric acid (H_2SO_4, Sigma-Aldrich) for removal of metallic impurities were performed at 80˚C prior to the deposition process. Tetraammineplatinum

(II) chloride ($[Pt(NH_3)_4]Cl_2$, Alfa Aesar) and sodium borohydride ($NaBH_4$, Sigma-Aldrich) were used for the platinum-IPMC fabrication. The Nafion™ membrane was immersed in a 10 ~ 20 mM $[Pt(NH_3)_4]Cl_2$ solution to allow $[Pt(NH_3)_4]^{2+}$ diffusion through the ion-exchange process. $NaBH_4$ was used to platinize the membrane at 40 ~ 70˚C.

Gold (III) dichloro phenanthroline and sodium sulfite ($NaSO_3$, Sigma-Aldrich) were used for the gold-IPMC fabrication in order to use cationic gold ions. Gold (III) dichloro phenanthroline was synthesized by Block's method [75]. The chemical structure of $[AuCl_2(Phen)]^+$ is shown in Figure 3.2.

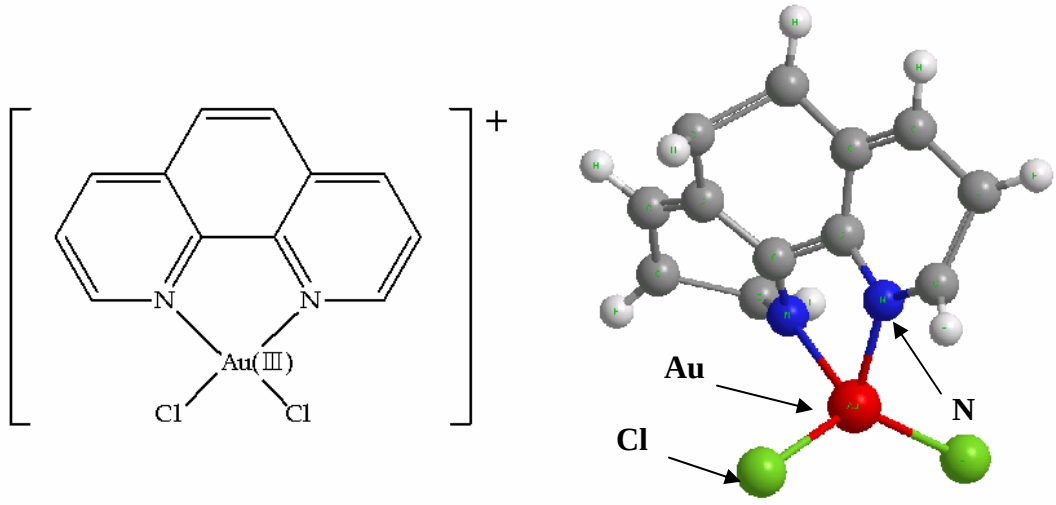

(a) (b)

Figure 3.2. Chemical formula (a) and three-dimensional structure (b) of gold (III) dichloro phenanthroline.

Nafion™ was soaked in 5 ~ 10 mM gold (III) dichloro phenanthroline solution $[AuCl_2(Phen)]^+$ and $NaSO_3$ was used to deposit gold onto the membrane at 55 ~ 65˚C. The reaction mechanisms for deposition of metals onto Nafion™ can be represented by the following chemical reactions shown in Equations 3.1 and 3.2 [8].

$$\left[Pt(NH_3)_4\right]^{2+}(aq) + 2e^- \rightarrow Pt(s) + 4NH_3(g) \tag{3.1}$$

Gold reduction can be represented by the following chemical reaction:

$$\begin{aligned}&[AuCl_2(Phen)]^+(aq) + Na_2SO_3(aq) + H_2O(aq)\\ &\rightarrow Au(s) + Phen(aq) + Cl_2(g) + Na_2SO_4(aq) + 2H^+(aq)\end{aligned} \tag{3.2}$$

Photographs of a platinum-IPMC and a gold-IPMC are shown in Figure 3.3. Prior to all experiments, pretreatment of the platinum-IPMC and gold-IPMC was performed by dozens of cyclic voltammetric curves between -0.25 V and +1.2 V (*vs.* SCE) in 0.5 M H_2SO_4 in order to ensure the absence of any residuals or impurities on the IPMC surface and, after washing it thoroughly with distilled water (DI), allowing it to stand at +0.05 V until the current became approximately zero in 0.5 M H_2SO_4. All solutions used in this study were prepared with ultra pure water (resistivity higher than 18.2 MΩ·cm) supplied by a three-stage Milli-Q (Millipore) purification system.

Figure 3.3. Photographs of a platinum-IPMC (a) and a gold-IPMC (b).

3.2. Experimental setups and methods

In general, the tensile test provides a material's mechanical properties such as the Young's modulus (Y), the tensile strength (TS), and yield point (YP). The stress-strain curve profiles obtained from the tensile test are strongly influenced by the polymer structure, molecular weight, molecular weight distribution, chain branching, degree of cross-linking, chain orientation, extent of crystallization, crystal structure, size and shape of crystal, ionic interaction, processing conditions, and temperature [82]. Mechanical properties of Nafion™ membranes and IPMCs were evaluated in accordance with the American Standard Test Methods (ASTM) D 638 and D 882 [83, 84], using a universal materials testing machine (Instron™ 5565, Canton, Massachusetts, EUA) with a 100 N load cell. The type M-III specimen of the ASTM D 638 was used for all materials due to the thickness of samples (less than 4 mm) [83]. The experiments were performed at room temperature. The crosshead was raised at the standard extension rate of 10 mm/min, placing an individual thread in tension until failure occurred. The tension test specimen geometry was selected to minimize the effects of stress concentration and premature fractures at the grips. A photograph of the testing machine in tension mode and, a photograph and an illustration of the tension test specimen are shown in Figure 3.4.

The differential scanning calorimeter (DSC) is an analytical tool that measures the heat flow to the sample pan with the heat flow to a reference pan as a function of the temperature. From this heating data, physical properties such as glass transition temperature (Tg) and melting temperature (Tm) of the polymeric materials can be

determined. In this study, DSC experiments were conducted on a DSC Q10 (TA Instruments) shown in Figure 3.5.

In addition, a dynamic mechanical analysis (DMA) experiment, another method for characterizing mechanical properties of samples was carried out using a Pyris Diamond DMA (PerkinElmer, UK). The DMA testing grip is shown in Figure 3.6. The bottom grip is fixed, and the upper grip oscillates in the vertical direction. The IPMC sample is fixed between the grips and is held in place by four screws. The mechanical characterizations with the tension test and DSC experiment were compared to the DMA data.

In general, the modulus measured in DMA is not exactly the same as the Young's modulus of the classic stress-strain curve. Young's modulus is the slope of a stress-strain curve in the initial linear region. In DMA, a Complex (tensile) modulus (E*), a storage modulus (E'), and a loss modulus (E'') are calculated from the material response to the sine wave. These different moduli allow better characterization of the material because the ability of the material to return or store energy (E'), to its ability to lose energy (E''), and the mechanical loss factor (tan *delta*), which is called damping can be examined [85]. The complex modulus can be expressed by the following equation:

$$\text{Complex(tensile) Modulus} = E^* = E' + E''i \tag{3.3}$$

The real part of the modulus is related to energy storage (E'), and the imaginary part is the loss energy (E''). The loss tangent is expressed by dividing the imaginary coefficient by the real (Equation 3.4).

$$\text{Loss tangent} = \tan delta = \frac{E^{"}}{E^{'}} \tag{3.4}$$

From DMA data, Tg can be mechanically defined either as the peak in the loss modulus or tan *delta* peak. It is important to note that the DMA is much more sensitive than the DSC technique and can easily measure transitions not apparent in other thermal methods. This sensitivity allows the DMA to detect the Tg of highly crosslinked thermosets or of thin coatings.

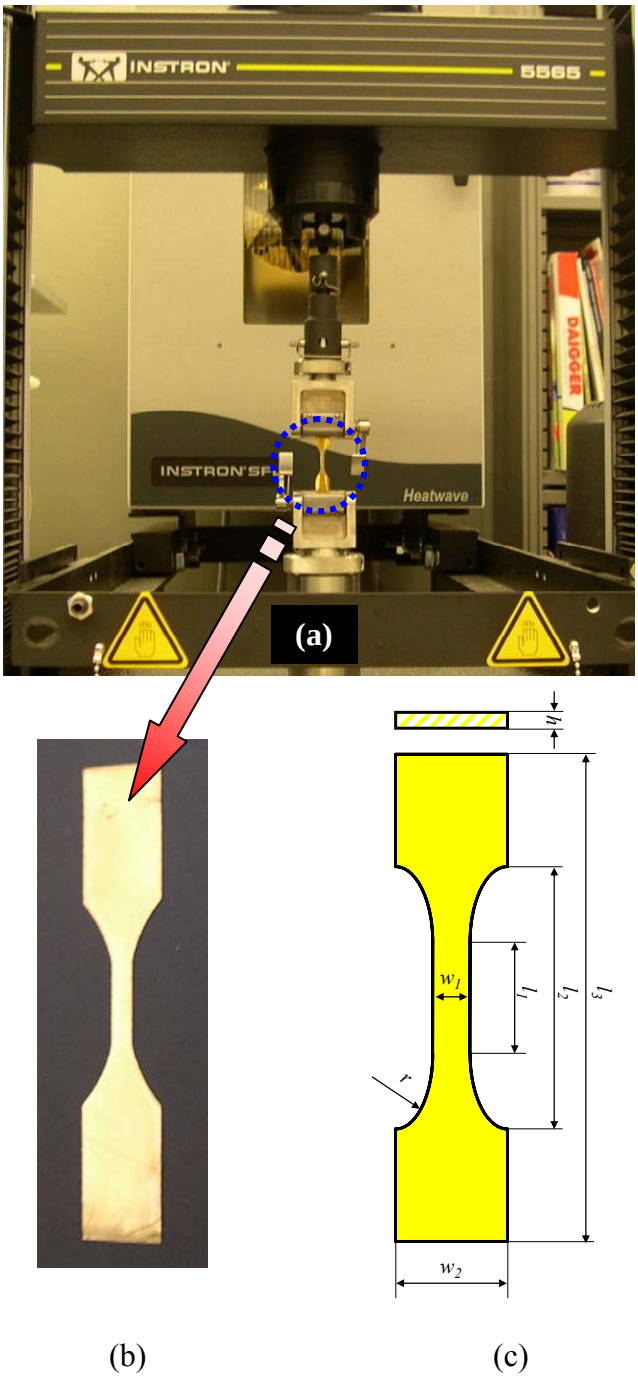

Figure 3.4. Photograph of a universal materials testing machine (Instron™ 5565) in tension mode (a) and photograph (b) and illustration (c) of the tension test specimen.
*Note that the tension test specimen was the type-III of ASTM D 638.

Figure 3.5. Photograph of a differential scanning calorimeter (TA, DSC Q10).

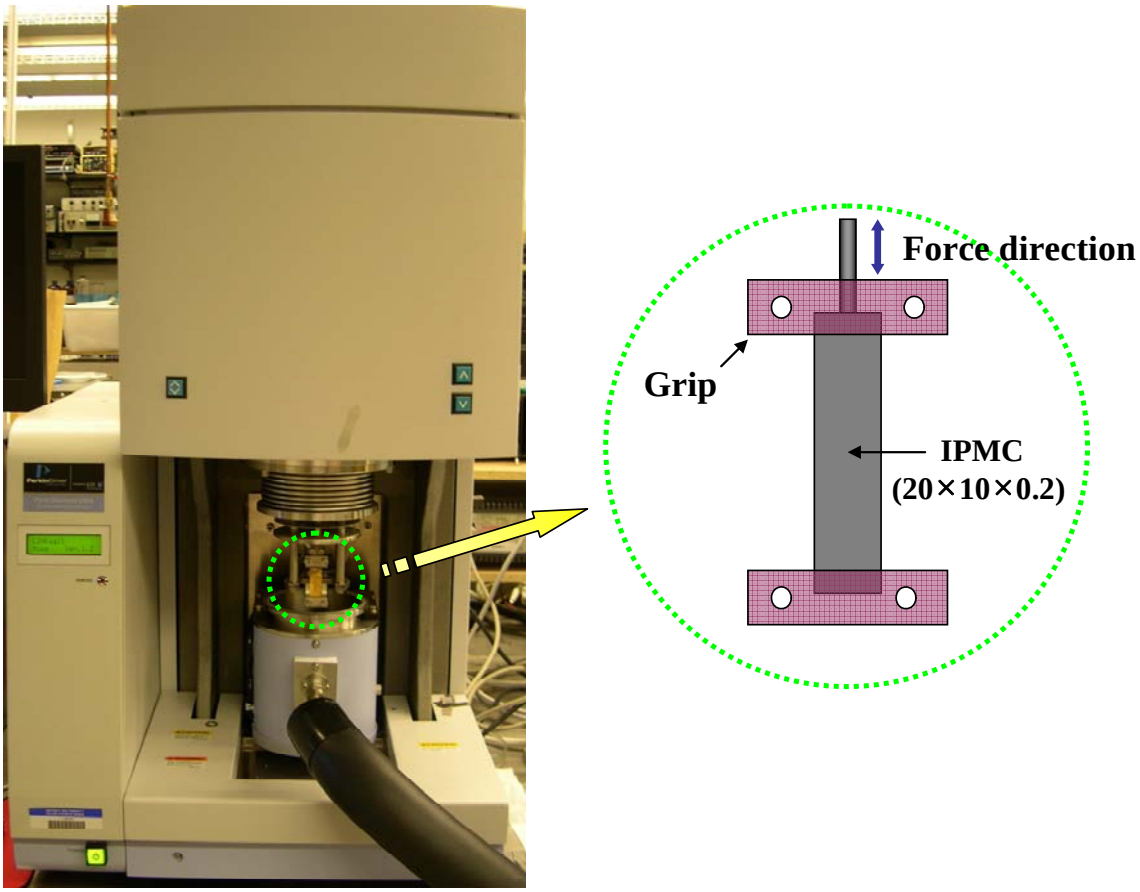

Figure 3.6. Photograph of DMA testing machine in tension mode (left) and illustration of DMA testing grip in tension mode (right).
*Note that the sample size was 20 mm-length × 10 mm-width.

The actuation tests of IPMCs for underwater and in-air operation were carried out in a conventional setup using a two-electrode system (Figure 3.7). The electrochemical experiments shown in Figure 3.8 were conducted in a conventional electrochemical cell using a three-electrode system: a reference electrode and both electrodes functioning as the working and counter electrodes, respectively. A saturated calomel electrode (SCE) or a silver/silver chloride (Ag/AgCl) electrode was used as a reference electrode in this experiment. For the three-electrode configuration, the potential is applied to the working electrode with respect to a reference electrode, and a counter electrode is used to complete the electrical circuit. Voltammograms were obtained using a potentiostat/galvanostat (Radiometer Analytical, Voltalab 80, Model PGZ402). At the same time, a high speed charge-coupled device (CCD) camera (BASLER, Model A602fc) was used for an image-processing method in order to measure bending motion. The setup for an image-processing of IPMC is shown in Figure 3.9. The camera is capable of frame rates up to 100 fps (frames per second). Six equally spaced white dots of reflective tape on the IPMC sample's edge acted as markers for tracking. After the images were acquired, those images were processed to calculate the position of each markers on the IPMC. The data points from the pixel number of the image were converted into SI units. The deflection and trajectory data of the IPMC bending motion were obtained by this technique. Additionally, the data were converted into the curvature and the strain of IPMC from the equations used in prior works [16, 17, 86] . Assuming a constant curvature throughout the IPMC strip, curvature ($\kappa(t)$) can be related to the displacement (x(t)) and the distance (y(t)) along the IPMC strip in a cantilever configuration (refer to Figure 3.10).

$$\kappa(t) = \frac{2x(t)}{x(t)^2 + y(t)^2} \cong \frac{2\sin\left[\tan^{-1}\{x(t)/y(t)\}\right]}{\sqrt{x(t)^2 + y(t)^2}} \tag{3.5}$$

where x(t) is the displacement, y(t) is the distance from fixed end.

The curvature is related to maximum tensile or compressive strains in the IPMC as

$$\varepsilon = \frac{\kappa(t) \cdot h}{2} \tag{3.6}$$

where h is the thickness of the IPMC.

Stress (σ) can be related to strain (ε) by simply using Hooke's law, assuming linear elasticity. It can be written as

$$\sigma = Y\varepsilon = Y\frac{\kappa(t) \cdot h}{2} \tag{3.7}$$

Figure 3.11 shows three different experimental setups. Figure 3.11(a) are a two-electrode system of IPMC testing in air, Figure 3.11(b) is a two-electrode system of IPMC testing in water, and Figure 3.11(c) is a three-electrode system of IPMC testing in water using a reference electrode.

The chemisorptions of intermediate species on platinum are a blocking process of surface-active sites. An electrochemical quartz crystal microbalance (EQCM) is a useful

unit for measuring mass change on the electrode. Quartz crystals, having the resonant frequency of 9 MHz, were used in this study. For the EQCM experiment the resonant frequency change for mass change can be represented by Sauerbrey equation shown in Equation 3.8 [87]:

$$\Delta f = -C_f \cdot \Delta m \tag{3.8}$$

where C_f (935.7 μHz/g) is a constant determined by the properties of the quartz crystal.

In this study, the EQCM experiments were carried out by a frequency analyzer (Seiko EG&G, Model QCA 917). A schematic diagram of an electrochemical half-cell with an EQCM unit is shown in Figure 3.12.

The blocking forces of IPMC were measured in air using a load cell (Transducer Techniques, Model GSO series). The IPMC sample is attached at one end to the load cell while the other end is placed at the contact platinum plate, forming forceps-like jaws. The blocking force of the IPMC was measured using a 10 g-load cell with zero tip displacement. Figure 3.13 shows a setup for the blocking force measurement.

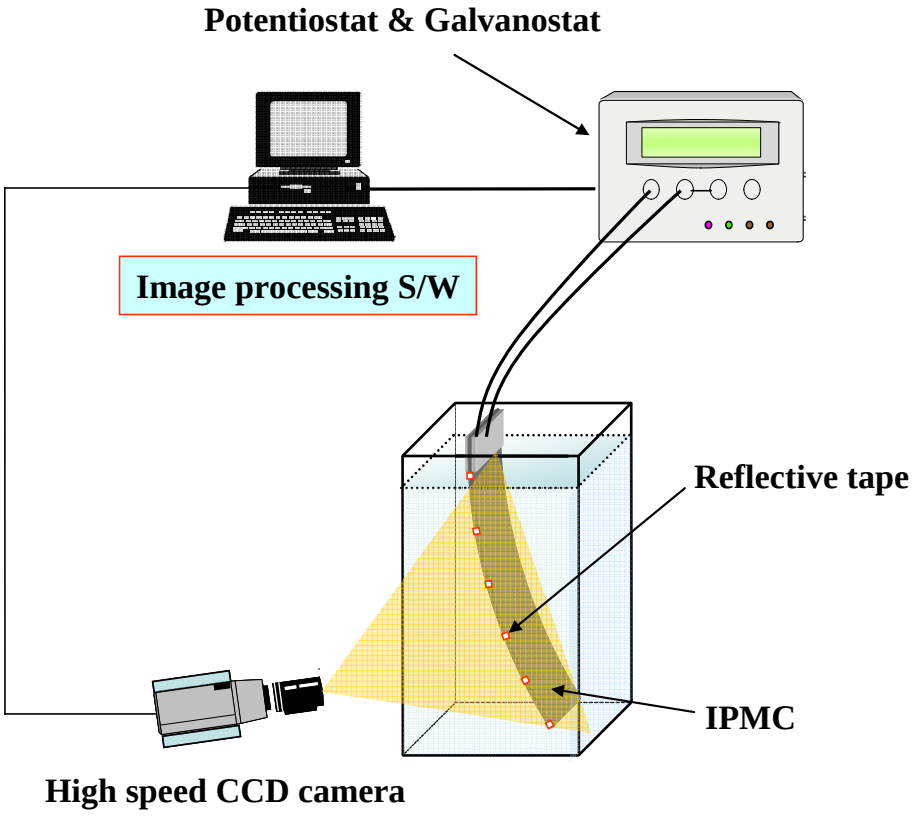

Figure 3.7. Schematic diagram of an experimental setup for actuation testing in aqueous environment.

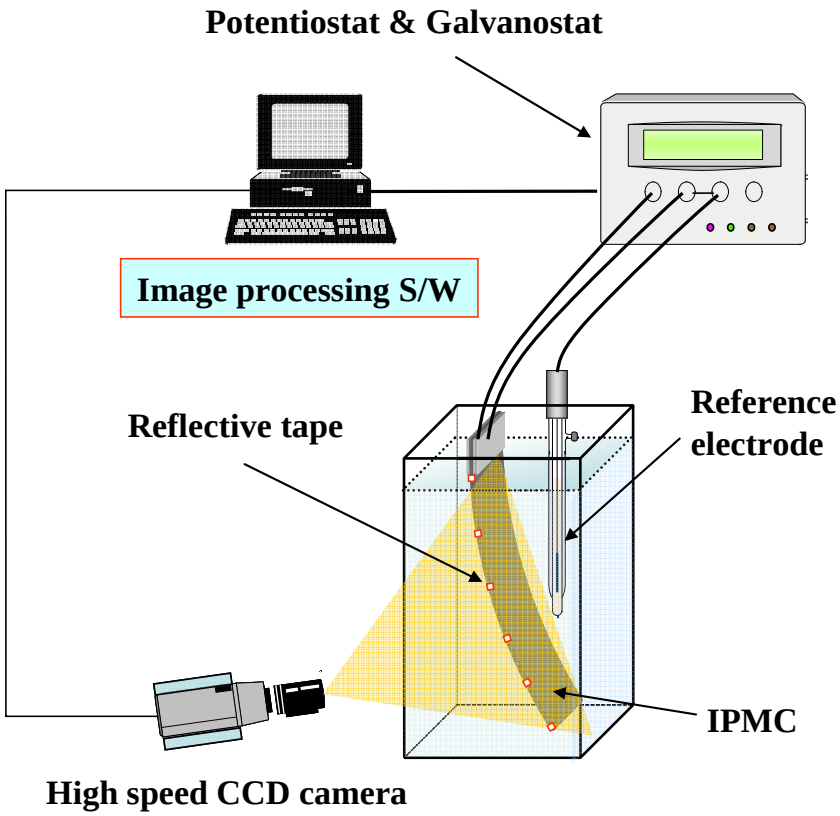

Figure 3.8. Schematic diagram of an experimental setup for electrochemical and electromechanical analyses.

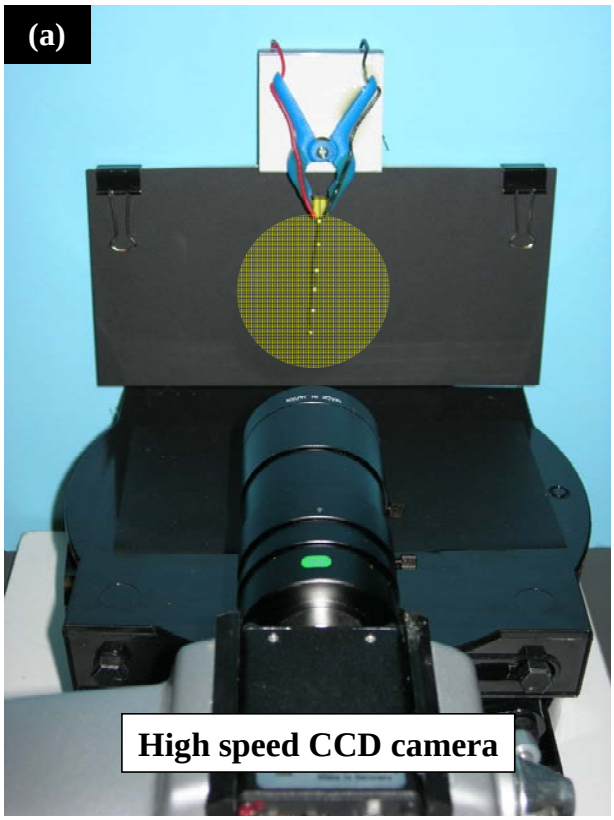

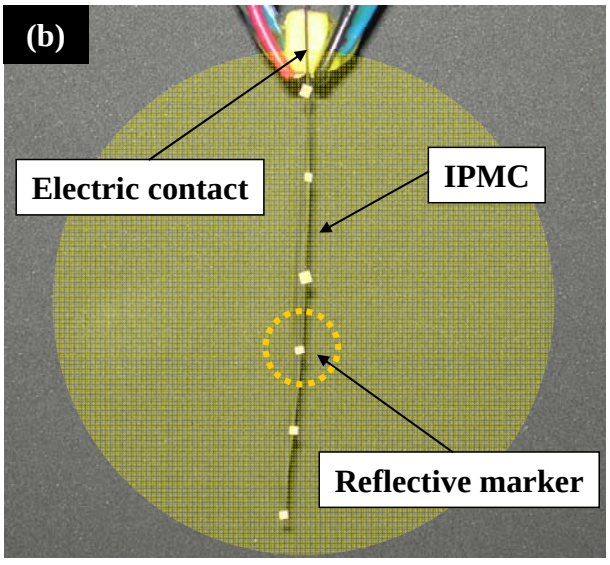

Figure 3.9. Photographs of the image-processing setup (a) and a close-up view (b) for the motion analysis of IPMC.

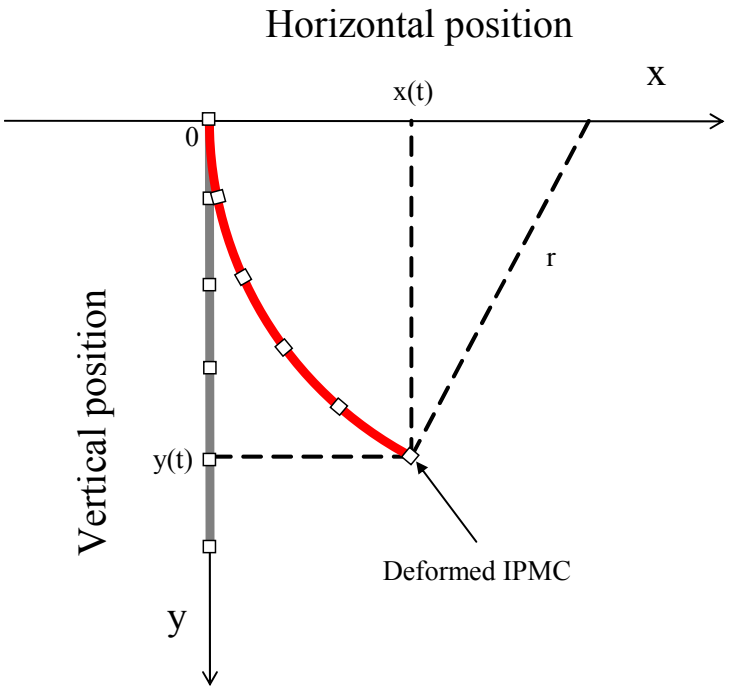

Figure 3.10. Calculation of the bending curvature of IPMC.

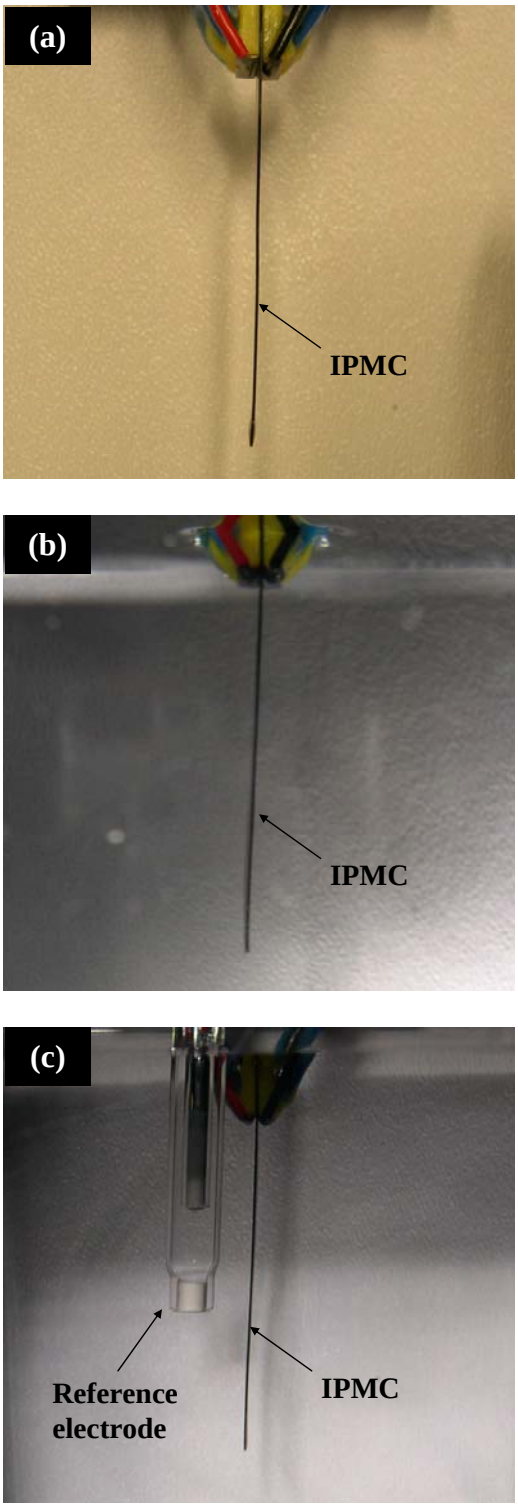

Figure 3.11. Photographs of experimental setups: two-electrode system for in-air operation (a), two-electrode system for underwater operation (b), and three-electrode system for electrochemical analyses (c).

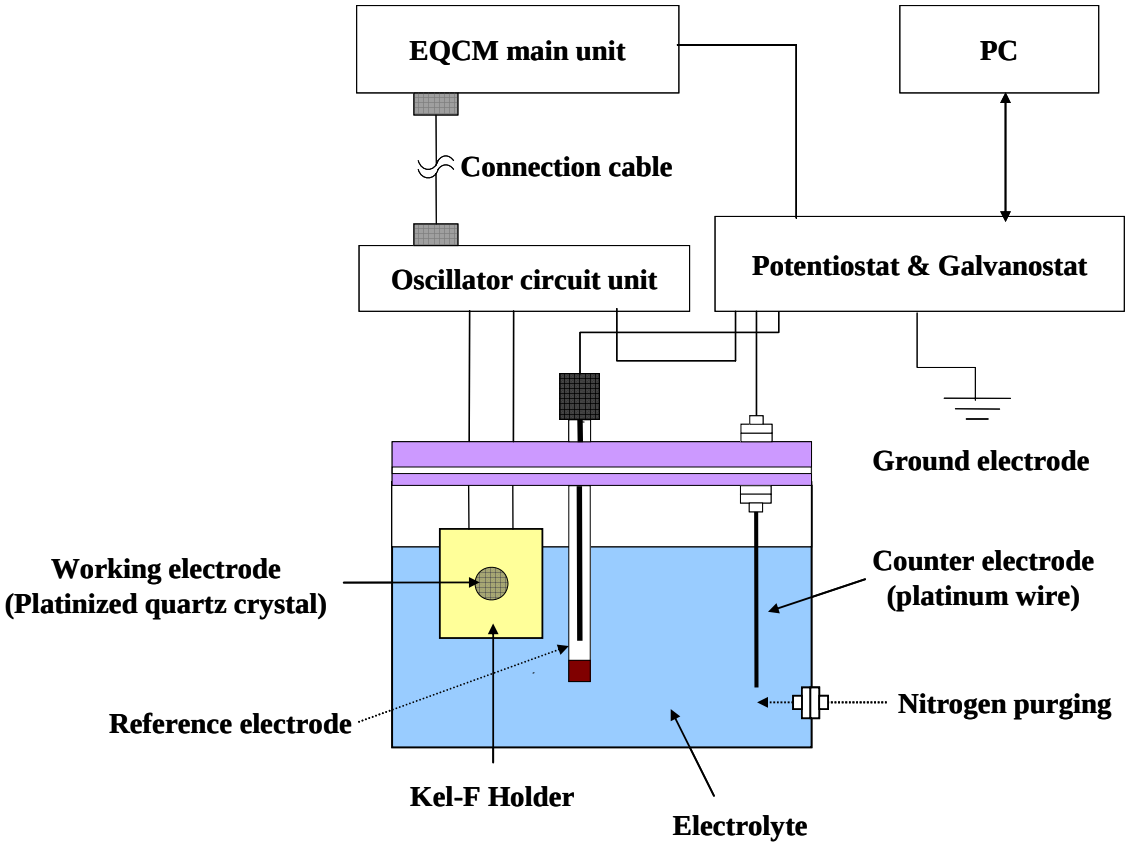

Figure 3.12. Schematic diagram of an electrochemical half-cell with an EQCM unit.

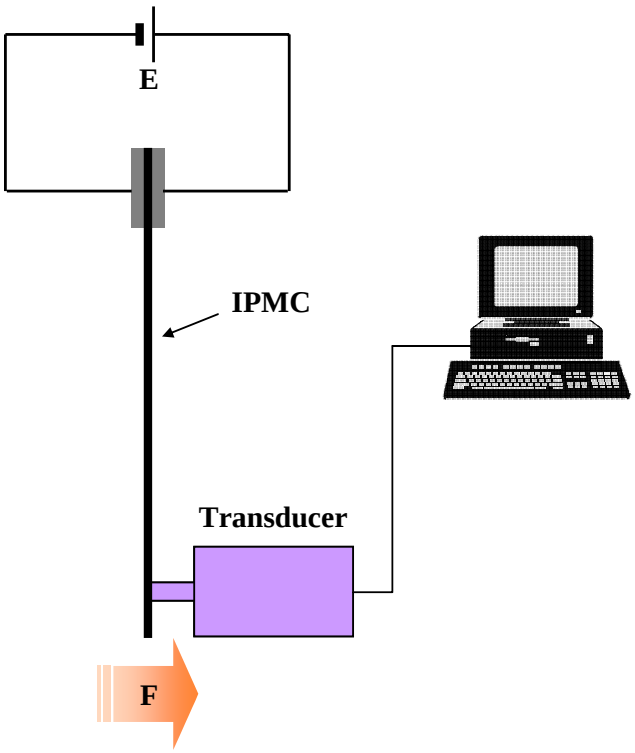

(a)

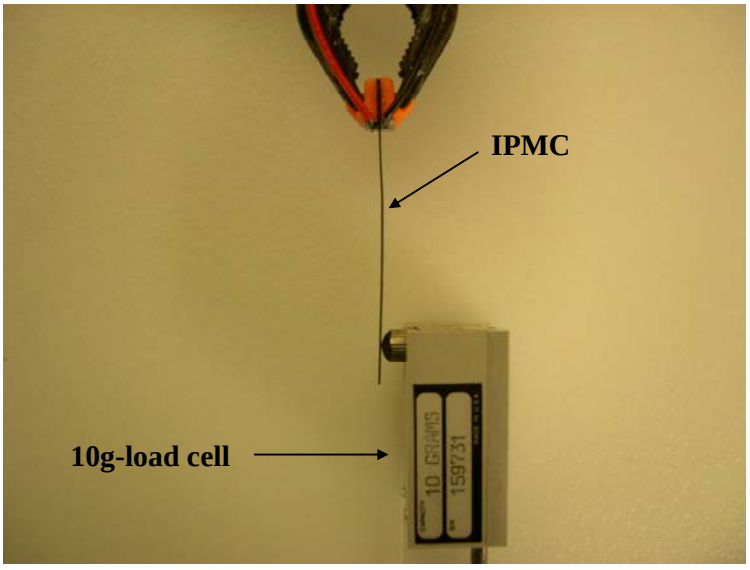

(b)

Figure 3.13. Schematic diagram (a) and photograph (b) of experimental setup for blocking force measurement in air.

CHAPTER 4:

PHYSICOCHEMICAL INVESTIGATION OF IPMC

This chapter is devoted to the evaluation of fundamental electrochemical and electromechanical experiments with IPMC during actuation. Four cases that are expressed: 1) surface morphological, 2) mechanical and thermal, 3) electrochemical, and 4) electromechanical analyses of IPMC, using the major techniques as described in Chapter 3.

4.1. Surface morphological properties

Microstructural characteristics of the IPMCs were examined using a scanning electron microscope (SEM). Surface-morphological images of the platinum-IPMC and gold-IPMC samples shown in Figure 3.3 were taken at the Korea Institute of Ceramic Eng. & Tech. The SEM images (Figure 4.1 and Figure 4.2) show that the platinum surface has microcracks on the surface, but the gold surface does not have any microcracks. These morphologies can be influenced by the deposition rate and hydrogen evolution during the coating process. However, these tessellated shapes are not believed to have any detrimental effect on the performance of the IPMCs [88]. Both platinum and gold surfaces are formed by a porous structure, as shown in Figure 4.1(c) and Figure 4.2(c). It is believed that these porous structures can have an effect on the catalytic activity of the materials, *i.e.* actuation performance.

A four-point probe (Bridge Technology, Model SRM-232-100) was also used to measure the surface resistivity of the samples. The probe has a resolution of 0.04 Ω/sq. This method practically eliminates measurement errors due to contact resistances between the electrodes and the sample [89]. The measurement was performed by making four separate electrical connections to a sample and driving an electric current through two of these connections while monitoring the corresponding electric potential at the other two connections. The surface resistivities of each sample were measured by the probe. As a result, the platinum-IPMC showed approximately 2 Ω/sq and the gold-IPMC showed approximately 1 Ω/sq. Based on the morphological observation and the four-point probe measurement, the surface resistivity of IPMC was influenced by the particle size of the electrode materials.

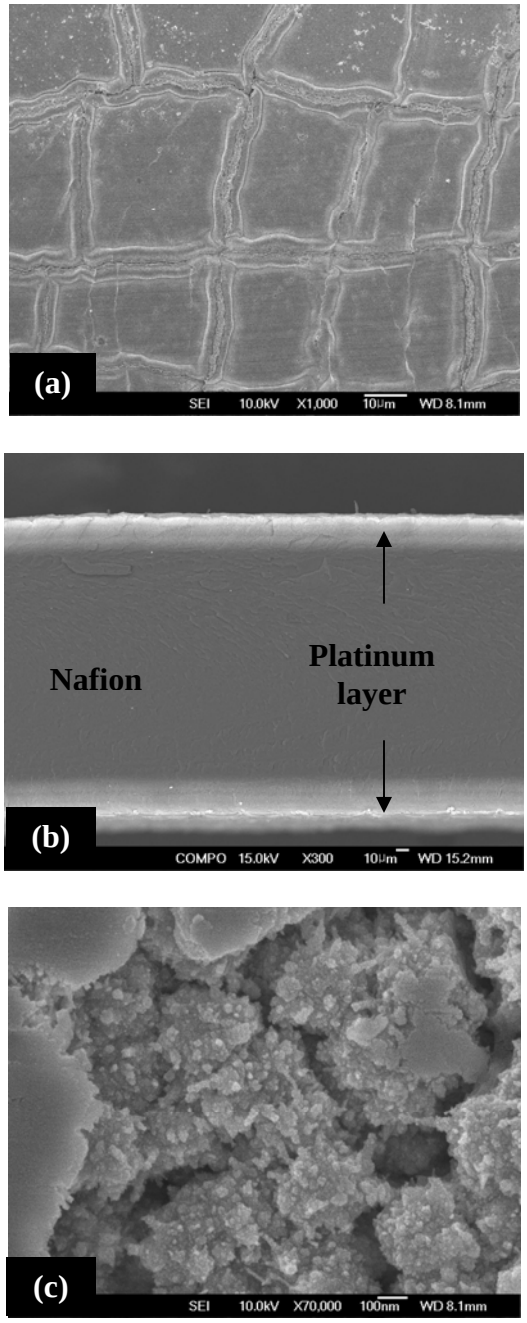

Figure 4.1. Top view (a) and cross-section view (b) of the platinum-IPMC as scanning electron microscopy (SEM) images. A close-up view of the surface of the platinum electrocatalyst layer is shown (c).

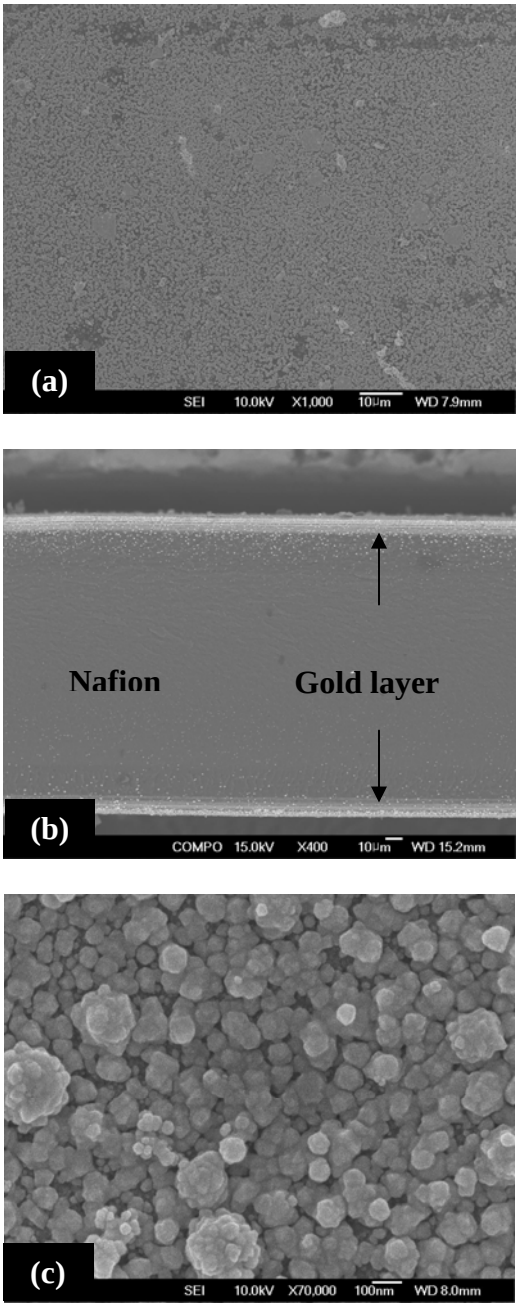

Figure 4.2. Top view (a) and cross-section view (b) of the gold-IPMC as scanning electron microscopy (SEM) images. A close-up view of the surface of the gold electrocatalyst layer is shown (c).

4.2. Mechanical and thermal behavior

During an IPMC operation, the membrane undergoes substantial mechanical stress; therefore, an IPMC requires a more durable membrane. This can be achieved by increasing the physical strength of the membrane. In order to investigate the effect of platinum and gold metals on the Nafion™ membrane for mechanical properties of the IPMC, tensile tests were performed using a universal tester, shown in Figure 3.4. Tension test specimens were prepared from Nafion™ 117 and the fabricated IPMCs under fully dried and fully hydrated conditions (Note that hydrated samples were immerse in DI water for 24 hours and dried samples were dried in an oven at 60^{o}C for 24 hours). Five tests per sample were performed. Figure 4.3 shows the typical stress-strain curves with regard to normal stress versus normal strain on dried Nafion™ 117, hydrated Nafion™ 117, dried platinum-IPMC, hydrated platinum-IPMC, dried gold-IPMC, and hydrated gold-IPMC. Young's modulus is taken as the linear regression of the initial linear part of the stress-strain curve, and tensile strength is obtained at the break point. Young's modulus and tensile strength values of the samples are provided in Figure 4.4, Figure 4.5, and Table 4.1. The curves for the dried samples monotonically shift upward, corresponding to increases in the tensile strength. From Young's modulus results, a similar trend are seen for tensile strength results because the amorphous domain (with higher strength) decreases, leading to a lower Young's modulus. The increase in the tensile strength and the Young's modulus of platinum-IPMC and gold-IPMC is attributed to the platinum and gold metals. The depositions of platinum and gold onto the Nafion™ membrane substantially increase the mechanical strength. However, there was little increase in the mechanical strength of the hydrated IPMC samples. The curves for the

hydrated samples showed decreased break stress values. This means that, in the tensile strain, the stress-strain responses are predominated by, not only the membrane and metallic electrode materials, but also the water molecules. Water molecules in the Nafion™ membranes, the platinum-IPMCs, and gold-IPMCs lead to lower break stress. The membrane changes dimensionally due to water molecules that swell the Nafion™ substantially. In addition, since water has a very low glass transition temperature (Tg) (estimated value at -130˚C) [90], the water acts as a good plasticizer even in small quantities. The interference between water and the chain-to-chain secondary bonding reduces the intermolecular forces. As a result, chains acquire greater mobility and the free volume increases, leading to a decrease in strength [91]. The curves for the metal coated samples showed decreased break strain values. Seemingly, metal particles influence the samples in break strain. In particular, nano-sized gold particles shown in the SEM image of Figure 4.2 contributed to the significant increase in the Young's modulus and the tensile strength of the dried gold-IPMC. It is believed that the dried gold-IPMC exhibit higher break stress and lower break strain than for dried platinum-IPMCs due to nano-sized particles of gold. The complex of gold particles and water in hydrated gold-IPMC contributed to increase in break strain than in dried platinum-IPMC.

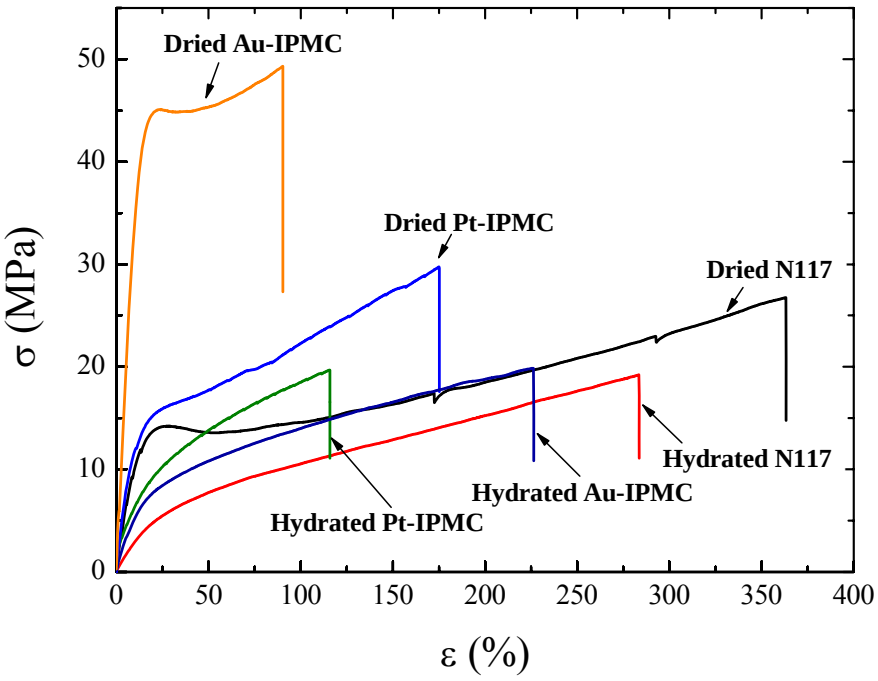

Figure 4.3. Stress-strain curves from tensile testing results.

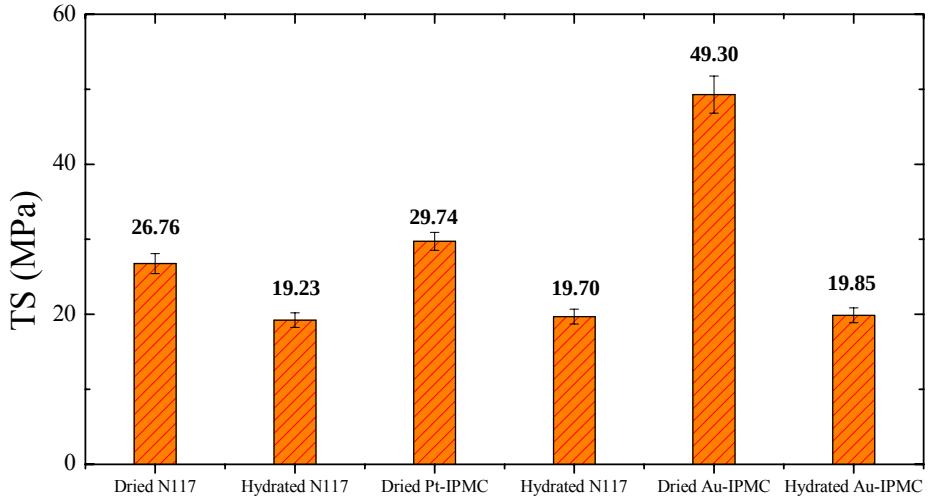

Figure 4.4. Tensile strength (TS) of Nafion™ 117 and IPMC samples.

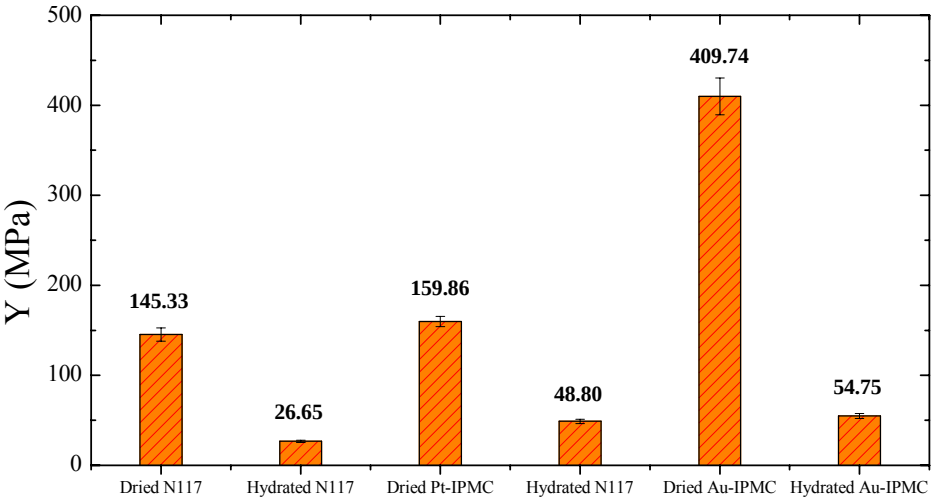

Figure 4.5. Young's modulus (Y) of Nafion™ 117 and IPMC samples.

Table 4.1. Mechanical properties of Nafion™ 117 and IPMC samples.

Sample	Condition	Young's Modulus, MPa	Tensile Strength, MPa
Nafion™ 117	Dried	145.33	26.76
Nafion™ 117	Hydrated	26.65	19.23
Pt-IPMC	Dried	159.86	29.74
Pt-IPMC	Hydrated	48.80	19.70
Au-IPMC	Dried	409.74	49.30
Au-IPMC	Hydrated	54.75	19.85

In order to measure thermal properties, such as glass transition temperature (Tg) and melting temperature (Tm) of samples, DSC measurements were performed on a DSC Q10. Dried samples of Nafion™ 117, platinum-IPMC, and gold-IPMC were tested in aluminum pans, purged with nitrogen gas with a heating rate of 10˚C/min. The sample weight in these DSC experiments was in the range of 5 to 10 mg. In general, amorphous polymers undergo a substantial change in their properties as a function of temperature. The Tg is a boundary between the glassy region of behavior, in which the polymer is relatively stiff, and the rubbery region, in which the polymer is very compliant. Tg can also be defined as the temperature at which solidification without crystallization takes place from viscous liquid or the temperature at which the slope of the volume changes versus temperature as shown in Figure 4.6. Since polymers are non-crystalline or at most semicrystalline, the values obtained in this measurement are dependent on how fast it is taken [92]. Figure 4.7 and Figure 4.8 depict DSC results for the samples. The DSC thermograms presented Tg. There are two Tg peaks for Nafion™, platinum-IPMC, and gold-IPMC. The Tg values for Nafion™ showed approximately 128˚C and 244˚C, respectively. The first Tg was assigned to the Tg of the polymeric matrix, and the second Tg was assigned to the Tg of the ionic clusters. The second Tg was believed that the Nafion™ at the temperature of 244˚C was also associated with the region of crystalline melting of the Nafion™ [93]. The significant increase in the Tg of platinum-IPMC and gold-IPMC is due to the platinum and gold metals. It was determined that an increase in the amount of and dimensions of the clusters and reduction in the mobility of polymeric chains resulted in the observed shift of the glass-transition to a higher temperature [90].

Since the melting temperatures of platinum (1,768.4˚C) and gold (1,064.2˚C) are very high [94], Tm of platinum-IPMC and gold-IPMC were not observed in the range of operation temperatures.

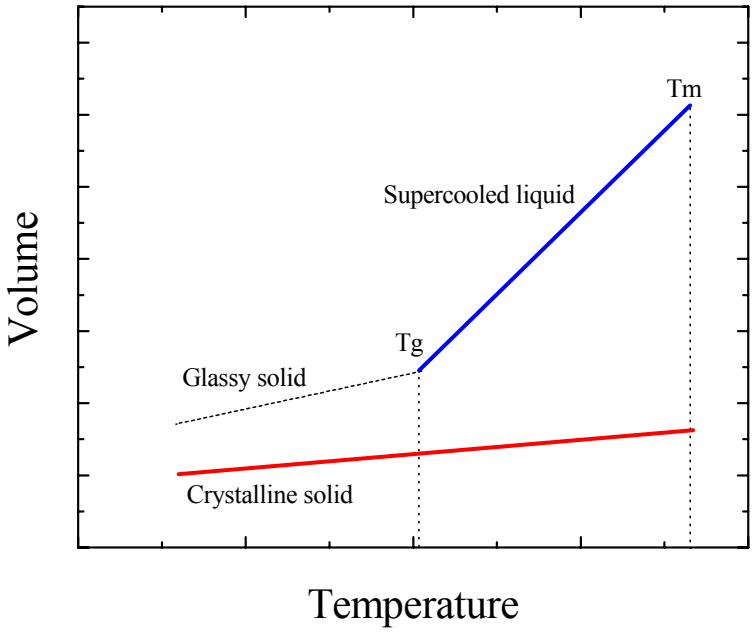

Figure 4.6. Change of volume versus temperature of a solid. The glass transition temperature (Tg) and below Tg the material behaves as a solid like a window glass [92].

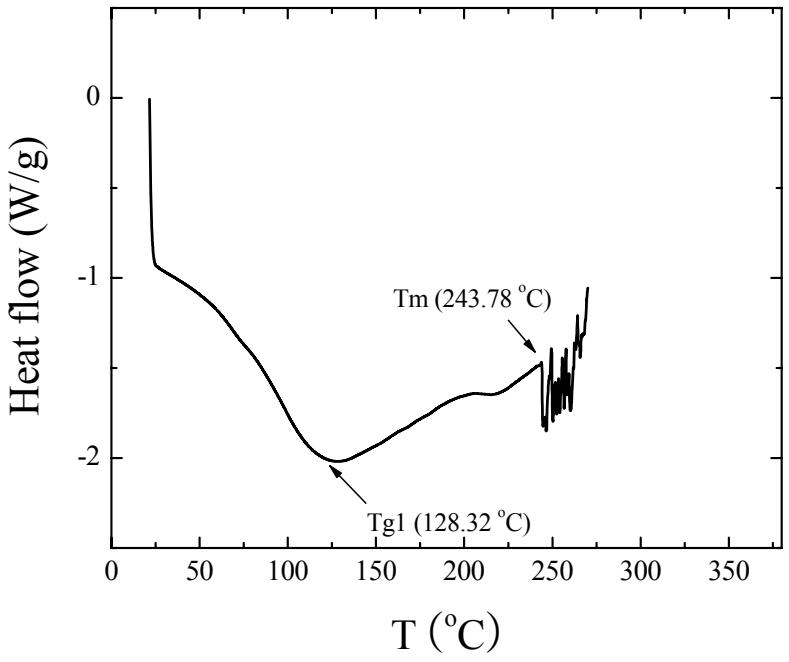

Figure 4.7. DSC thermogram of dried Nafion™ 117 with a heating rate of 10˚C/min under nitrogen atmosphere.

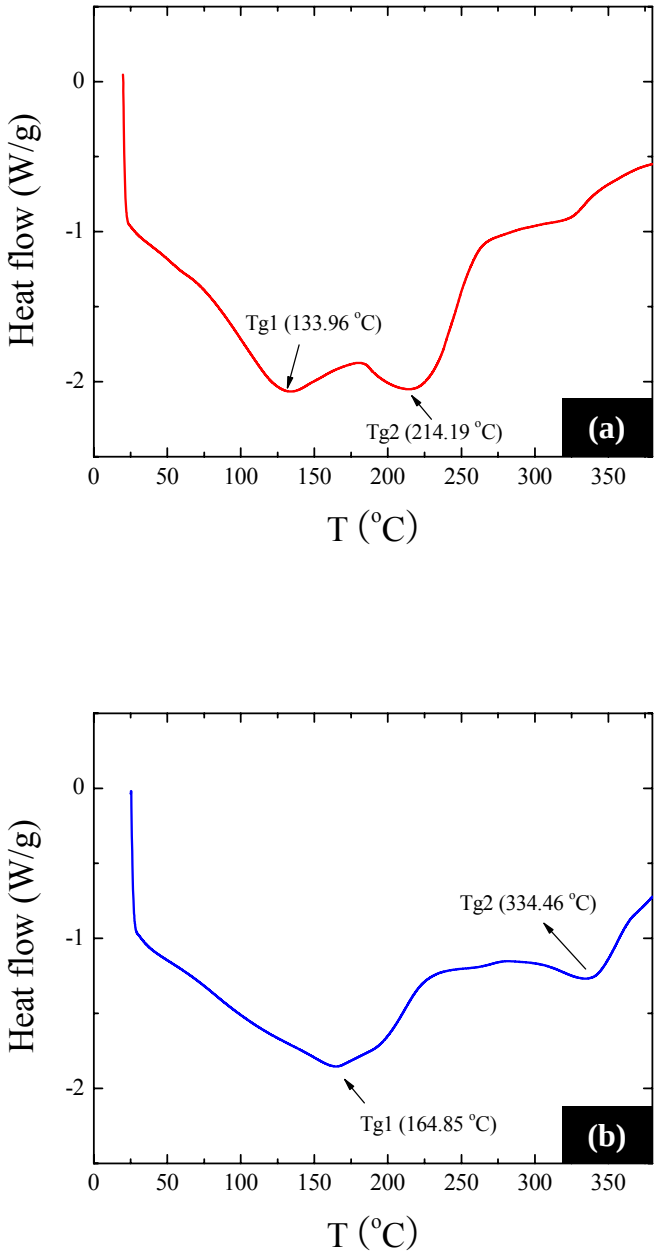

Figure 4.8. DSC thermograms of platinum-IPMC (a) and gold-IPMC (b) with a heating rate of 10˚C/min under nitrogen atmosphere.

The Dynamic Mechanical Analyzer (DMA) is a dynamic mechanical spectrometer that measures two types of parameters, the moduli and the loss tangents. In general, material strength is characterized by the elastic modulus properties and depends on the mechanical properties of the material and its dimensions. The moduli obtained from a DMA testing of materials are similar to Young's modulus but are fundamentally different in that they are treated as a complex quantity. Damping is expressed in terms of tan *delta* and is related to the amount of energy a material can store. A higher tan *delta* peak reflects higher damping; conversely, a lower tan *delta* peak indicates better resiliency or rebound characteristics of the material. Usually, these measurements are conducted in a tension mode using a dynamic frequency temperature sweep, which simultaneously executes a dynamic frequency sweep and a dynamic temperature step. This allows the application of a sinusoidal deformation on the sample over a range of frequencies while temperature is stepped between selected temperature limits [95].

Frequency of the oscillations was fixed at 1 Hz with strain amplitude. The heating rate was 2˚C/min for all temperature scan tests. The results of the ambient scan of the saturated Nafion™ 117, platinum-IPMC, and gold-IPMC are shown in Figure 4.9 ~ Figure 4.11. Figure 4.9 presents the storage modulus (E') curves for the samples. The data give information on the position of the Tg, sample stiffness. The DSC is a general method to obtain the Tg of the samples, but it is less sensitive than the DMA. The DMA Tg was obtained by the maximum peak value of tan *delta.* Figure 4.10 depicts the dynamic loss modulus (E") curves for the samples. The tan *delta* curve was obtained from the relationship between E' and E" (Equation 3.4). The tangent of the phase angle shown in Figure 4.11 is one of the most basic properties measured. This property is also called the

damping, and is an indicator of how efficiently the material loses energy to molecular rearrangements and internal friction [85].

Table 4.2 summarizes the tensile test, the DSC, and the DMA results. Young's moduli of the platinum-IPMC and the gold-IPMC are higher values than for pure Nafion™ 117. A similar trend is seen for the tensile test and the DMA. However, for platinum-IPMC, the tensile test Young's modulus showed much smaller than the DMA Young's modulus. From the Tg results, a similar trend is also seen for the DSC and the DMA. The DMA Tg showed approximately 10˚C lower than the DSC Tg.

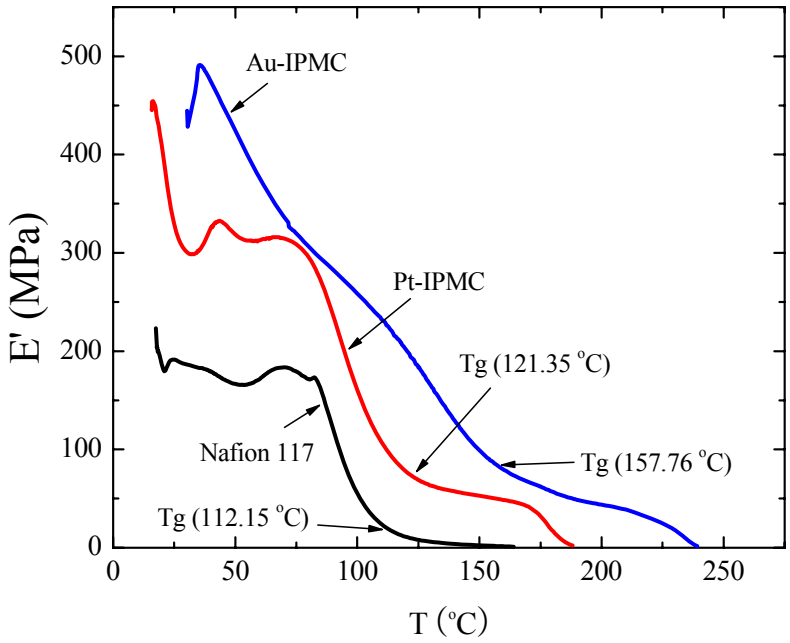

Figure 4.9. Storage moduli (E') of Nafion™ 117, platinum-IPMC, and gold-IPMC with ambient DMA scan (heating rate of 2°C/min).

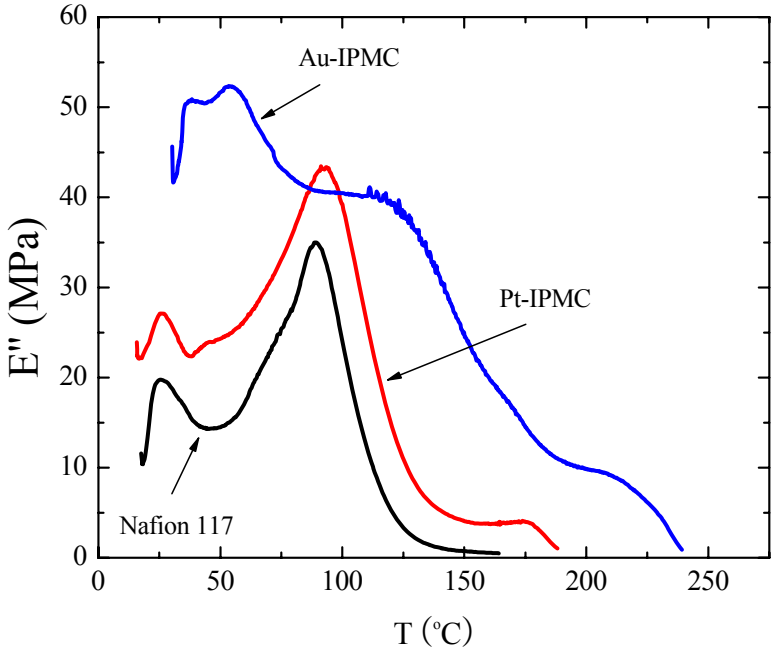

Figure 4.10. Loss moduli (E") of Nafion™ 117, platinum-IPMC, and gold-IPMC with ambient DMA scan (heating rate of 2˚C/min).

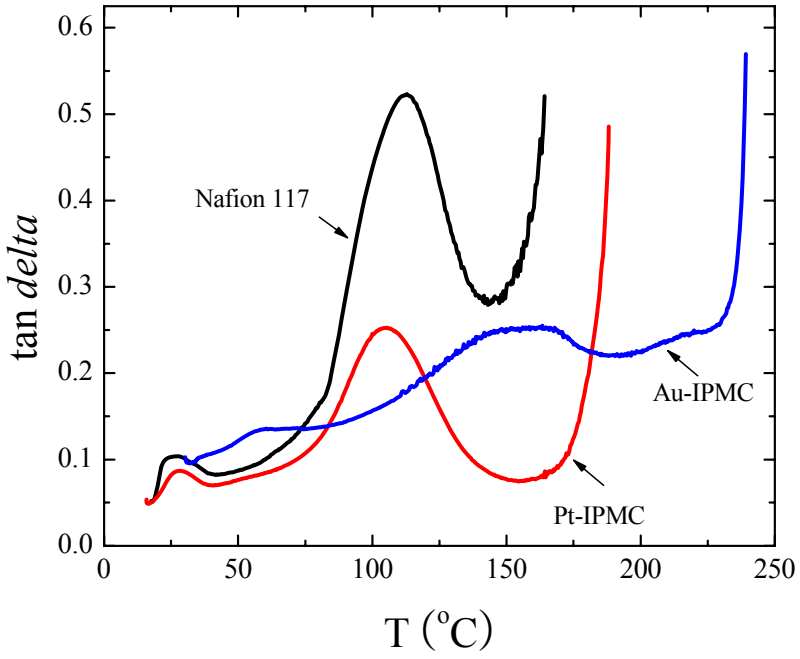

Figure 4.11. tan *delta* of Nafion™ 117, platinum-IPMC, and gold-IPMC with ambient DMA (heating rate of 2˚C/min).

Table 4.2. Young's modulus (Y) and glass transition temperature (Tg) of Nafion™ 117, platinum-IPMC, and gold-IPMC measured from different methods. *Note that all samples were fully dried before experiments.

	Nafion™ 117	Pt-IPMC	Au-IPMC	Method
Y (MPa)	145.33	159.86	409.74	Tensile test
	185.73	299.76	428.30	DMA
Tg (˚C)	128.32	133.96	164.85	DSC
	112.15	121.35	157.76	DMA

4.3. Electrochemical investigation

Although the electrochemical properties on the electrode surface of IPMCs during actuation is one of the important factors for interpreting the fundamental actuation mechanisms of IPMCs, there have been few studies on the electrode/electrolyte interface of IPMCs. In this section, electrochemical analyses, including cyclic voltammetry (CV), chronopotentiometry (CP), chronoamperometry (CA), and electrochemical impedance spectroscopy (EIS), were carried out in aqueous environments.

In general, most studies on solid-state redox systems are at least initially based on CV. In CV, the potential of the working electrode is scanned linearly between two threshold values and the current is measured. When redox reactions occur in the potential region, a wealth of information from the current peaks can be obtained about the reversibility and type of processes, and the nature of reaction products [96]. Figure 4.12 shows typical cyclic voltammograms of platinized platinum and gold in 1 M H_2SO_4 with a scan rate of 20 mV/s. In Figure 4.12 (a), the cyclic voltammogram for a platinum electrode clearly shows defined peaks starting at approximately +0.55 V (*vs*. SCE) on the anodic scan and starting at approximately +0.82 V (*vs*. SCE) on the cathodic scan. These peaks correspond to the oxidation and reduction of oxide layers on the platinum electrode surface. Platinum oxidation occurs in the presence of adsorbed hydroxyl radicals *i.e.*, Pt-OH_{ads}. Platinum oxidizes to platinum oxide by the dehydrogenation of Pt-OH_{ads}. Electrochemical desorption of the platinum oxide layer results in a single peak on the cathodic scan of the voltammogram. In addition, hydrogen absorption/desorption peaks in the range of approximately +0.10 V and -0.25 V (*vs*. SCE) were also observed during this process. The cyclic voltammogram for a gold electrode (Figure 4.12(b)) also shows

defined peaks starting at approximately +1.00 V and +1.18 V (*vs*. SCE) on the anodic scan and starting at approximately +1.1 V (*vs*. SCE) on the cathodic scan. These peaks also correspond to the oxidation and reduction of oxide layers on the gold electrode surface. It is interesting to note that the oxidation and reduction potentials of gold are higher than for platinum. These results indicate that gold can be used in a higher range of potential without electrochemical reactions. In Figure 4.13, starting at the most cathodic potential (-0.25 V *vs*. Ag/AgCl), the positive scan through the hydrogen desorption exhibits an increase in mass change, implying that H_2O adsorption takes place after the hydrogen is desorbed. Also, it can be clearly observed that the increase in mass in the hydrogen region is significant, meaning that the adsorption of H_2O occurs in the double layer region during the scan. Accordingly, platinum oxide formation starts and leads to a decrease in mass [97, 98]. It is believed that water clusters of large mass are desorbed from the platinum due to the adsorption of one oxygen molecule from the water clusters.

Figure 4.14 shows the cyclic voltammogram, the corresponding deflection, the curvature, and the bending strain of platinum-IPMC in 1 M H_2SO_4 solution. The high capacitive current is attributed to the existence of porous platinum, as can be seen in Figure 4.1(c). The reduction of platinum oxide starts at approximately +0.6 V (*vs*. SCE). Hydrogen absorption appears between approximately +0.2 V and –0.25 V (*vs*. SCE). A single but broad peak of hydrogen absorption/desorption arises from the high ohmic drop inside the ionomeric electrolyte, and there are concentrations of hydrogen ions due to the use of Nafion™ as a cation-exchange membrane. The peak of platinum oxide reduction also shifted due to the ohmic drop. The corresponding deflection shows the deformation of the IPMC as it returns to its original shape, when the cyclic electric field is applied.

The bending directions of platinum-IPMC in 1M H_2SO_4 are summarized as a function of surface reaction, in Table 4.3. In the anodic scan of the CV, the deflection abruptly decreases above +0.85 V (*vs*. SCE) due to platinum oxide formation; in the cathodic scan, the deflection abruptly increases below +0.42 V (*vs.* SCE) due to the re-activation of the platinum. In addition, the deflection within the hydrogen region is affected by adsorption/desorption of hydronium ions. The platinum-IPMC shows a bending strain in the range of -0.05 % to +0.07 %. A maximum bending strain can be obtained in the pure platinum condition of the electrode. By varying the scan rate applied in the course of the experiment, the time scale of the processes was able to be explored. In Figure 4.15 and Figure 4.16, the redox peaks of the platinum-IPMC, under lower scan rates, are shown at similar potential ranges to the peaks of the platinized platinum. However, under higher scan rates, CV and deflection shapes are less influenced by surface reactions. It can be determined that higher scan rates allow sufficient reaction time of the electrode surface and adequate migration time of ions within the membrane. The sufficient time allows more ions to be attracted on the surface and lead to a larger deflection of the IPMC.

Figure 4.17 shows the cyclic voltammogram and the corresponding deflection data of gold-IPMC. The results also show the deformation of the IPMC as it returns to its original shape, when the cyclic electric field is applied. In the voltammogram, it can be seen that defined peaks indicate oxidation of gold and reduction of gold-oxide. However, the deflection of the gold-IPMC is less influenced by those reactions. The maximum deflection of the gold-IPMC is smaller than that of the platinum-IPMC.

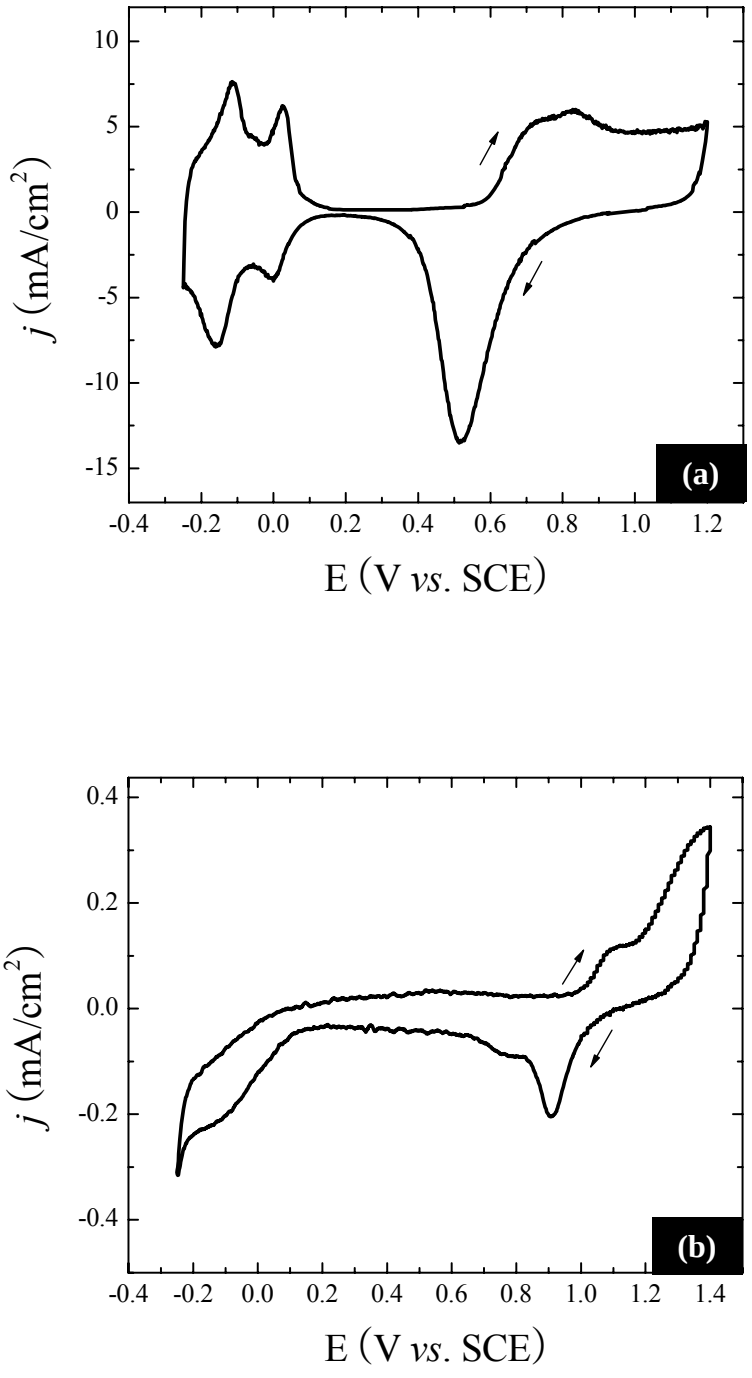

Figure 4.12. Cyclic voltammograms of platinized platinum (a) and gold (b) in 1 M H_2SO_4 solution (scan rate of 20 mV/s).

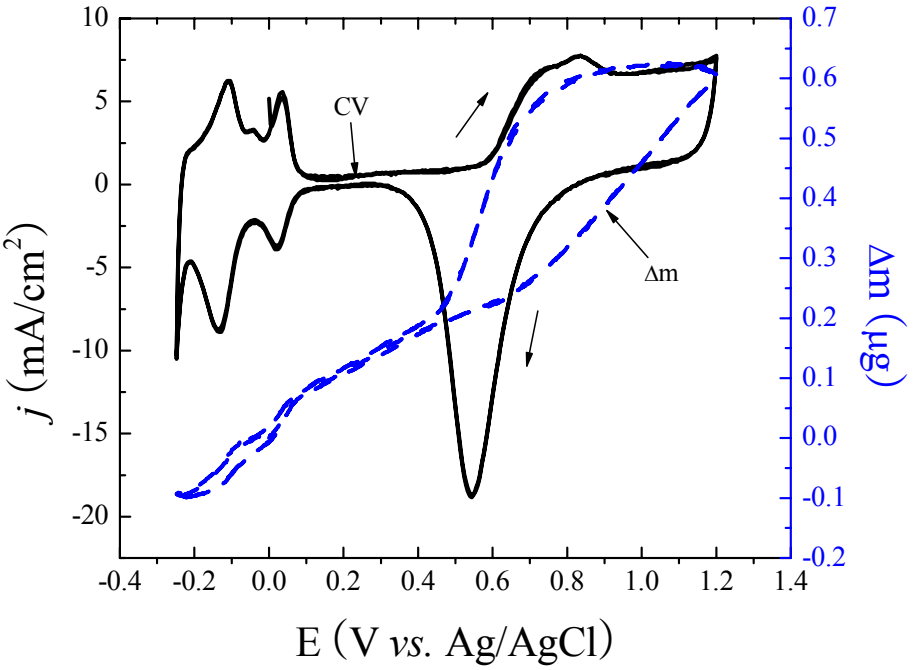

Figure 4.13. Cyclic voltammograms of platinized platinum (solid line); *in-situ* mass change-potential curve (dashed line) in 1 M H_2SO_4 (scan rate of 20mV/s).

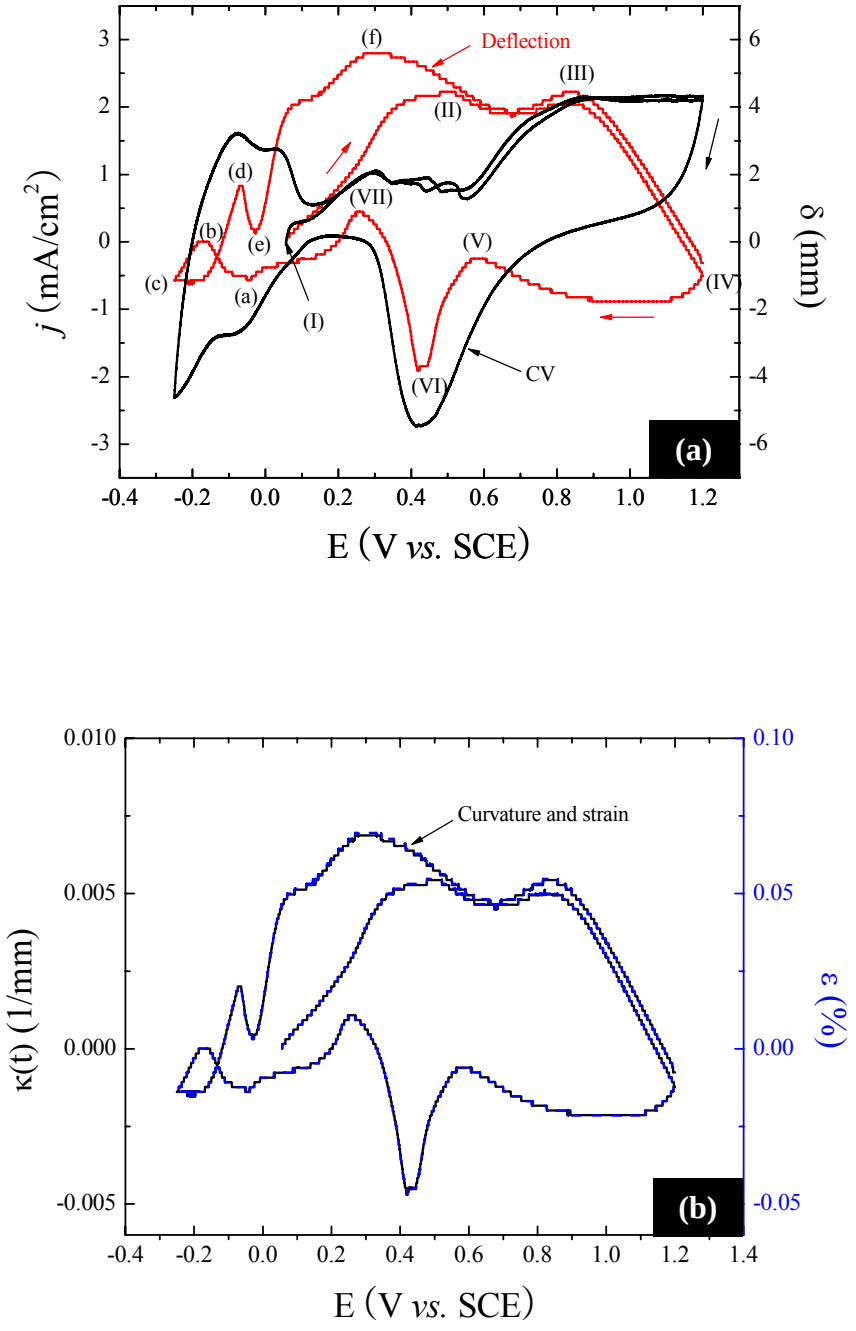

Figure 4.14. Cyclic voltammograms and corresponding deflection data (a) and the curvature and the strain (b) of the platinum-IPMC in 1 M H_2SO_4 solution (scan rate of 5 mV/s).

Table 4.3. Corresponding deflections of platinum-IPMC as a function of surface reactions during the cyclic voltammetry of Figure 4.14.

Potential range	CV direction	Proposed reactions	Bending direction
(I) ~ (II)	(+)	Pt	(+)
(II) ~ (III)	(+)	$Pt + H_2O \rightarrow Pt - OH_{ads} + H^+ + e^-$	(-) → (+)
(III) ~ (IV)	(+)	$Pt - OH_{ads} \rightarrow PtO + H^+ + e^-$	(-)
(IV) ~ (V)	(-)	PtO	(+)
(V) ~ (VI)	(-)	$PtO + H^+ + e^- \rightarrow Pt - OH_{ads}$	(-)
(VI) ~ (VII)	(-)	$Pt - OH_{ads} + H^+ + e^- \rightarrow Pt$	(+)
(VII) ~ (a)	(-)	$Pt + H^+ + e^- \rightarrow Pt - H_{ads}$	(-)
(a) ~ (b)	(-)	$Pt + H^+ + e^- \rightarrow Pt - H_{ads}$	(+)
(b) ~ (c)	(-)	$Pt - H_{ads} + e^- \rightarrow PtH$	(-)
(c) ~ (d)	(+)	$Pt - H_{ads} + e^- \rightarrow PtH$	(+)
(d) ~ (e)	(+)	$PtH \rightarrow Pt - H_{ads} + e^-$	(-)
(e) ~ (f)	(+)	$Pt - H_{ads} \rightarrow Pt + H^+ + e^-$	(+)

* Note that (+) and (-) indicate positive and negative directions, respectively.

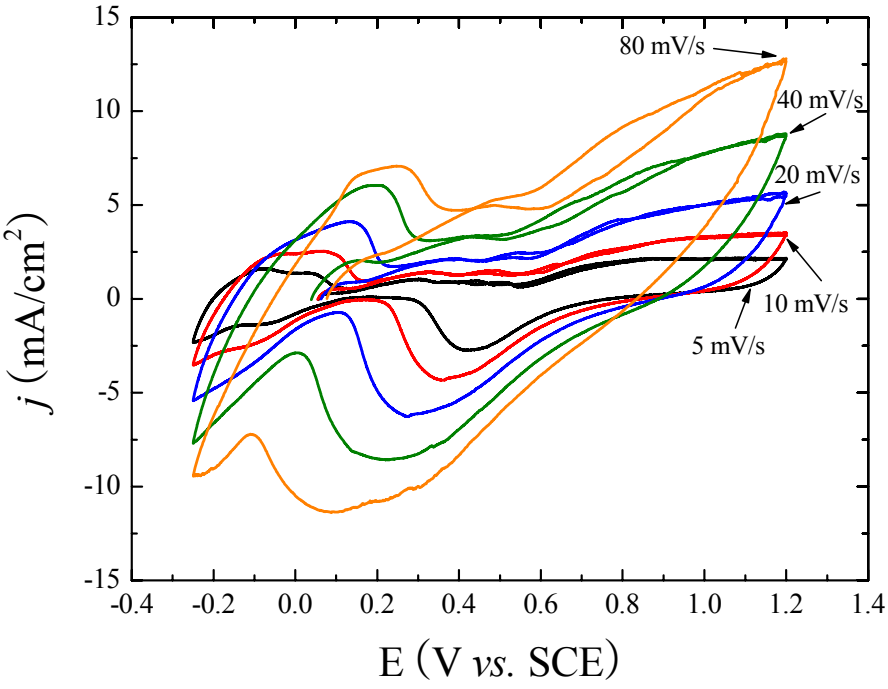

Figure 4.15. Cyclic voltammograms of the platinum-IPMC in 1 M H_2SO_4 solution with different scan rates.

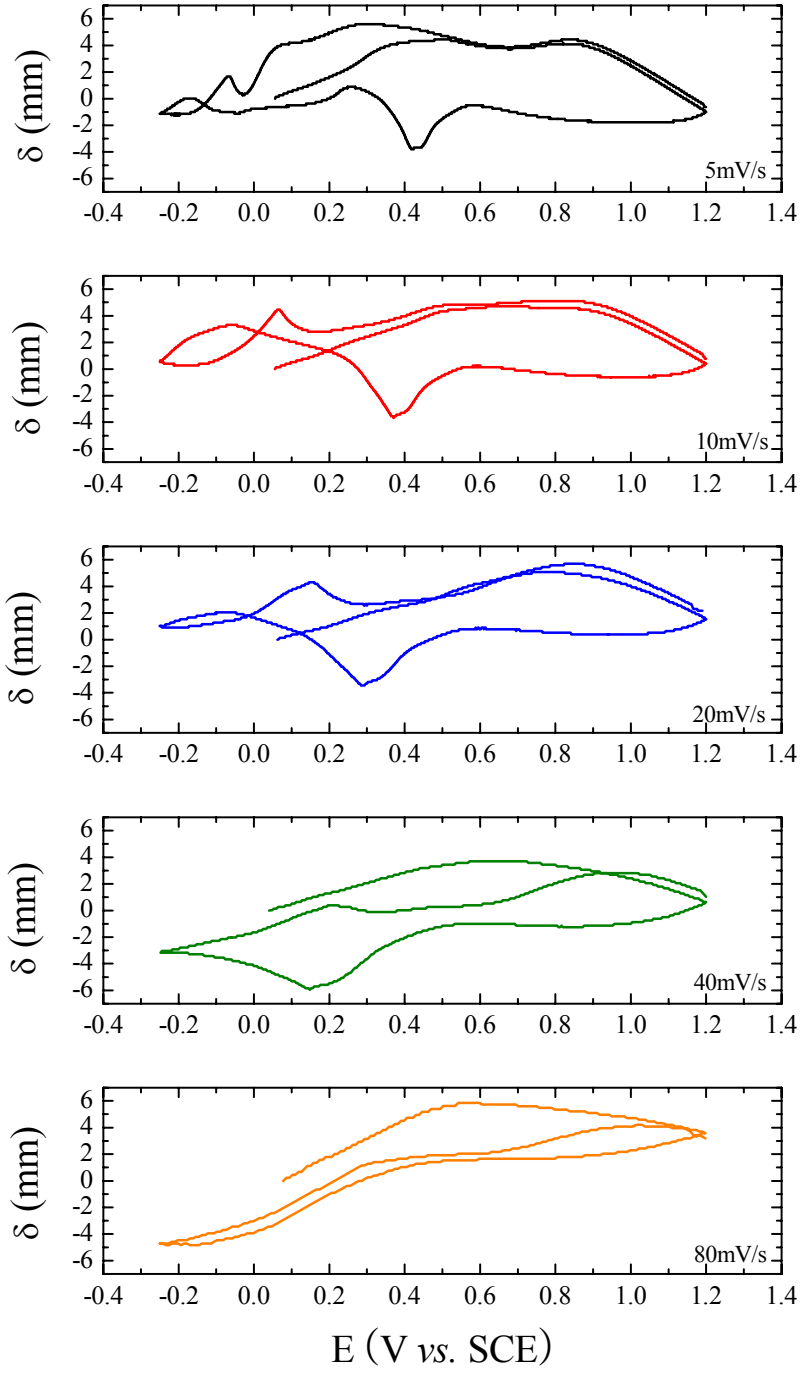

Figure 4.16. Corresponding deflection data during cyclic voltammetries (Figure 4.15) of the platinum-IPMC in 1 M H_2SO_4 solution with different scan rates.

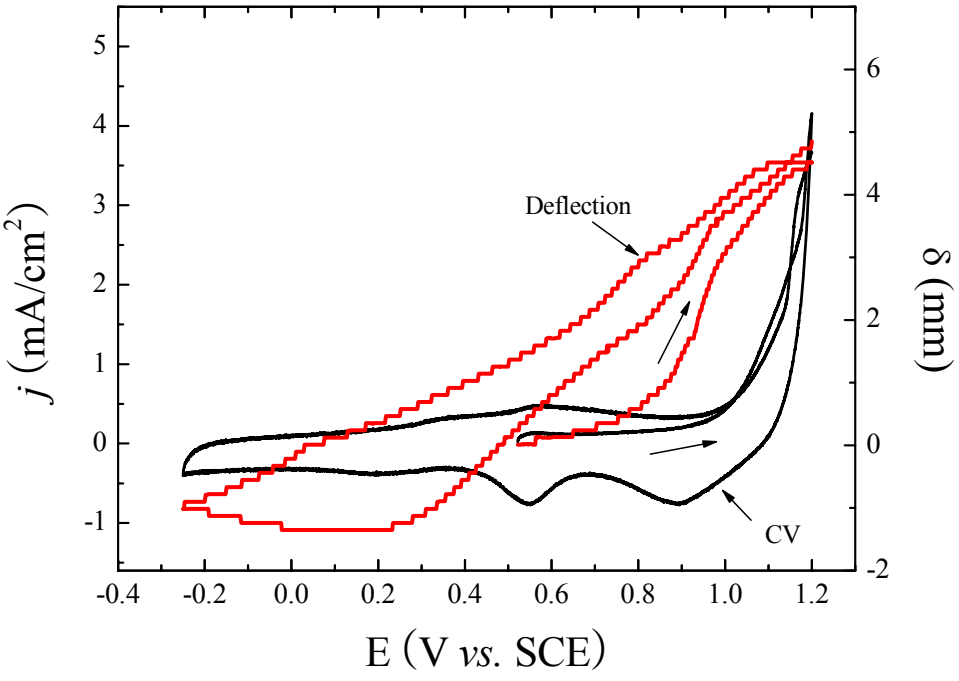

Figure 4.17. Cyclic voltammograms and corresponding deflection data of the gold-IPMC in 1 M H_2SO_4 solution (scan rate of 5 mV/s).

The EIS is a routine method of characterizing of various electrical properties of materials and their interfaces with electronically conducting electrodes. Figure 4.18 shows the impedance behavior at 0.0 V for a platinum-IPMC, as well as the proposed equivalent circuit model [26, 99]. By observing the impedance characteristics of Figure 4.18(a), one is able to view the capacitive/resistive behavior of the IPMC in the double layer potential region, which allows for the material to be modeled using an RC circuit [100]. The basic unit cell model is shown in Figure 4.18(b). The RC circuit connected in parallel represents the surface capacitance and resistance of the particular IPMC. There is an additional resistance for the electrolyte placed in the center of the unit cell, and it represents the resistance that the solvent flux sees during actuation due to migration of hydrated cations and free water through very narrow pores and channels. Figure 4.19(a) compares the AC impedance response (as Nyquist plots) of the platinum-IPMC response, with a variation in the applied potentials in a 0.5 M H_2SO_4 solution. The Nyquist plots of the platinum-IPMC show the similarity of the impedance values of the Nafion™ and the supporting electrolytes, regardless of applied potential. The impedance values of electrodes increased with the applications of voltages between 0.0 V and +1.1 V, and decreased above +1.2 V. This decreasing impedance value is believed to be due to platinum oxide reduction with oxygen evolution. This phenomenon can be seen in Figure 4.19(b) obtained at a frequency of 150 Hz. The capacitance value shown (calculated from a potential scan at fixed frequency; Mott-Schottky experiment; $C=1/(2\pi \cdot f \cdot Z_{im})$) corresponds to the value of the interface capacitance at each potential, when the interface is a pure capacitor. The potential-fixed frequency electrochemical impedance spectroscopy method can provide information about charge transfer and the adsorption

mechanism. Figure 4.20(a), in an interesting note, shows that the circuit model does need some parameters. The effect of inductance is often seen at higher frequencies [101-103]. The impedance of the inductor increases with frequency, while that of the capacitor decreases. At higher frequencies, positive values of the imaginary part show the existence of an inductor, proving that the equivalent circuit of IPMC in the double layer potential region follows an RLC circuit. Figure 4.20(b) is a proposed RLC circuit model of the electrochemical system of the IPMC under applied electric fields.

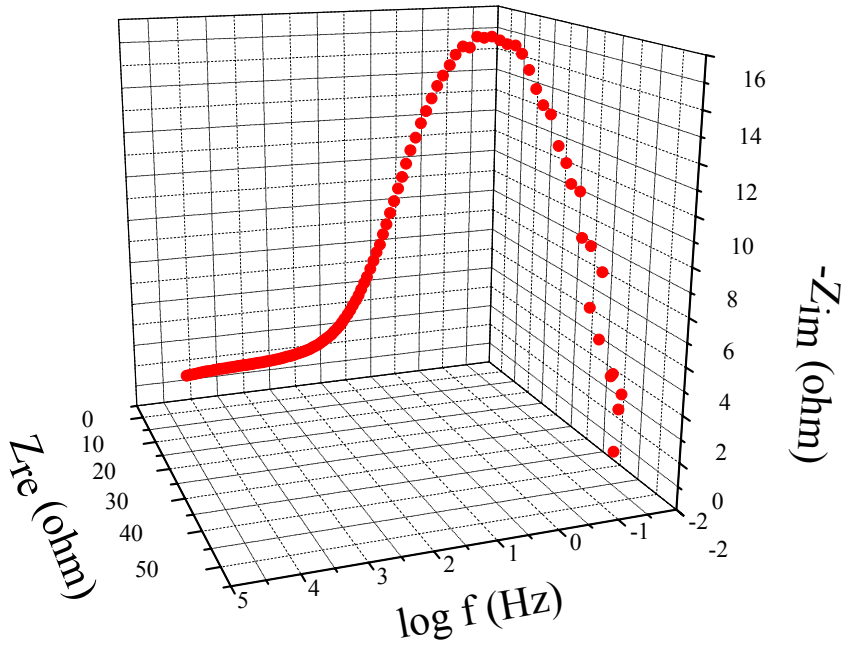

(a)

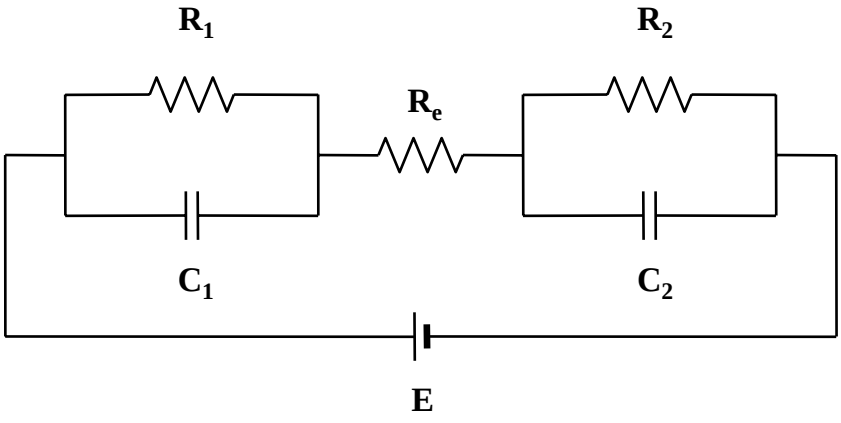

(b)

Figure 4.18. Three-dimensional plots of impedance response for IPMC in the double layer potential region (a) and proposed RC equivalent circuit model (b).

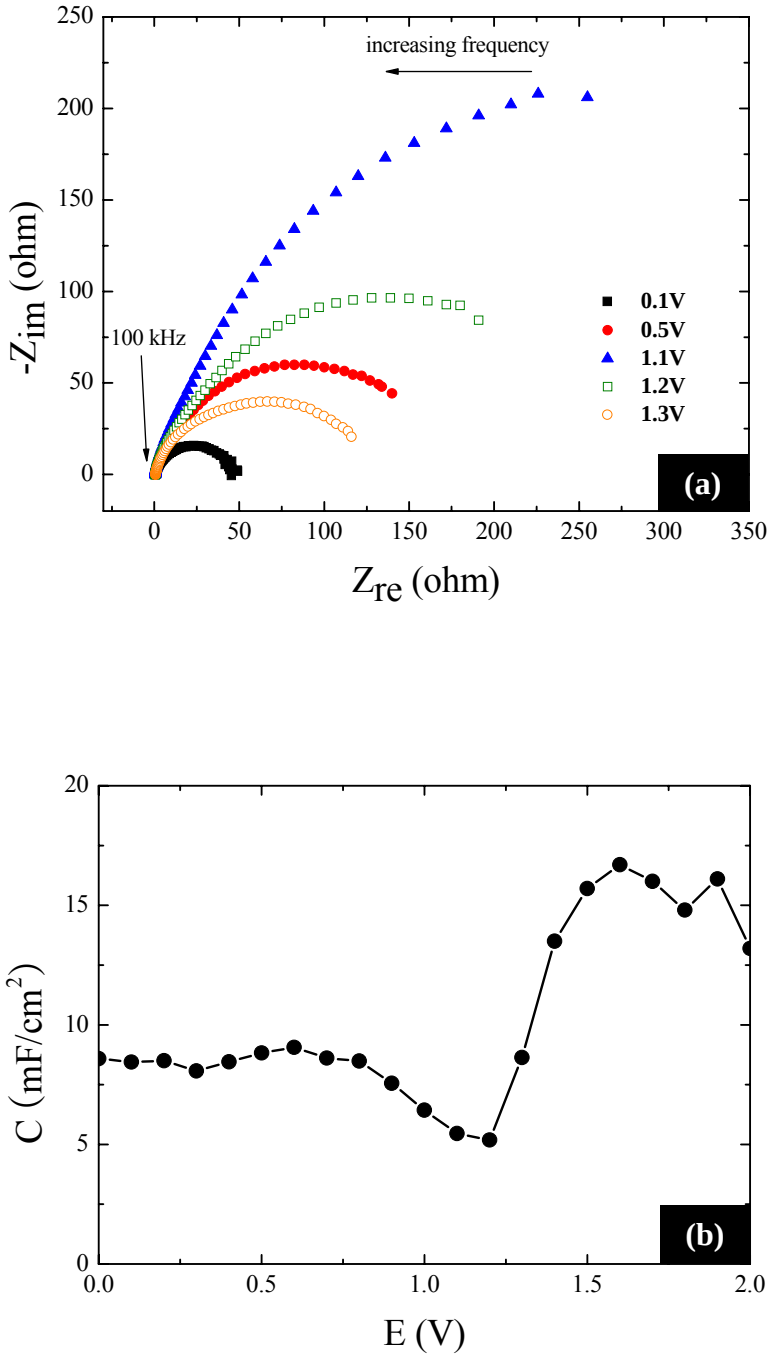

Figure 4.19. Nyquist plots in the frequency range of 100 mHz to 100 kHz (a) and Mott-Schottky experiment at the fixed-frequency of 150 Hz. (b) of the platinum-IPMC in 1 M H_2SO_4 solution.

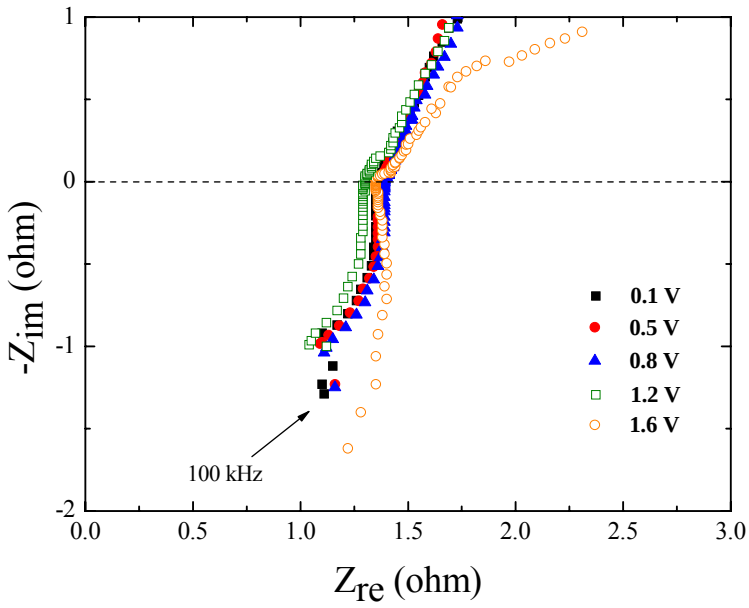

(a)

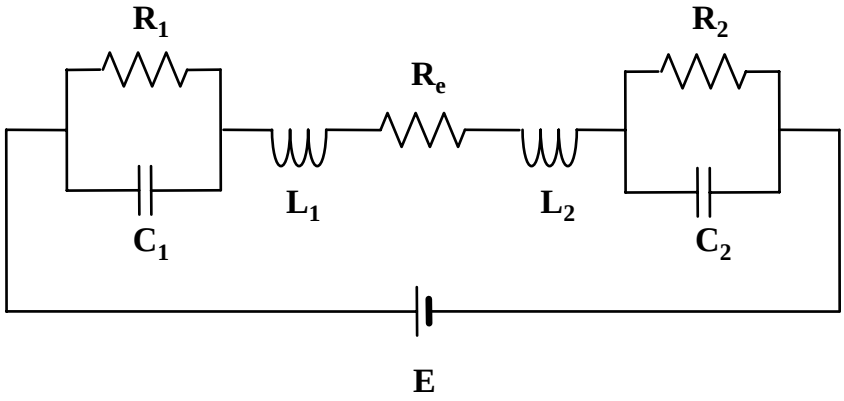

(b)

Figure 4.20. Nyquist plots of platinum-IPMC (a) and proposed RLC equivalent circuit model in the double layer potential region (b).

In order to measure the cell voltage of water electrolysis during the actuation of the IPMC, two-electrode tests, such as potentiostatic linear sweep voltammetry and galvanostatic linear sweep voltammetry, were carried out in an aqueous environment. Due to the required hydration within the membrane, electrolysis is observed at approximately +1.8 V to cause loss of a hydration and, hence, a loss of actuation capabilities. Generally, cell voltage is directly proportional to the power consumption for the process. The cell voltage is composed of:

$$E = E_{rev} + \eta_a + \eta_c + \eta_{IR} \tag{4.2}$$

where E_{rev} refers to the reversible thermodynamic decomposition potential η_a to the anode overpotential, η_c to the cathode overpotential, and η_{IR} to the interelectrode ohmic drop.

Figure 4.21 shows an increase in overpotential of +0.57 V, including activation overpotential, concentration overpotential, and an interelectrode ohmic drop for an IPMC made with electroless deposition of platinum. Note that this overpotential is mainly caused by the resistance of the platinum layers and the solid electrolyte. This result suggests that in the two-electrode system the IPMC can be operated without gas evolution within the ranges of -1.8 V to +1.8 V.

The two electrochemical half-reactions for the electrolysis of water are shown in Table 4.4 and Table 4.5. The primary products of the electrolysis of water are oxygen gas at the anode and hydrogen gas at the cathode. The net reaction entails a 3:2 stoichiometric

ratio of gas to liquid and occurs via the transfer of four equivalents of electrons through an external circuit. From the overall electrochemical reaction, assuming the current efficiency to be 100 %, 2 faradays of electricity are required to produce 1 mole of hydrogen gas.

Table 4.4. Electrochemical reactions at the cathode side under different pH [94].

	Electrochemical reaction	E^0 (V) / pH
Acid media	$4H^+(aq) + 4e^- \underset{oxidation}{\overset{reduction}{\rightleftharpoons}} 2H_2(g)$	0.0 / 0.0
Neutral media	$2H_2O(l) + 2e^- \underset{oxidation}{\overset{reduction}{\rightleftharpoons}} H_2(g) + 2OH^-(aq)$	+0.41 / 7.0
Basic media		+0.82 / 14.0

Table 4.5. Electrochemical reactions at the anode side under different pH [94].

	Electrochemical reaction	E^0 (V) / pH
Acid media	$2H_2O(l) \underset{reduction}{\overset{oxidation}{\rightleftharpoons}} O_2(g) + 4H^+(aq) + 4e^-$	+1.23 / 0.0
Neutral media		+0.82 / 7.0
Basic media		+0.41 / 14.0

Overall electrochemical reactions are;

$$2H_2O(l) \underset{recombination}{\overset{electrolysis}{\rightleftharpoons}} O_2(g) + 2H_2(g) \qquad E_0 = +1.23\ V \quad (4.3)$$

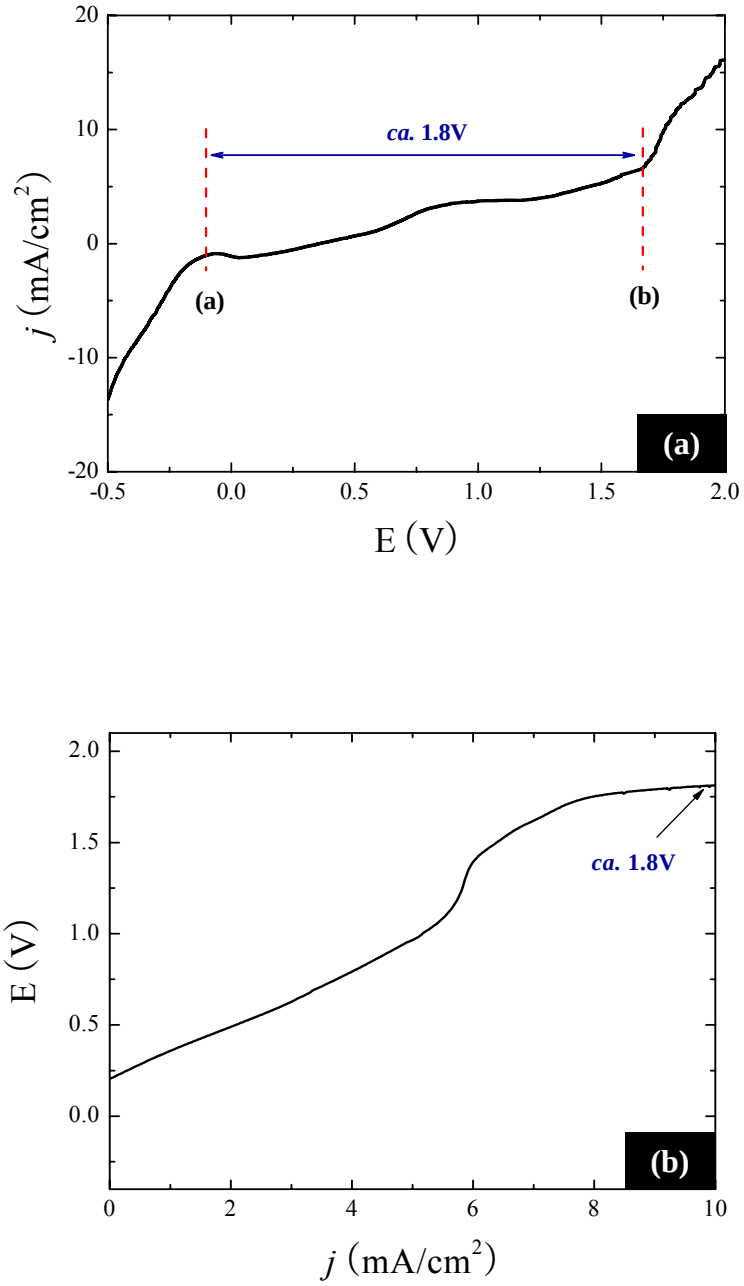

Figure 4.21. Measurement of overpotential of water electrolysis during the actuation of the IPMC: Potentiostatic linear sweep voltammetry (a) and galvanostatic linear sweep voltammetry (b).

Measurements of the mechanical response of an IPMC as a bending actuator are important for understanding its physical behavior under applied electric fields. For bending actuators, the most common metric is the radius of the curvature that can be obtained by deflection measurement. The parameters are most often measured as a function of time to a specified input waveform [86]. The IPMCs as actuators were tested in a cantilevered configuration as shown in Figure 3.7. Deflection of an IPMC was measured using an image-processing technique. To obtain the curvature and strain values of IPMC during actuation, the deflection data were converted into these values. The blocking force of the IPMC was measured using a 10 g-load cell with zero tip displacement.

Figure 4.22 depicts measured two-electrode cyclic voltammograms of a platinum-IPMC with a scan rate of 20 mV/s. As can be seen, a peakless behavior with a small hysteresis is obtained. It does not show any distinct oxidation and reduction peaks within ± 1 V. The overall behavior of the IPMC shows a simple trend of ionic motions caused under an imposed electric field. Corresponding deflection data of the six markers on the edge of platinum-IPMC are shown in Figure 4.22(b). Additionally, the corresponding trajectory data shown in Figure 4.23 provide, clearly, an IPMC bending motion during CV. The deflections of each marker do not show a symmetric motion of the IPMC because the amount of deposits is not exactly the same on both sides. Figure 4.24 shows cyclic voltammograms and corresponding deflection data for different potential ranges. Cyclic voltammograms of ± 1.5 V and ± 2.0 V show distinct oxidation and reduction peaks over ± 1 V. These peaks are induced from platinum oxidation and platinum oxide

reduction, as explained in section 4.3. Deflections of the IPMC relax toward the cathode side above ± 1 V.

The performance of IPMCs was examined by measuring the blocking force in a cantilever configuration, as shown in Figure 3.13, using a 10 g-load cell. The actuation performance of the platinum-IPMCs is given in Figure 4.25, with measured blocking forces being a function of the length of the samples during a linear sweep voltammetry (LSV) with a scan rate of 20 mV/s. The electro-responsive blocking force curves in Figure 4.25 suggest that the length of the IPMC significantly affects the mechanical properties and electromechanical responses. The 10 mm-length IPMC exhibited larger blocking forces than for the others. It is interesting to note that IPMCs generated monotonically increasing blocking forces until approximately +1.1 V and then showed decreasing blocking forces. It can be deduced from this finding that the platinum-IPMCs reach maximum blocking force at approximately +1.1 V, which is clear evidence of platinum oxide formation as mentioned in section 4.3. The maximum value of the blocking force for the 10 mm-length sample was approximately 1.16 mN. The results are believed to be due to the relaxation phenomena of IPMCs. Figure 4.26 presents comparison of corresponding blocking forces of the platinum-IPMC and the gold-IPMC during an LSV with a scan rate of 20 mV/s. The gold-IPMC showed lower values for the blocking force, but there was no relaxation phenomenon in the potential range. The relaxation phenomena will be discussed in Chapter 5, in detail.

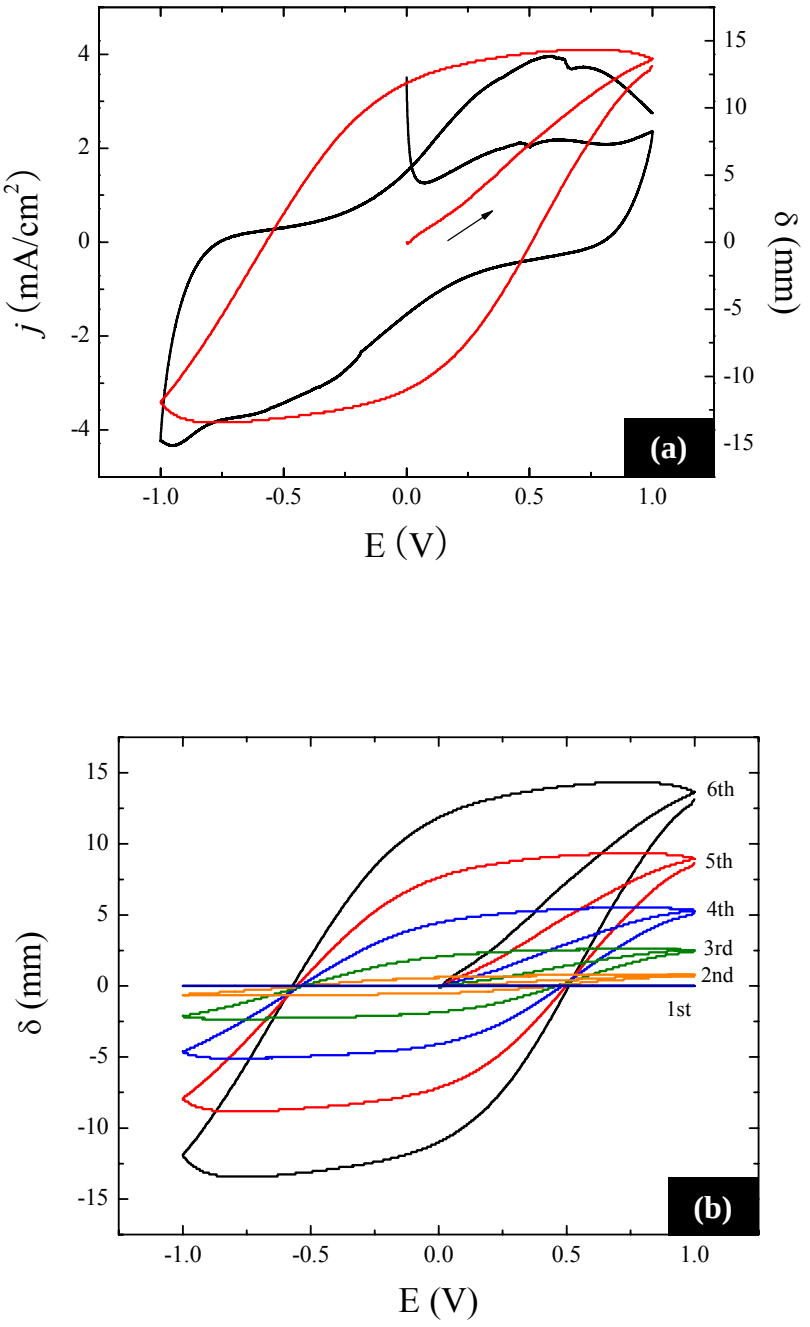

Figure 4.22. Cyclic voltammogram and corresponding tip deflection data (a) and corresponding deflection data (b) of the six markers on the edge of the platinum-IPMC in cantilever configuration during a cyclic voltammetry (scan rate of 20 mV/s).

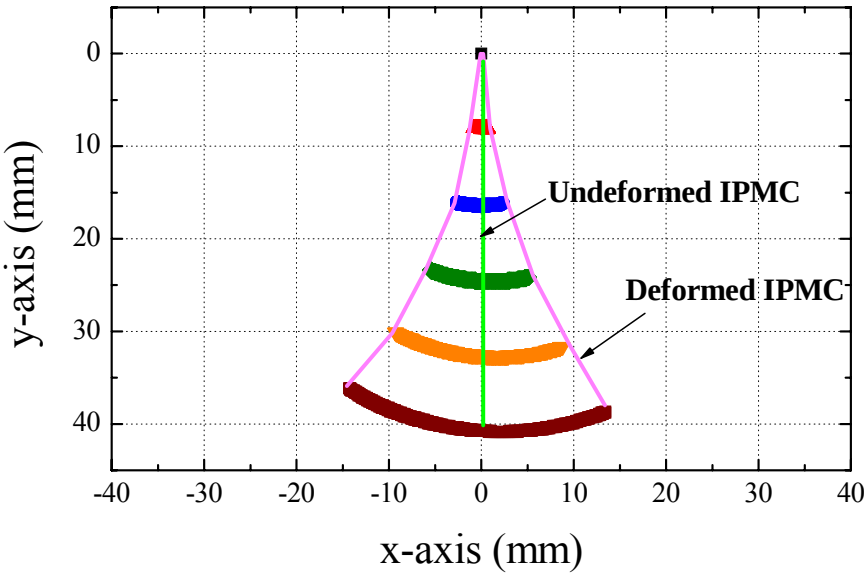

Figure 4.23. Trajectory of the platinum-IPMC in a cantilever configuration during a cyclic voltammetry of Figure 4.22 (a).

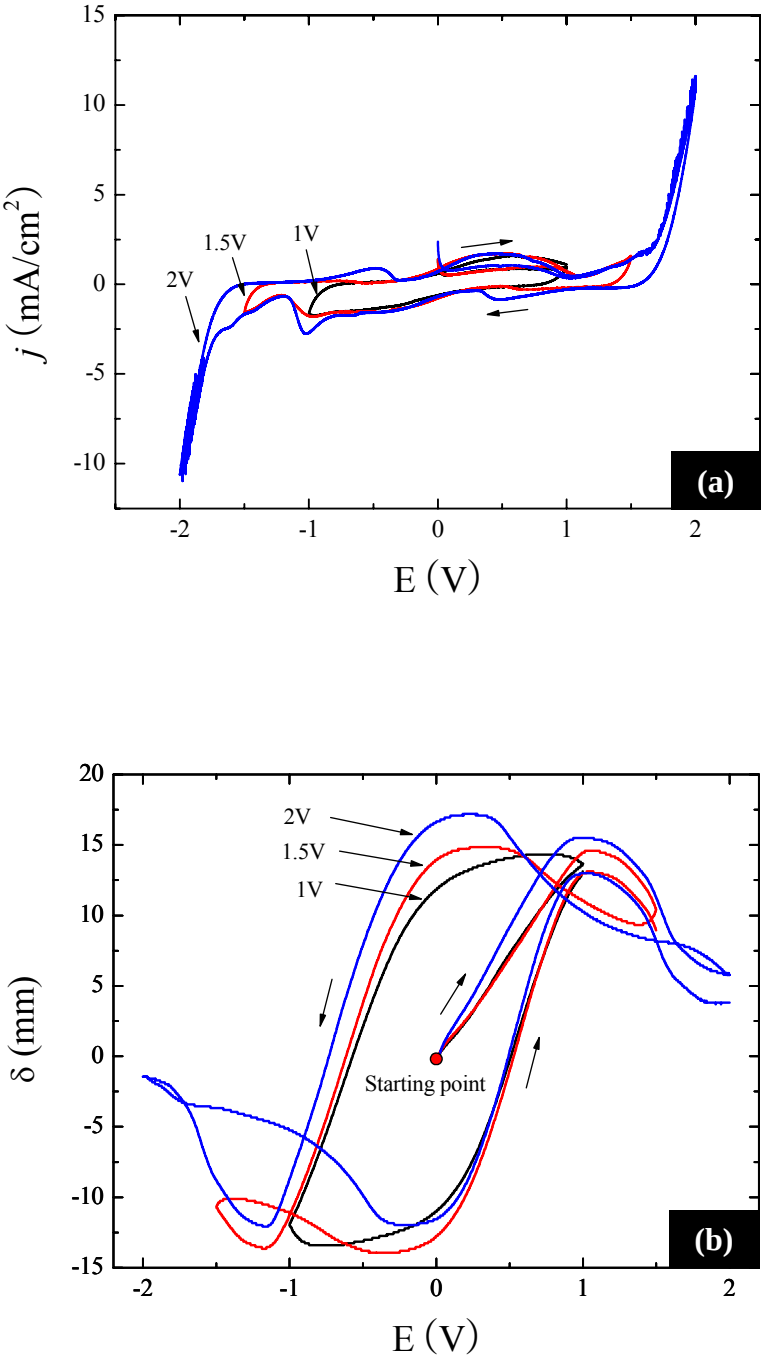

Figure 4.24. Cyclic voltammograms (a) and corresponding deflection data (b) during cyclic voltammetries with different potential ranges

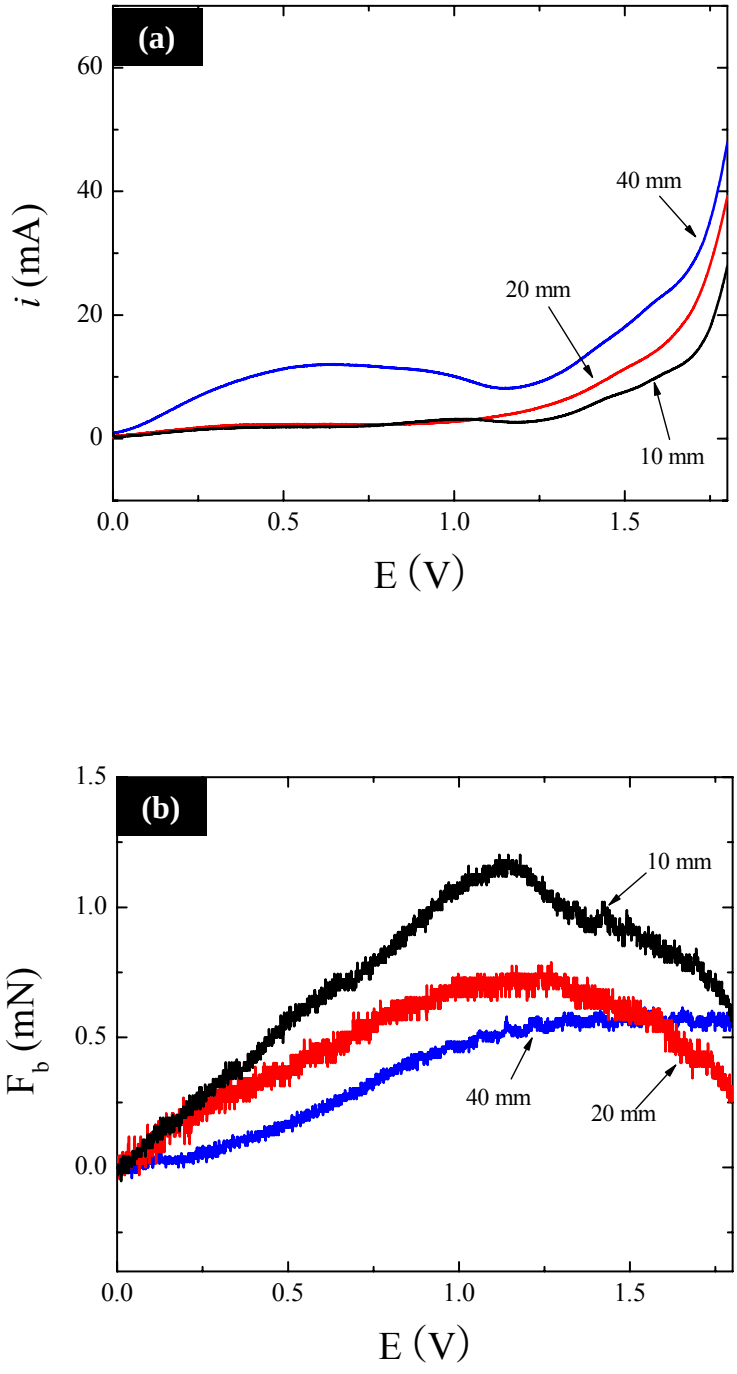

Figure 4.25. Linear sweep voltammograms (a) and corresponding blocking forces (b) of the platinum-IPMCs with three different lengths.

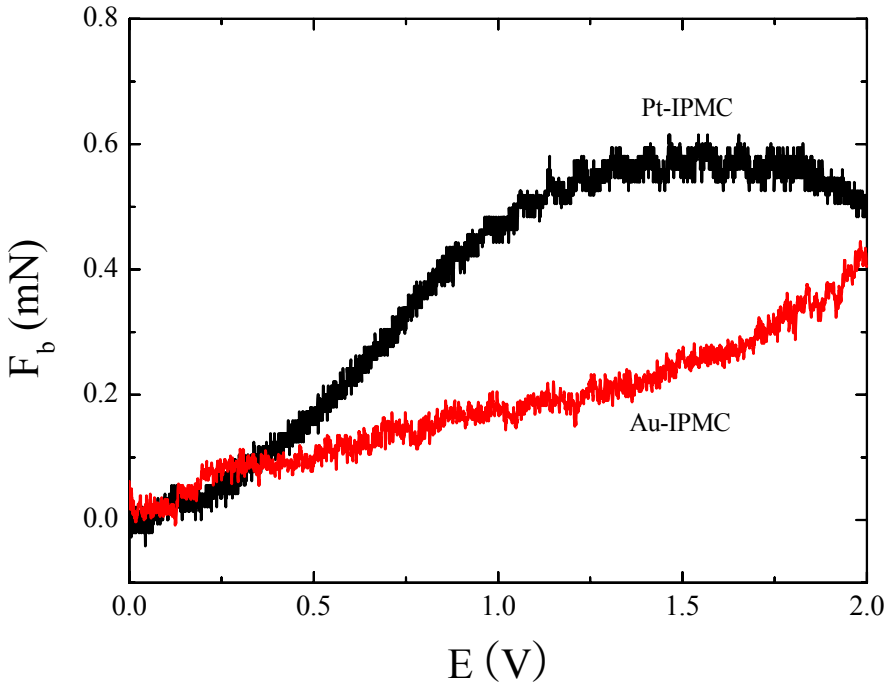

Figure 4.26. Corresponding blocking forces of platinum-IPMC and gold-IPMC during a linear sweep voltammetry (scan rate of 20 mV/s).

CHAPTER 5:

UNDERWATER AND IN-AIR OPERATIONS OF IPMC

IPMCs, due to their high sensitivity to hydration, are ideally suited for operation within an aqueous environment. However, at low frequency, an IPMC is accompanied by a relaxation from the results of which were discussed in Chapter 4. One possible way to handle the relaxation of IPMC is to use feedback controls that require additional equipment. IPMCs show performance degradation within an air environment, due to evaporation of the solvents. Many researchers [16, 104] have tried to solve this problem by using a protective coating and by creating a polymer composite. However, the techniques are still not practical. In order to reduce unwanted reactions and to use IPMCs in an air environment, effective solvents are required. Recently, Bennett and Leo [20] demonstrated an IPMC solvated with room temperature ionic liquids (RTIL). The results indicate that RTILs may be suitable replacements for water as a membrane solvent.

This chapter focuses on the fundamental operation of IPMCs in water and air, on the relaxation problem associated with IPMCs, and on further investigation of the IPMC solvated with an RTIL.

5.1. IPMC operation in water

The large bending motion of the IPMC actuator under low applied voltages and the possibility of operation in an aqueous environment make it useful for various naval

and marine applications [105, 106]. As a flexible hydrodynamic actuator, the IPMC can provide many new opportunities in Navy platforms, especially in developing unmanned vehicles for both surveillance and combat. IPMC materials are virtually silent when in operation since they have no vibration-causing components, *i.e*. gears, motors, shafts, etc. For small autonomous underwater vehicles, these features are attractive due to limited space and their need for silence as well as being effective actuators.

5.2. Relaxation phenomena

The IPMC can operate under a DC or an AC input. Under an AC electric field, an IPMC is found to operate efficiently, alternately bending and straightening, depending largely on the applied DC voltage or on the frequency of the applied AC voltage. When a DC voltage is applied, the IPMC will initially bend toward the anode side, but after some time, the material relaxes toward the cathode side [7, 107-110]. In other words, the application of DC does not allow the IPMC to sustain an induced bending for long period, the IPMC relaxing after several seconds. This relaxation phenomenon often causes poor repeatability and uncontrollability of the IPMC bending [109] and is believed to be caused by a back diffusion of free water that was carried with the cations to the cathode side of the actuator. Data representing this relaxation phenomenon for an IPMC are shown in Figure 5.1. This graph shows the time dependence of IPMC with constant applied voltage, +1, +1.5, and +2 V. The IPMC under +1 V showed large bending and maintained a fairly constant deflection after 10 s. Under +1.5 V of applied voltage, the IPMC shows a larger bending at the initial stage, but the large bending deflection relaxes toward the other side. However, under +2 V of applied voltage, the IPMC shows a

smaller bending motion at the initial stage and slowly increases its bending deflection with time. Maximum deformation is observed at 4 s under +1.5 V and then the IPMC relaxed toward the other side. After relaxation (*ca.* 35 s), the IPMC sustains its deformation. The experimental bending curve data from Figure 5.1 are shown on an x-y axis in Figure 5.2. The bending curve (a) is undeformed IPMC; the bending curves (b) ~ (e) are deformed IPMC at 2 s, 4 s, 10 s, and 40 s, respectively. Figure 5.3 ~ Figure 5.6 clearly show that the relaxation phenomena are caused by the overpotential of the electrode surface. The overpotential values of approximately +1 V were measured for platinum IPMCs. The IPMC does not show any relaxation during bending below +1 V. With applied potentials over +1 V, the IPMCs start to show relaxation phenomena. These findings can be explained by the catalytic activities of the platinum surface. According to the three-electrode CV result of Figure 4.14, the potential for platinum oxide formation was approximately +0.85V. However, CP results of Figure 5.4 ~ Figure 5.6, the relaxation of the IPMC started from approximately +1 V. The results experimentally prove that the relaxation of IPMC bending originates from the oxide formation of platinum during actuation.

In order to compare IPMC operations in water and air, an IPMC was tested in both environments. Figure 5.7 presents two experimentally measured deflections for two IPMCs under applied potential of +1.5 V in air and in water, respectively. For in-air operation, the deflection of the IPMC is larger than in water operation. In this particular experiment, the tip deflection of the IPMC is reduced nearly 40 % when operated underwater compared to in-air operation. It is observed that the IPMC deflections continuously increases during the 40 s for in-air operation, but this is not the case for

water operation, where the IPMC's deflection increases in the first 10 s of the experiment but then relaxes toward the other side and remains constant for the following 30 s of the experiment. This finding can be explained that the deformation of an IPMC is decisively influenced by the friction between the IPMC and water.

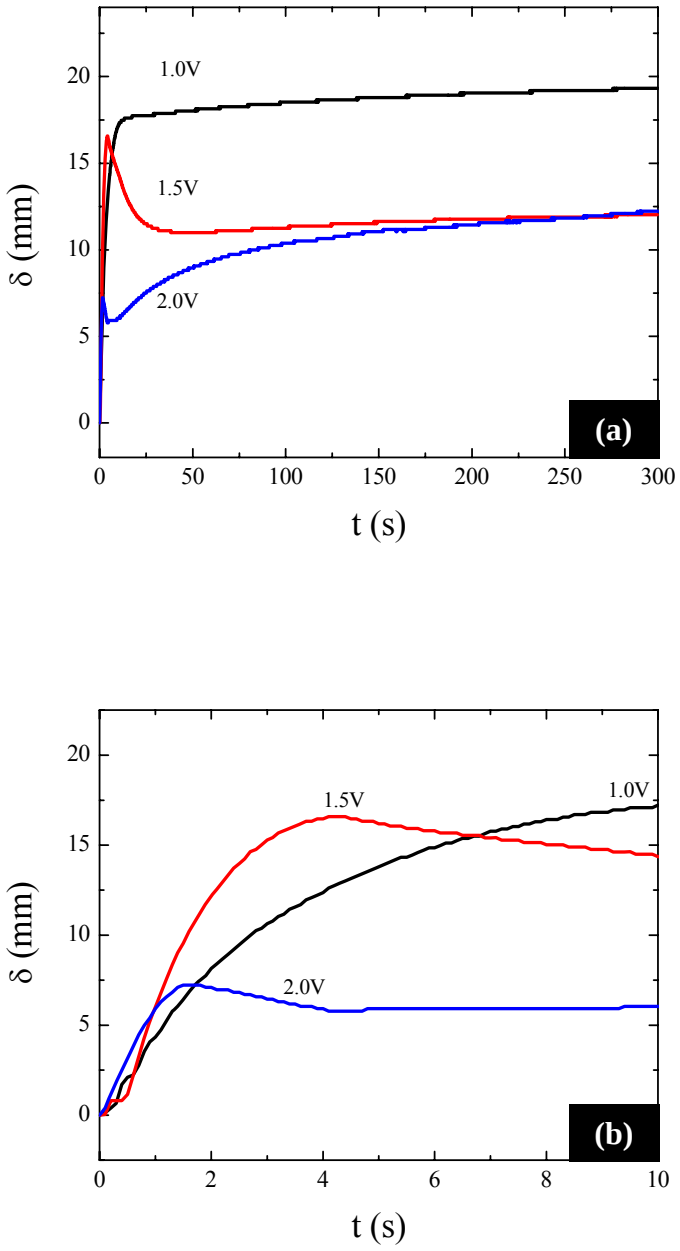

Figure 5.1. Time dependence of bending deflection (a) of the platinum-IPMC upon constant applied voltage, +1.0, +1.5, and +2.0V; A close-up view of (a) at the initial stage (10 s).

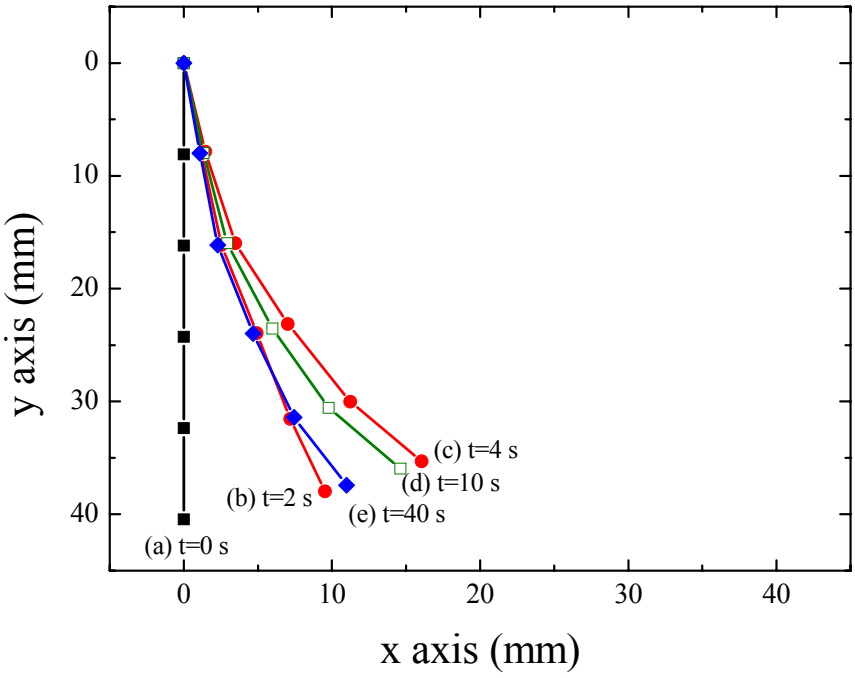

Figure 5.2. Experimental bending curves for the IPMC under applied potential of +1.5 V in water (Figure 5.1) with time.

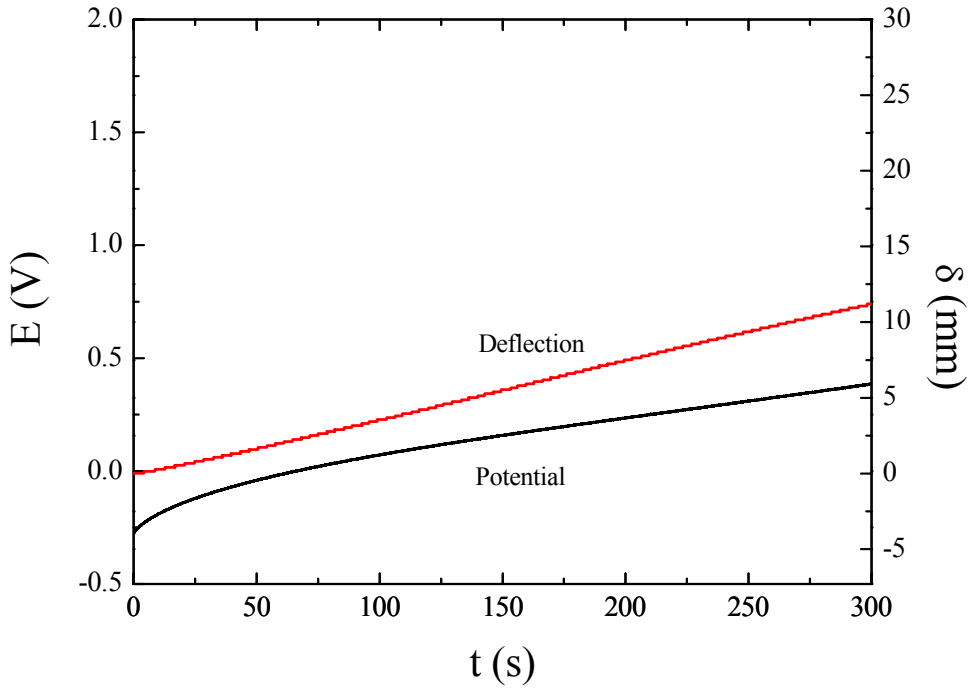

Figure 5.3. Time dependence of bending deflection of the platinum-IPMC upon constant applied current, +0.25 mA/cm^2.

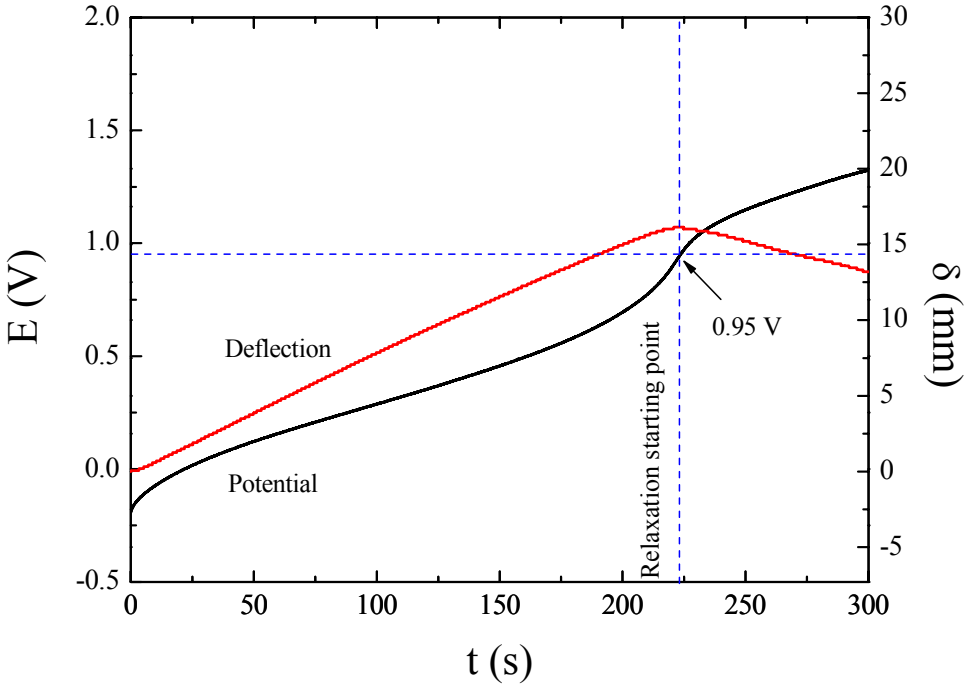

Figure 5.4. Time dependence of bending deflection of the platinum-IPMC upon constant applied current, +0.5 mA/cm^2.

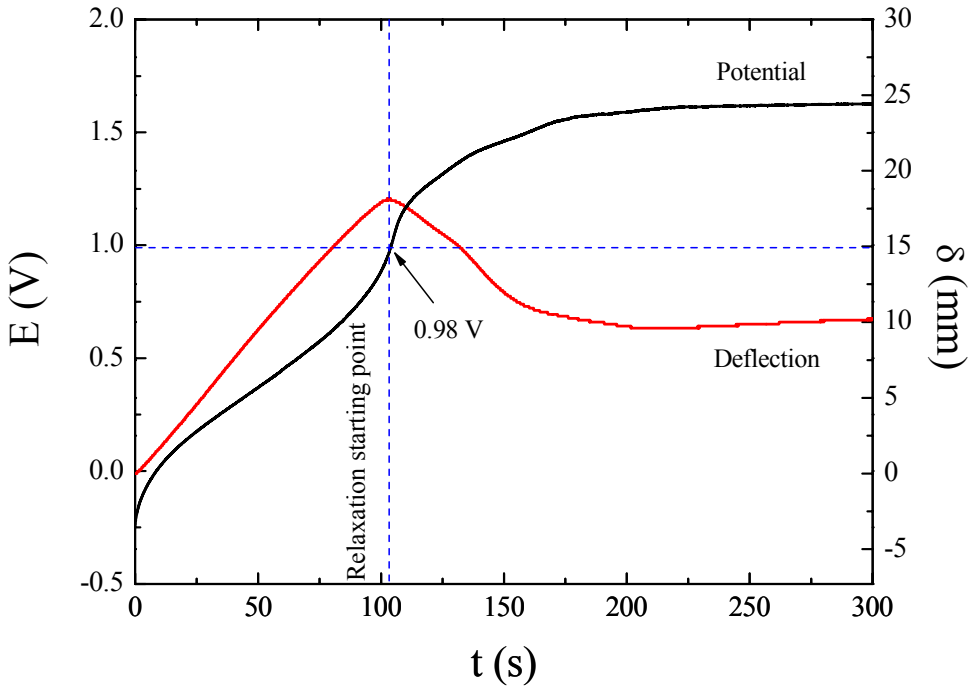

Figure 5.5. Time dependence of bending deflection of the platinum-IPMC upon constant applied current, 1.25 mA/cm^2.

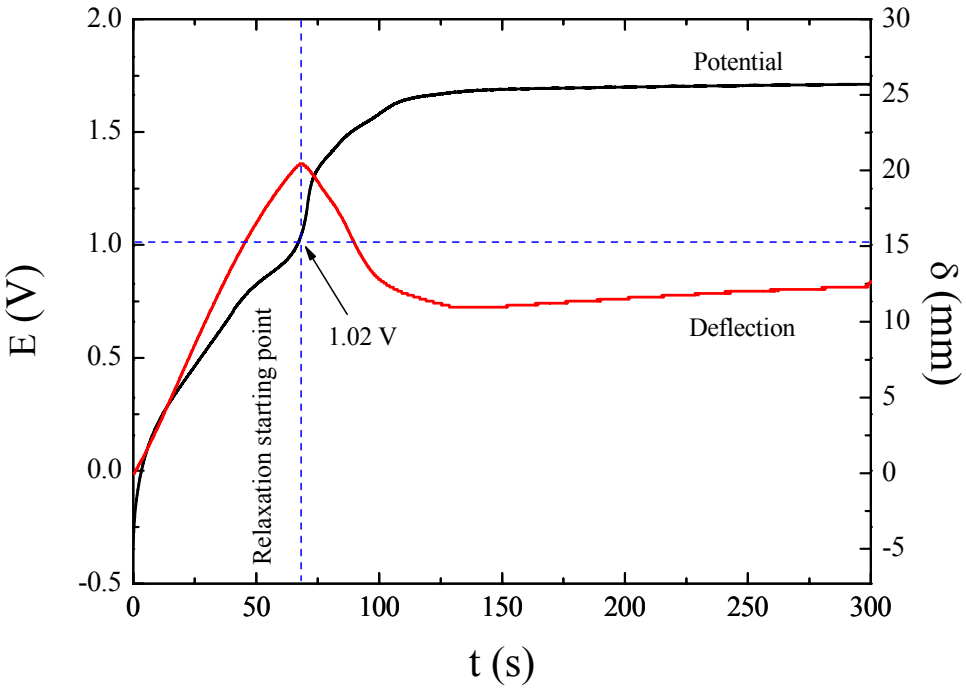

Figure 5.6. Time dependence of bending deflection of the platinum-IPMC upon constant applied current, 2.5 mA/cm^2.

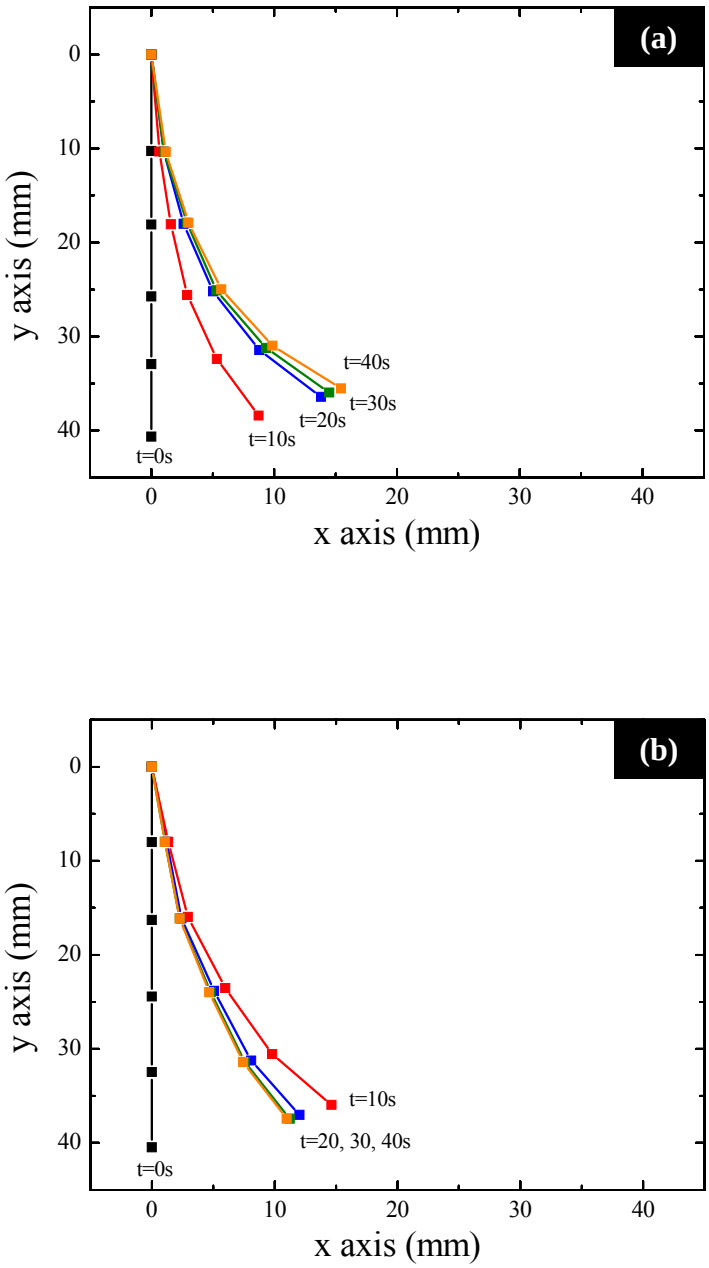

Figure 5.7. Experimental bending curves for the hydrated platinum-IPMC in air (a) *vs.* in water (b) under applied potential of +1.5V.

5.3. Room temperature ionic liquid (RTIL) as a solvent for IPMC

In order for an IPMC to show bending motion, the IPMC must include cations in the membrane due to the underlying mechanism of an IPMC actuator. A water-based solution is used as a solvent during the testing. When the IPMC needs to operate in air, the water will evaporate from the membrane over time. This problem makes in-air operation difficult for the long-term use. Moreover, a hydrated IPMC has a low electrochemical stability, as explained in Chapter 4. When operating in water, an undesirable characteristic of the IPMC causes power loss and degradation in performance due to unwanted electrochemical reactions, such as oxidation of the electrode materials and hydrogen/oxygen evolution during actuation and result in relaxation phenomena of the IPMC.

RTILs are molten salts made up of dissociated cations and anions. RTILs are salts with melting points below room temperature. Typical cations are substituted imidazolium ions and tetraalkylammonium ions, for example 1-butyl-3-methylimidazolium and trioctyl-methyl-ammonium. Typical anions are bis((trifluoromethyl)sulphonyl)imide (TFSI), tetrafluoroborate (BF_4^-), hexafluorophosphate (PF_6^-), , heptafluorobutanate (EH), trifluoromethylsulphonyl (TF), hexafluoroantimonate (SbF_6^-), and tetraphenylborate [$B(C_6H_5)_4^-$]. Liquids that contain these ions have low or negligible vapor pressure at room temperature and therefore evaporate much more slowly than water [111, 112]. They also have a wide window of electrochemical stability, good electrical conductivity, high ionic mobility, and excellent chemical and thermal stabilities [113, 114]. The electrochemical windows of RTILs can reach values of more than 4 ~ 5 V on platinum and gold [115].

The 1-butyl-3-methylimidazolium hexafluorophosphate ([bmim][PF6]) is historically one of the most important and most commonly investigated RTILs [116]. This study focuses on the use of [bmim][PF_6] as a solvent of IPMC. The physicochemical properties of [bmim][PF_6] are summarized in Table 5.1 and the chemical structure of [bmim][PF_6] is shown in Figure 5.8.

Table 5.1. Physicochemical properties of [bmim][PF_6].

Properties	Units	Value	Reference
Molecular weight	g/mol	284	[113]
Density	g/cm^3	1.362-1.370	[113, 114]
Viscosity	cP	371	[114]
Melting point	˚C	-61	[114]
Solubility in water	g/l	18	[113]
Water content at saturation	g/l	19	[113]
Specific conductivity	mS/cm	1.5	[114]
Maximum UV absorbance	nm	210	[113]
Thermal stability		starts to decompose at 180 ~ 200˚C	[113, 117]
vapor pressure at 25˚C	Pa	10^{-10}	[117]
Electrochemical window	V	4 ~ 5	[115, 118]

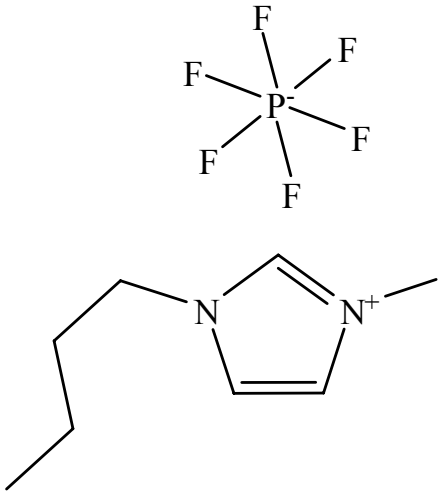

(a)

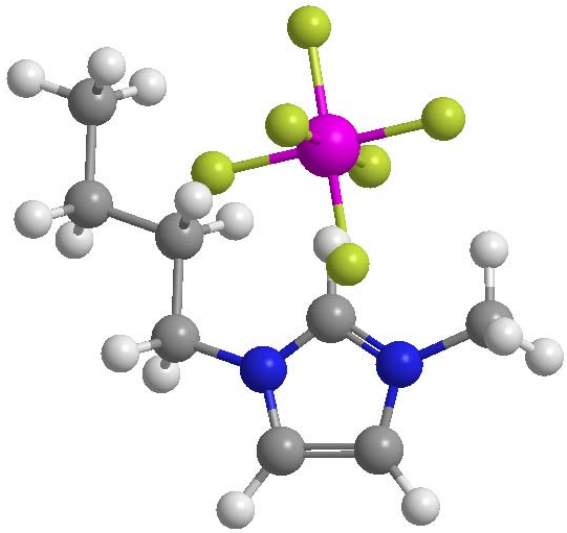

(b)

Figure 5.8. The general chemical formula (a) and three-dimensional structure (b) of 1-butyl-3-methylimidazolium hexafluorophosphate.

5.4. RTIL-IPMC for in-air operation

In order to prepare an IPMC solvated with [bmim][PF_6], initially the sample was dried in an oven at 60˚C under vacuum. The dried IPMC sample was then immersed in [bmim][PF_6] and a methanol-water mixture (1:1) at room temperature. Finally, the IPMC solvated with [bmim][PF_6] was dried in an oven at 60˚C for 30 minutes to eliminate moisture. Figure 5.9 shows cyclic voltammograms of a RTIL-IPMC within different potential ranges. It is interesting to note that the RTIL-IPMC showed a smaller bending motion than hydrated IPMCs under low potential (less than $\pm$ 1 V); however, the RTIL-IPMC under a higher potential (more than $\pm$ 1 V) shows a much larger bending motion than the water system. This result is believed to be due to the insufficient movement of large 1-butyl-3-methylimidazolium ions under low voltage. Under enough applied power, such a large ion can move easily toward the cathode side and make the Nafion™ increase the volume quickly. Figure 5.10 shows a galvanostatic cyclic voltammogram of a platinum-IPMC solvated with [bmim][PF_6] with a scan rate of 1 mA/s. In the RTIL system, a smaller applied current is required to obtain a larger bending motion than in hydrated IPMC system. Figure 5.11(a) provides comparative cyclic voltammograms for the platinum-IPMC solvated with [bmim][PF_6] and with water in the range of $\pm$ 2 V. The resulting data show that the surface reaction does not occur in [bmim][PF_6] within these operating potentials. There will is significantly less power loss in an RTIL system during actuation. In addition, in Figure 5.11(b), IPMC solvated with [bmim][PF_6] does not show relaxation phenomena. Figure 5.12 shows the IPMC bending motion under constant potentials, +1 V to +4 V. In the RTIL system, the IPMC deflections continuously increase, without relaxation for in-air operation. Seemingly, the RTIL system showed not

only a larger and more stable bending motion but also eliminated the relaxation phenomena.

The performance of IPMCs solvated with [bmim][PF_6] was examined by measuring the blocking force in a cantilever configuration, as shown in Figure 3.13, using a 10g-load cell. The actuation performance of the platinum-IPMC solvated with [bmim][PF_6] is given in Figure 5.13 with measured blocking forces as a function of the length of the samples during an LSV with a scan rate of 20 mV/s. The 10 mm-length IPMC solvated with [bmim][PF_6] exhibited larger blocking forces, about 3.0 mN. It is important to note that IPMCs generated monotonically an increase in the blocking forces, and there was no relaxation. By varying the scan rate applied in the course of the experiment, the potential scale of the blocking force was able to be explored. In Figure 5.14, the blocking forces were measured during an LSV with five different scan rates in the range of 0 V to +4 V. Maximum current and blocking force of the IPMC solvated with [bmim][PF_6] are summarized as a function of potential, in Table 5.2. IPMCs solvated with [bmim][PF_6], with lower scan rates, generate larger blocking forces. It can be determined that lower scan rates allow sufficient migration time of the [bmim] ions within the membrane. These ions lead to a larger force of IPMC. Figure 5.15 presents comparison of deflection of the hydrated platinum-IPMC and the platinum-IPMC solvated with [bmim][PF_6] under constant potential of +2 V. The IPMC solvated with [bmim][PF_6] shows a larger bending, but there is no relaxation during actuation.

In order to measure a relaxation potential and compare at potential with the potential of hydrated IPMC, potential-current curves were obtained during CPs. Figure 5.16 ~ Figure 5.18 showed the chronopotentiograms and corresponding deflections of

IPMC with different applied currents. In Figure 5.18, the IPMC deflections continuously increased in the RTIL system without relaxation in spite of overpotentials of +3.7 V. A maximum stain of 1.58 % was observed. The RTIL system showed not only a larger and more stable bending motion but also seemingly eliminated the relaxation phenomena.

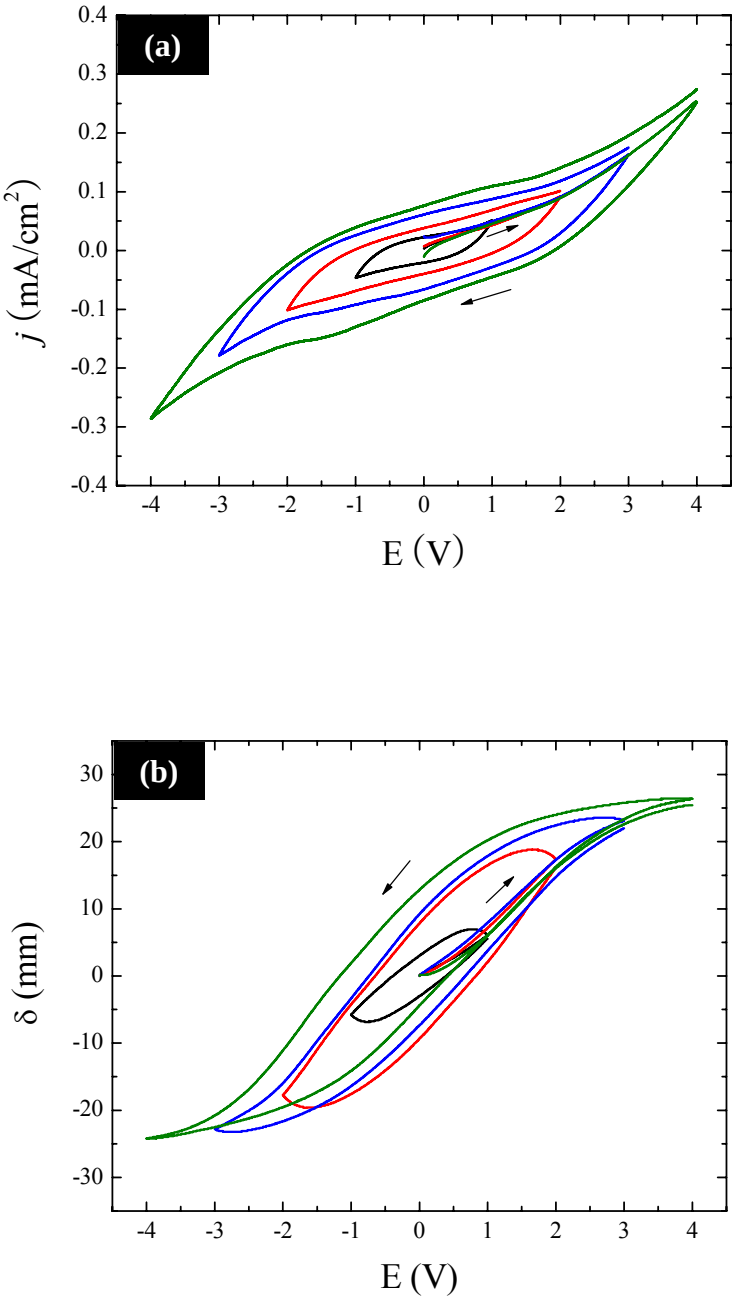

Figure 5.9. Two-electrode cyclic voltammograms of the platinum-IPMC solvated with [bmim][PF_6] with different potential ranges (scan rate of 20 mV/s).

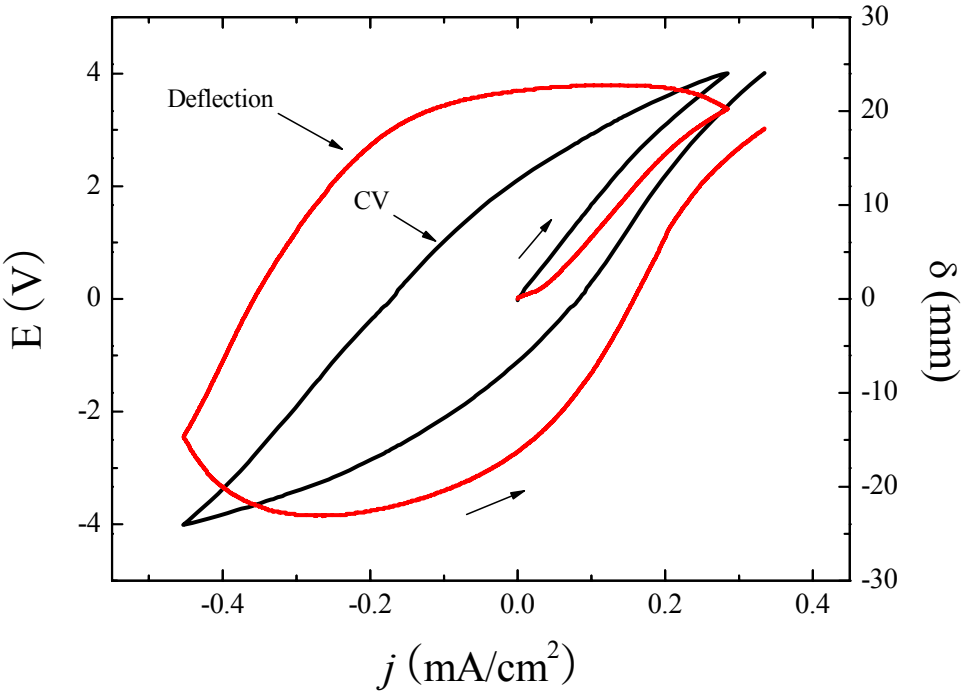

Figure 5.10. Galvanostatic cyclic voltammogram and deflection data of the platinum-IPMC solvated with [bmim][PF_6] (scan rate of 1 mA/s).

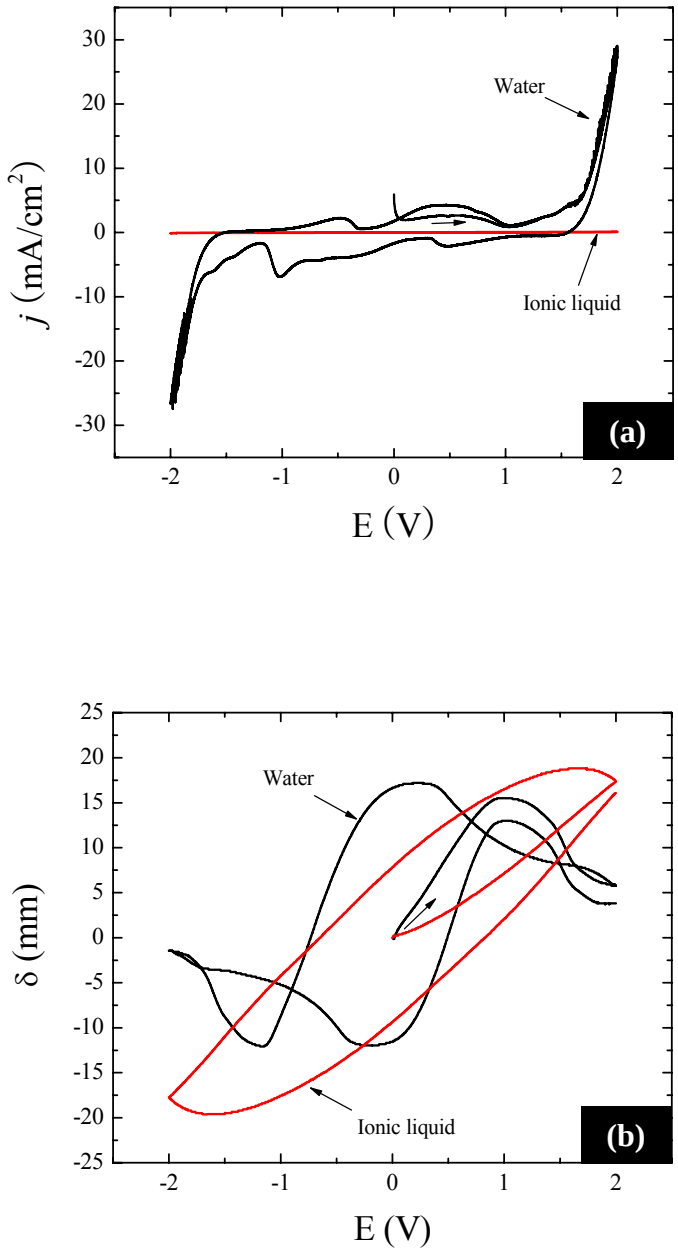

Figure 5.11. Cyclic voltammograms (a) and corresponding deflections (b) of the IPMCs solvated with [bmim][PF_6] and solvated with water in the range of ± 2V (scan rate of 20 mV/s).

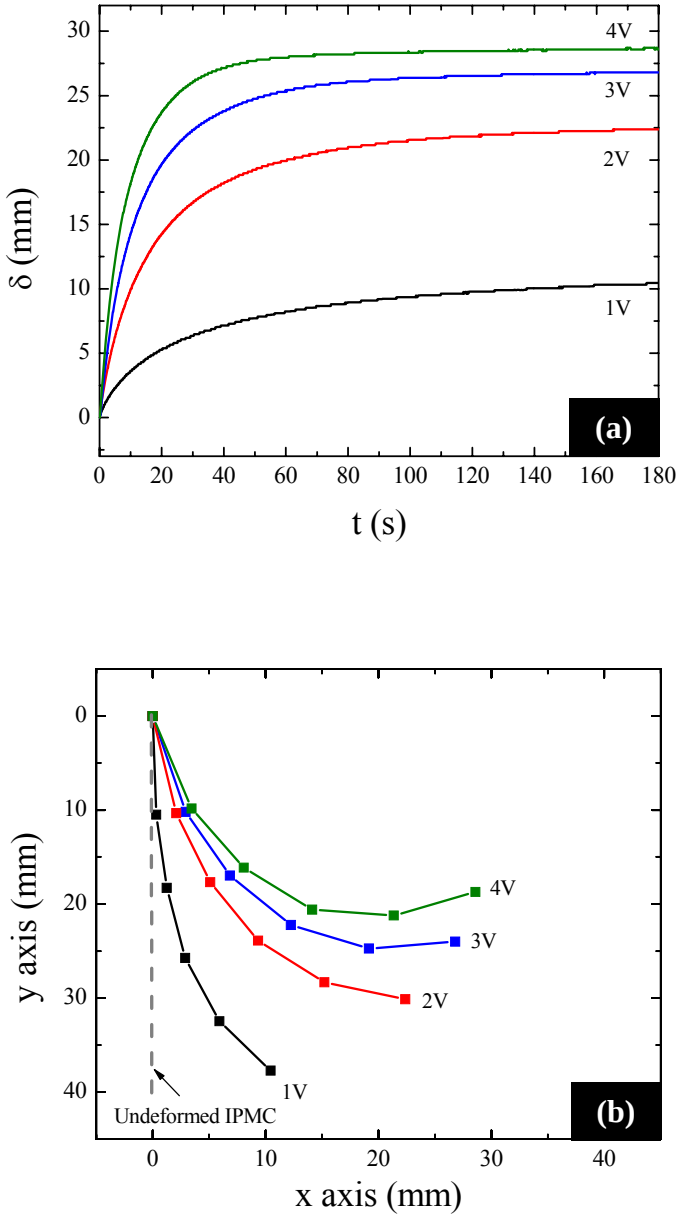

Figure 5.12. Time dependence of bending deflection (a) and maximum deflection at 180 s (b) of the IPMC solvated with [bmim][PF_6] upon constant applied potentials, +1 V ~ +4 V.

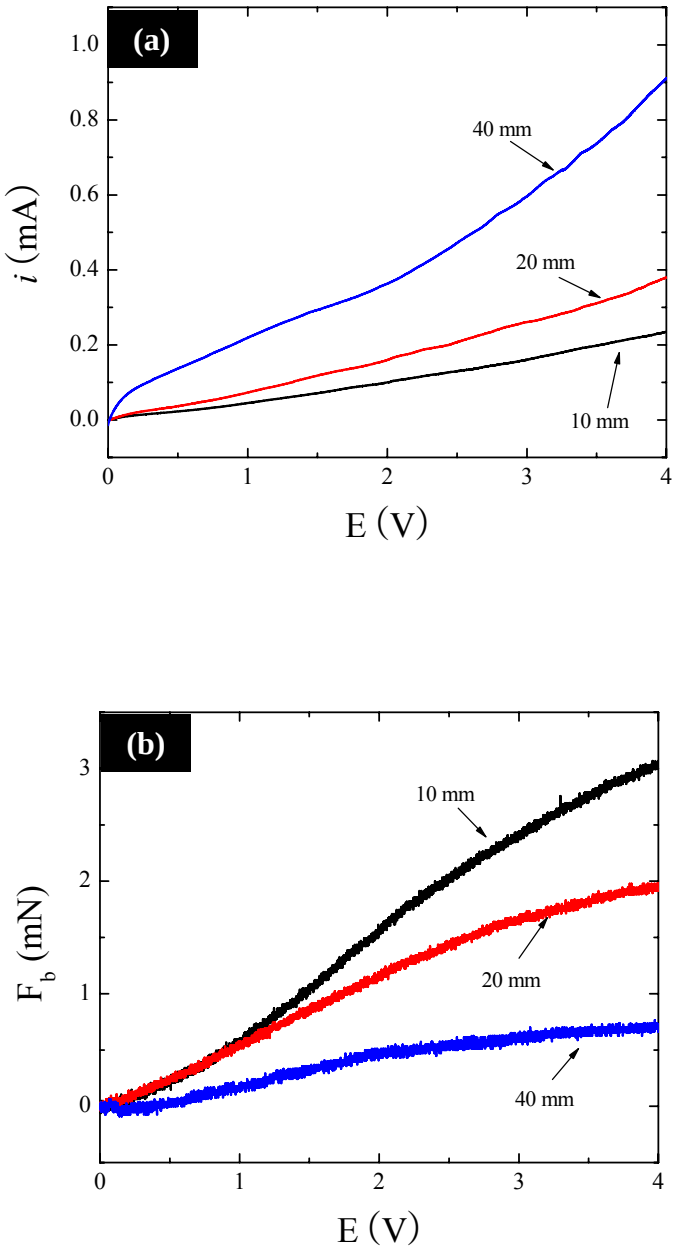

Figure 5.13. Linear sweep voltammograms (a) and corresponding blocking forces (b) of the IPMCs solvated with [bmim][PF_6] with three different lengths (scan rate of 20 mV/s).

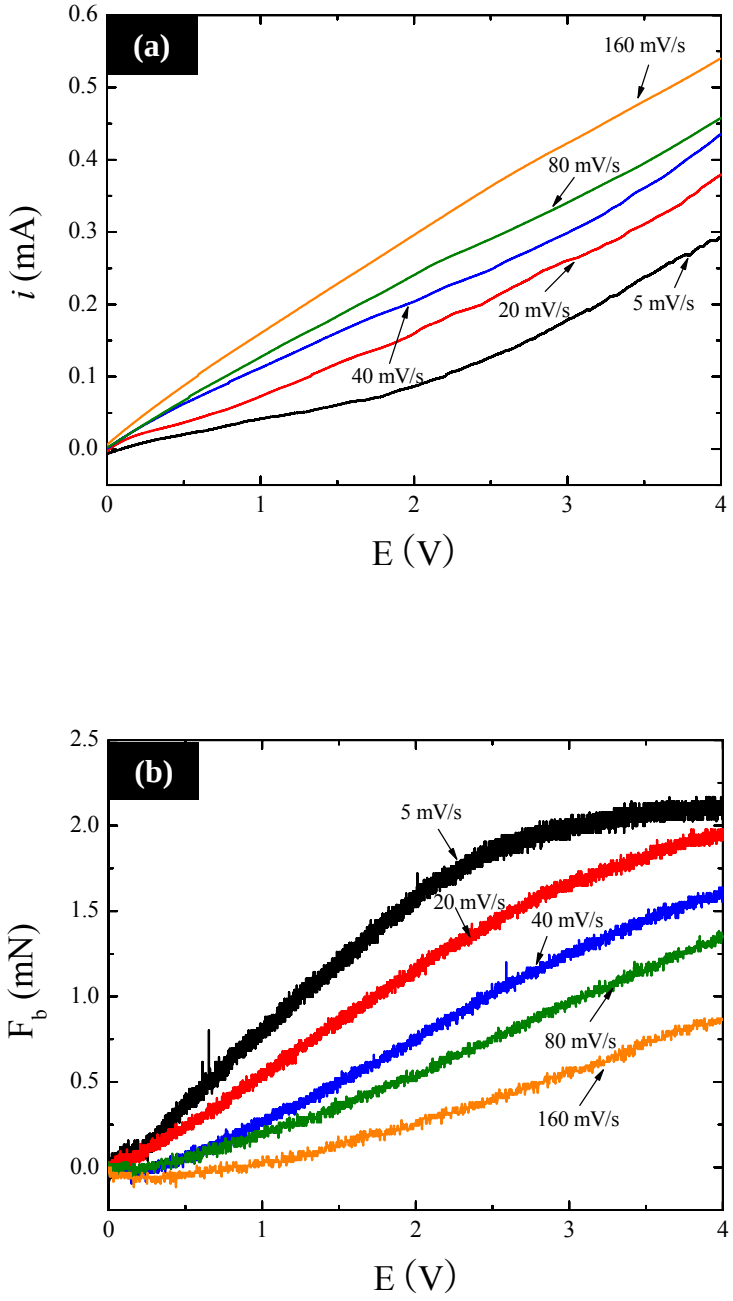

Figure 5.14. Linear sweep voltammograms (a) and corresponding blocking forces (b) of the platinum-IPMC solvated with [bmim][PF_6] with five different scan rates.

Table 5.2. Maximum current and maximum blocking force of the IPMC solvated with [bmim][PF_6] at under applied potential of +4 V with different scan rates.

scan rate (mV/s)	5	20	40	80	160
i_{max} (mA)	0.29	0.38	0.44	0.46	0.54
$F_{b,max}$ (mN)	2.10	1.96	1.58	1.35	0.87

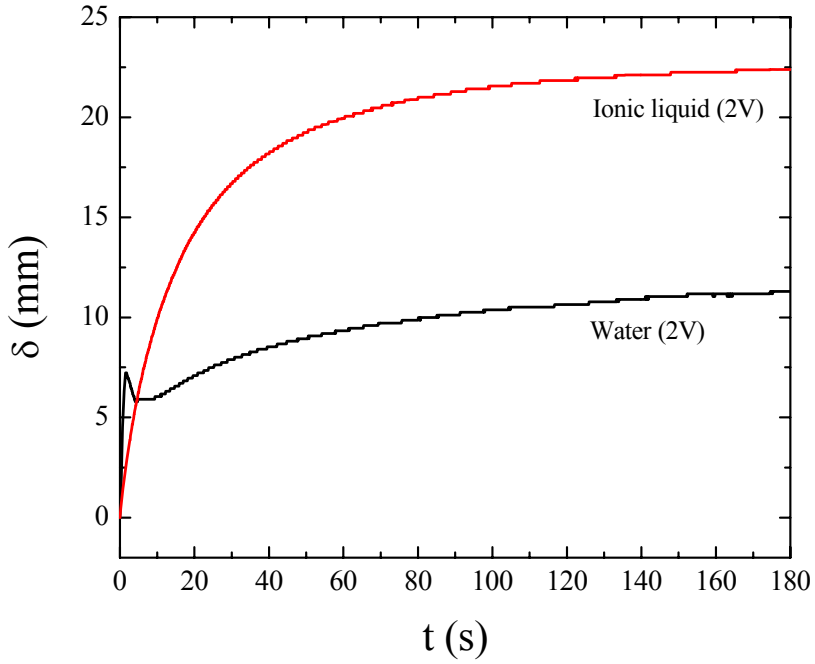

Figure 5.15. Bending deflection of the IPMCs solvated with [bmim][PF_6] and solvated with water under applied potential of +2V.

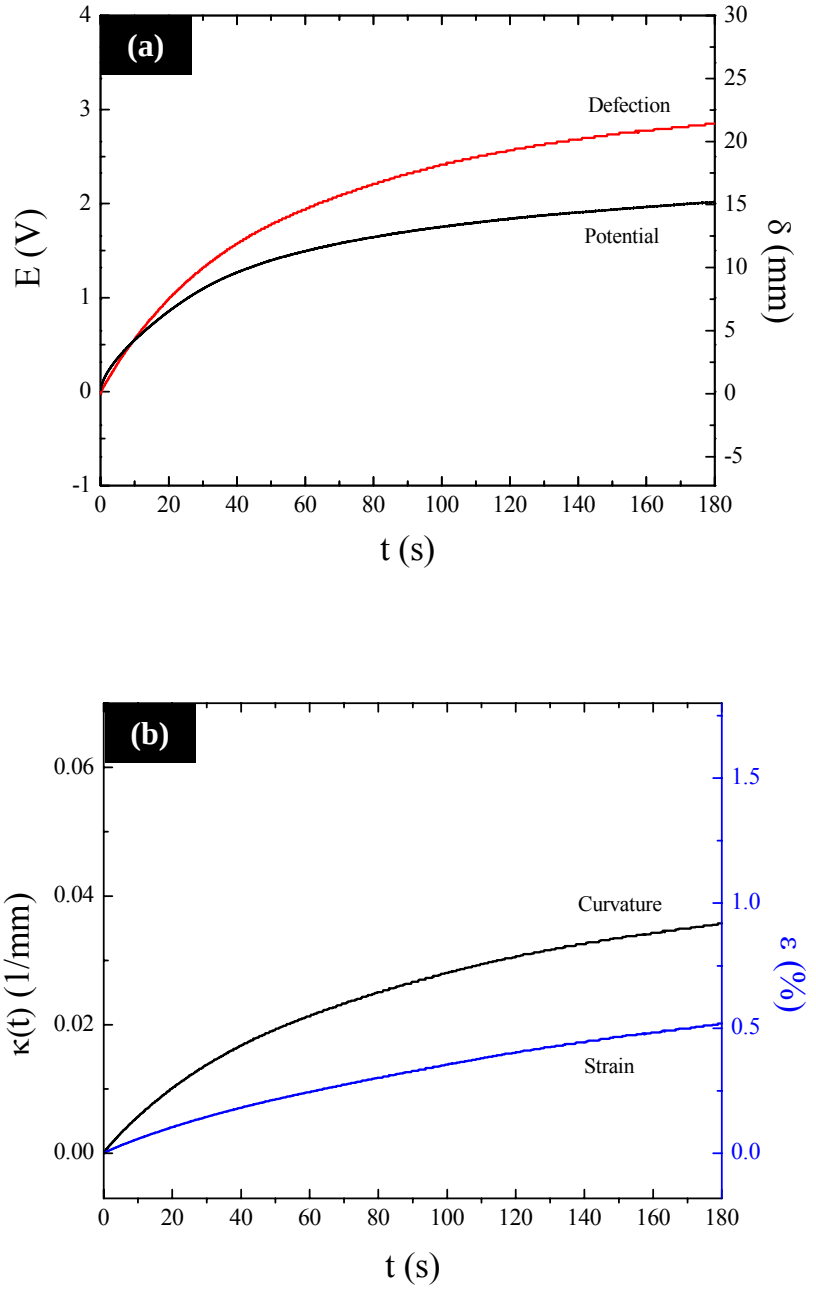

Figure 5.16. Time dependence of bending deflection of the IPMC solvated with [bmim][PF_6] upon constant applied current, +0.05 mA/cm^2.

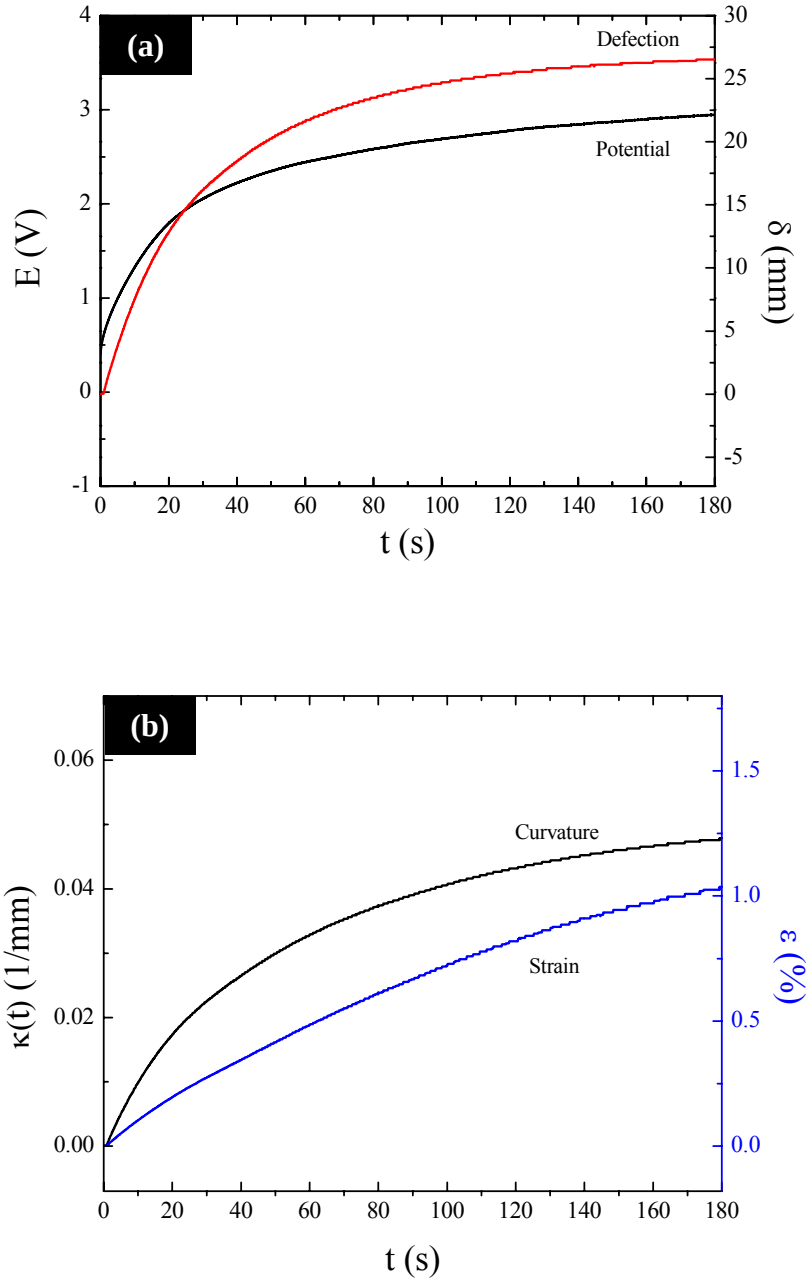

Figure 5.17. Time dependence of bending deflection of the IPMC solvated with [bmim][PF_6] upon constant applied current, +0.1 mA/cm^2.

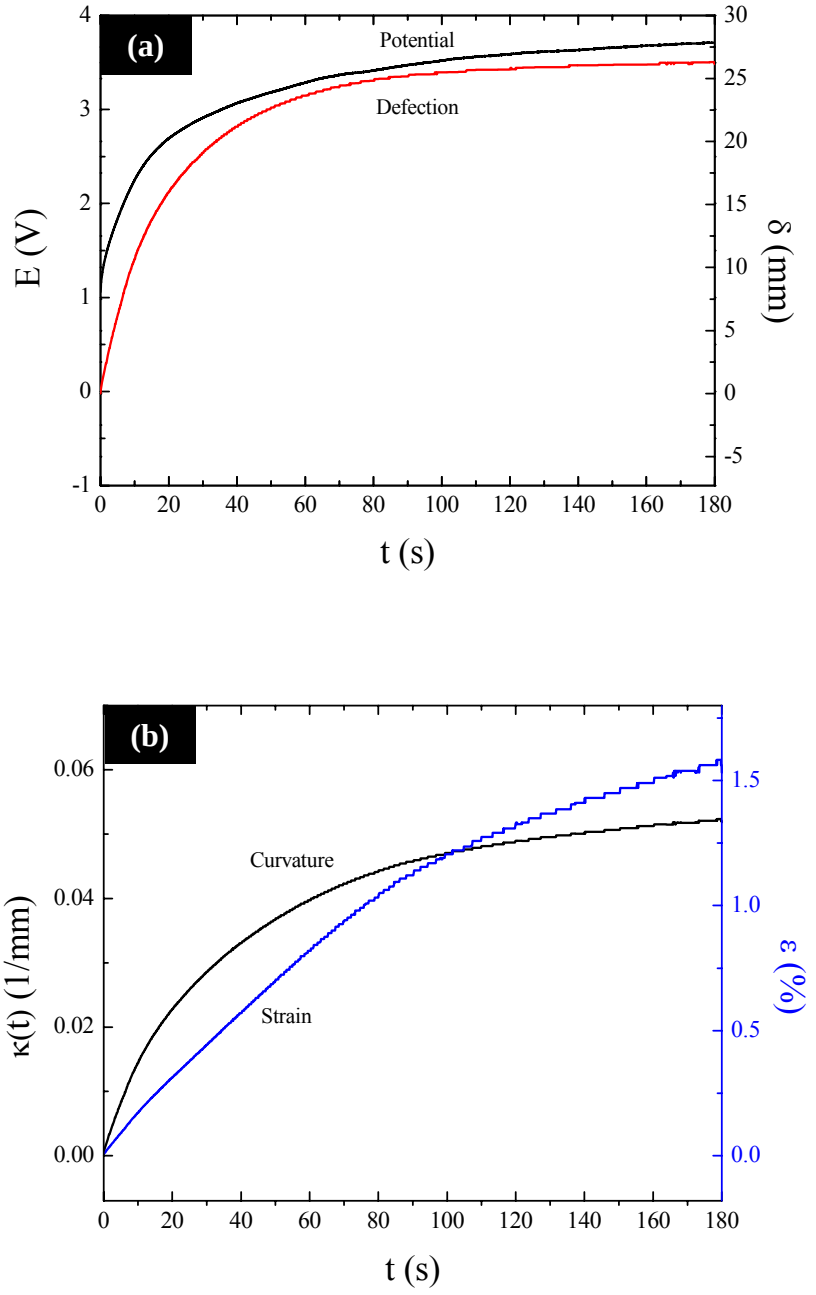

Figure 5.18. Time dependence of bending deflection of the IPMC solvated with [bmim][PF_6] upon constant applied current, +0.15 mA/cm^2.

5.5. IPMC efficiency

Experimentally measured electrical to mechanical conversion efficiency is reported only by Shahinpoor and Kim [16]. They obtained the optimum values of the IPMC's efficiency at approximately 5 ~ 10 Hz. The values were approximately 2.5 ~ 3.0 %. In this section, using a method different from Shahinpoor and Kim, the efficiency with which electrical energy is converted into mechanical work is presented for the evaluation of the performance IPMCs.

Generally, in resistive circuits, instantaneous electrical input power is calculated using Joule's Law.

$$P_{in} = i \cdot E \tag{5.1}$$

where P_{in} is electrical power input in watts (W), i is current in amperes, and E is potential in volts.

The strain-energy density in J/m^3 can be defined by [119]

$$u = \frac{Y \cdot \varepsilon^2}{2} \tag{5.2}$$

where u is the strain-energy density, Y is Young's modulus, and ε is bending strain.

Mechanical power output (P_{out}) is

$$P_{out} = \frac{(u_f - u_i) \cdot V}{t} = \frac{Y \cdot \varepsilon^2 \cdot V}{2t} \tag{5.3}$$

where P_{out} is the mechanical power output to the IPMC, u_f is final strain-energy density, u_i is initial strain-energy density, and V is the volume of the IPMC.

Therefore, the efficiency of electrical to mechanical energy conversion is:

$$e = \frac{\text{Power output (mechanical)}}{\text{Power input (electrical)}} \times 100 = \frac{P_{out}}{P_{in}} \times 100 = \frac{Y \cdot \varepsilon^2 \cdot V}{2E \cdot i \cdot t} \times 100 \tag{5.4}$$

Figure 5.19 shows the efficiency of the IPMC solvated with [bmim][PF_6] and the hydrated IPMC during chronoamperometry. A maximum efficiency of the IPMC solvated with [bmim][PF_6] is obtained around 50 ~70 s. The efficiency increases with increasing applied potentials. The maximum efficiency under +4 V of applied potential is 22.8 %. The maximum efficiency of the hydrated IPMC, 1.74 % is obtained under +1.5 V of applied voltage. The hydrated IPMC shows much lower efficiency. Under +1.5 V of applied potential, the IPMC shows a higher efficiency at the initial stage, but the efficiency decrease with time due to the relaxation. Under +2 V of applied voltage, the IPMC shows drastically lower efficiency due to the electrolysis of water. Apparently, the efficiency of IPMCs is significantly improved in an RTIL system. The hydrated IPMC consumes input power in electrochemical reactions during actuation. There is approximately eight times increase in maximum efficiency of the IPMC for the [bmim][PF_6] system when compared with both samples under +1V of applied potential.

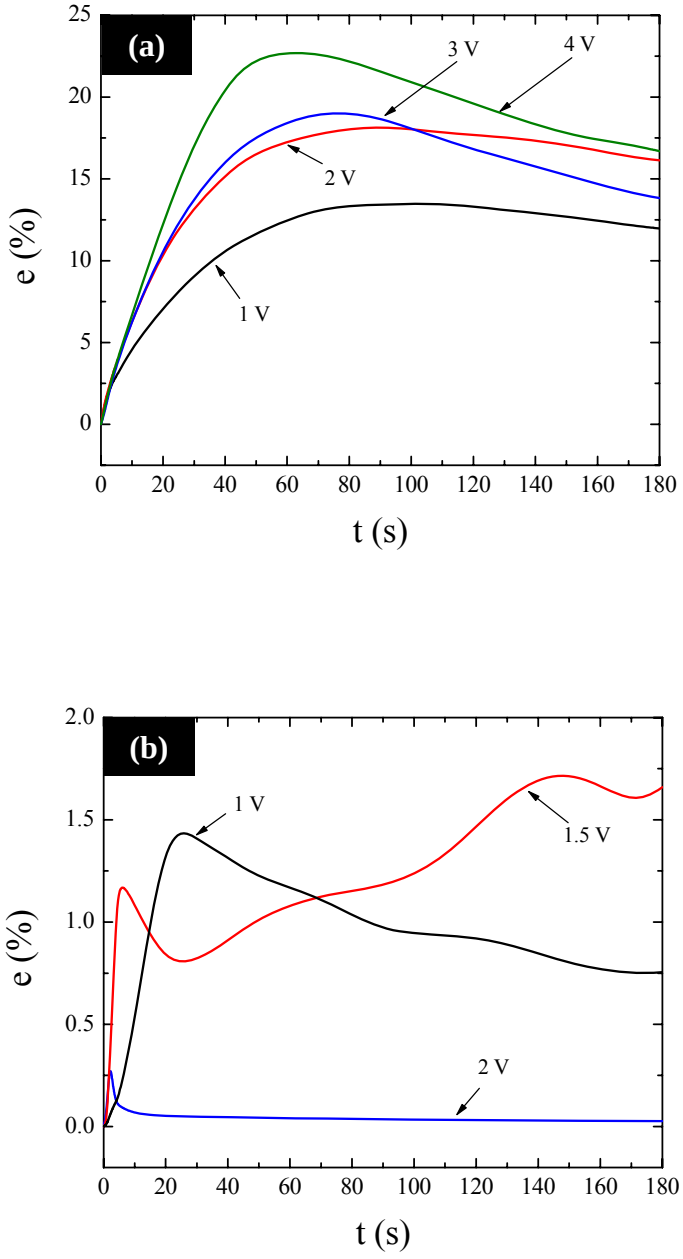

Figure 5.19. Efficiency of the IPMCs solvated with [bmim][PF_6] (a) and solvated with water (b).

CHAPTER 6:

SELF-OSCILLATORY BEHAVIOR OF IPMC

Biological systems often exhibit rhythmic phenomena at all levels. Their time scale ranges from less than a second to years. Obviously, it has been a great challenge to understand the periodic behavior of biological systems because of this. In this chapter, an intriguing new feature of the IPMC, "spontaneous rhythmic motion," is introduced. A surface modification technique that provokes a self-oscillatory motion of IPMCs is investigated.

6.1. Electrochemical oscillation

Spontaneous oscillations are a widespread phenomenon in electrochemistry and have been observed in a large number of experimental systems such as the oxidation of metals and organic materials [120-133]. Electrochemical systems exhibiting instabilities often behave like activator-inhibitor systems, whereby the electrode potential is an essential variable and takes on the role either of the activator or of the inhibitor. An activator-inhibitor system may generate oscillations in a certain condition if the time scale of the inhibitor is slower than the that of the activator [134]. The oscillations are decisively influenced by the control of the reactions via the external applied voltage or current. The great variety of electrochemical oscillation systems indicates that oscillations are not a specific, but a general phenomenon. In the electrocatalytic oxidation

of small organic molecules, the oscillatory behavior of current and potential were observed [122, 125, 135-138]. Figure 6.1 shows the CV on a platinized platinum electrode with different concentrations of HCHO, 0.05 M, 0.1 M, and 1 M. The cyclic voltammogram clearly shows two defined sets of peaks. The first peaks start at approximately +0.48 V on the anodic scan on all graphs; however, the potentials of the second peaks on the cathodic scan show different values of +0.87 V, +0.53 V, +0.46 V, respectively. The first peaks correspond to the oxidation of oxide layers on the platinum electrode surface ($Pt\text{-}OH_{ads}$) and the second peaks correspond to the oxidation of carbon monoxide (CO) to carbon dioxide gas (CO_2). The CO reaction rate increases with an increasing concentration of HCHO. Among the three solutions, only 1 M HCHO showed oscillation peaks during CV. The range of oscillation was between + 0.55 and +0.75 V in the cathodic direction. The oscillation phenomena require sufficient concentration of HCHO and are then able to generate oscillations in a certain range. Thus, the time scale of the inhibitor, such as CO and OH, is slower than that of the activator, such as platinum. Figure 6.2 also shows the cyclic voltammograms of a platinum-IPMC with three different concentrations. The oscillation peaks and the number of peaks increase with an increasing concentration of HCHO.

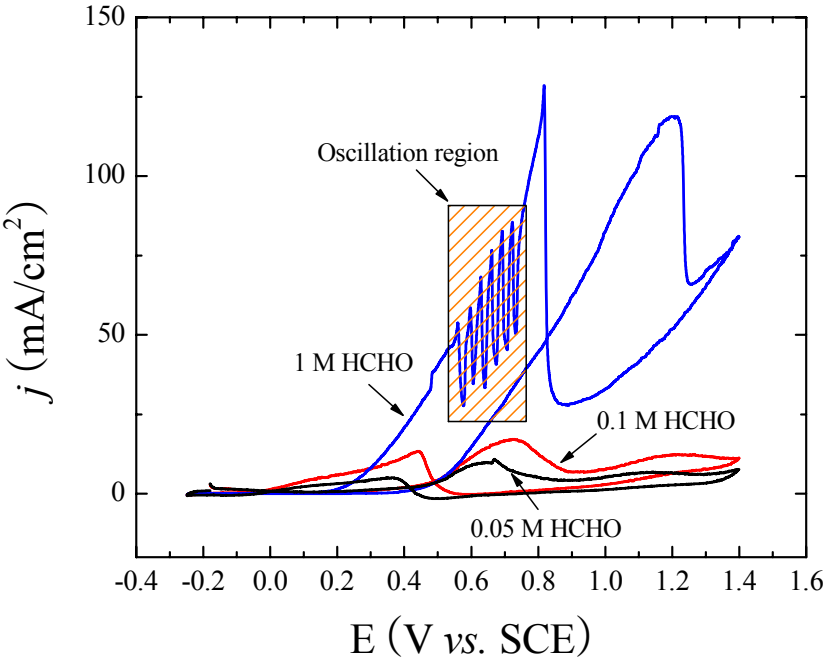

Figure 6.1. Cyclic voltammograms of the platinized platinum in 0.05 M, 0.1 M, and 1 M of HCHO + 1 M H_2SO_4.
*Note that the surface area of platinum in this experiment was 0.197 cm^2.

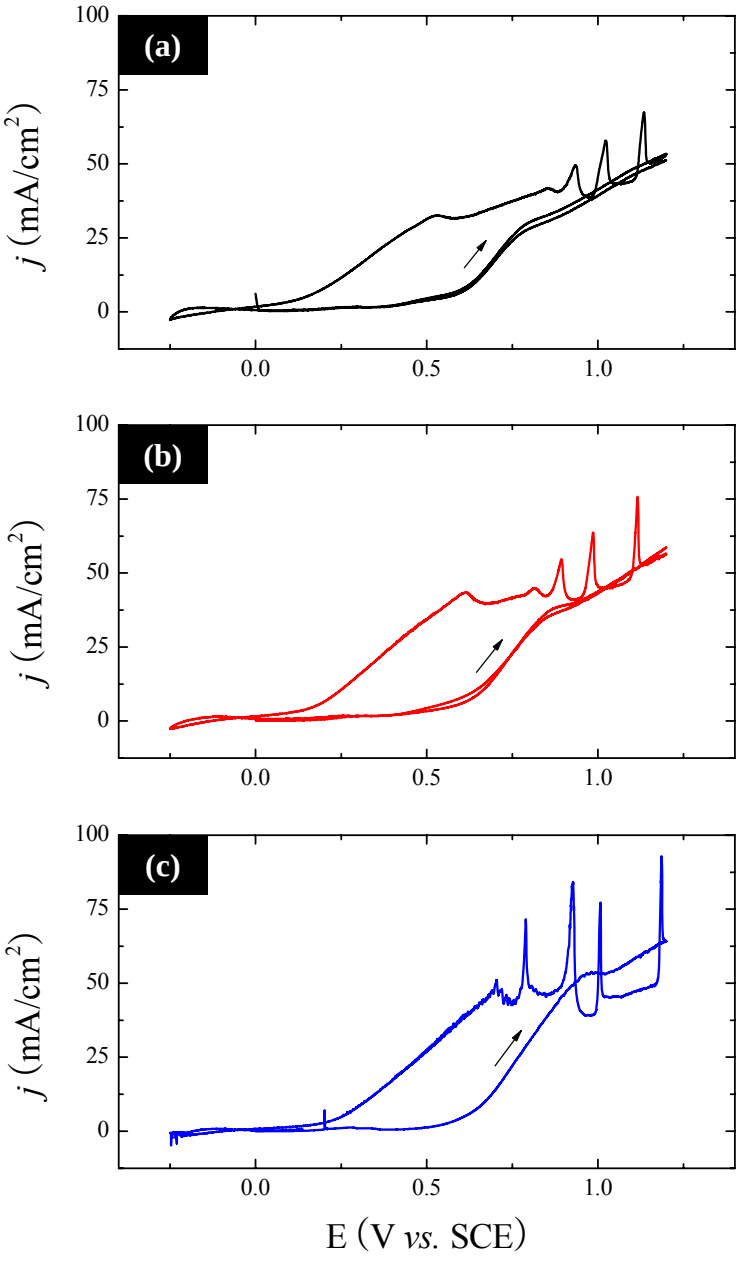

Figure 6.2. Cyclic voltammograms of the platinum-IPMC in 1 M (a), 2 M (b), and 3 M (c) HCHO + 3 M H_2SO_4 (scan rate of 20 mV/s).

6.2. The origin of self-oscillation

The oscillations in the presence of small organic molecules, such as HCHO, are caused by the potential or current periodicity in the electrode where the activation overpotential is altered by complex surface reactions under an applied DC current. The anodic oxidation of HCHO on a platinum surface is accompanied by the appearance of intermediate species *i.e*., CO and OH [137]. Therefore, the overall reaction, which involves the reaction of Pt-OH_{ads} with the intermediate Pt-CO_{ads} and the conversion of Pt-OH_{ads} to PtO, leads to the occurrence of complex voltammetric responses. The underlying mechanism of HCHO oxidation on a platinum surface, in aqueous electrolyte, can be elucidated [135, 137-140].

$$HCHO + * \rightarrow Pt - CHO_{ads} + H^+ + e^- \quad (6.1)$$

$$Pt - CHO \rightarrow Pt - CO_{ads} + H^+ + e^- \quad (6.2)$$

$$H_2O + * \leftrightarrow Pt - OH_{ads} + H^+ + e^- \quad (6.3)$$

$$CO_{ads} + OH_{ads} \rightarrow CO_2 + H^+ + e^- + 2* \quad (6.4)$$

where * denotes an actives site on the platinum surface and subscript ads indicates species adsorbed on the surface.

According to the cyclic voltammogram of HCHO in Figure 6.1 and Equations 6.1 ~ 6.4, HCHO is dissociated on the electrode surface at a lower anodic potential via a successive dehydrogenation processes. At a higher anodic potential than that of dehydrogenation potential, water oxidation takes place and shows an explosive nature of

interactions during the intermediate formation. CO molecules are formed during the HCHO dissociation and OH molecules are generated by the water oxidation. These two molecules tend to produce CO_2, H^+, and an electron.

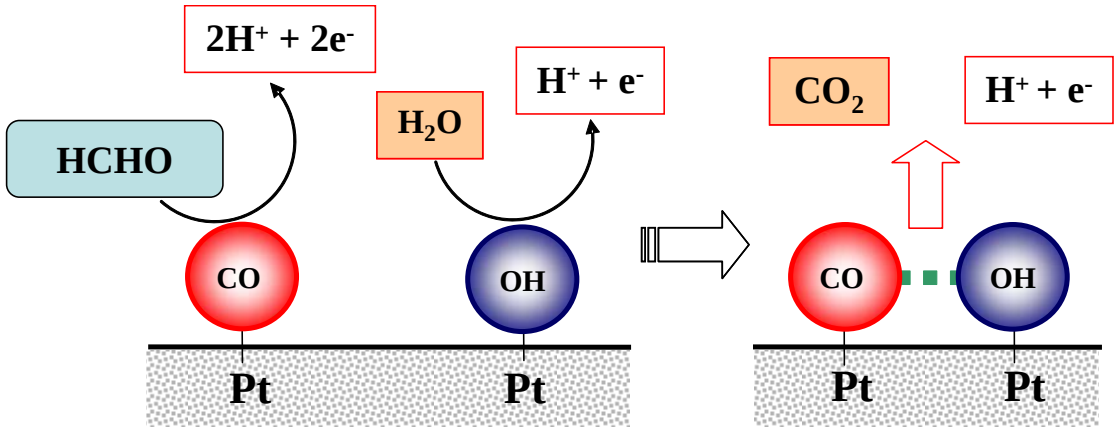

Figure 6.3. Illustration of a proposed mechanism of HCHO oxidation on a platinum surface in aqueous electrolytes.

Figure 6.4 shows the mechanistic origin of the electrochemical oscillations for HCHO using an LSV and an EQCM in the HCHO solution, respectively. The onset potential of current oscillations on the anodic scan was approximately +0.75 V. At the low outer-potential ranging between -0.2V and +0.3 V, the dissociation of HCHO (*i.e.*, dehydrogenation and CO adsorption) induces small anodic currents resulting in constant mass change. At approximately +0.45 V, the onset of HCHO oxidation (*i.e.*, CO oxidation) is observed, caused by the reaction with OH adsorbed resulting from the

oxidation of the surface water. Interesting to note is that from the anodic potential of approximately +0.75 V, one can clearly observe that current oscillations on the positive current-potential slope. In parallel, the mass oscillates on the anodic scan and the average value of mass change is approximately 125 ng. The initial burst of anodic current at +0.75V is due to the reaction (6.4), *i.e.*, CO_2 evolution presenting the clean platinum surface. The anodic current abruptly decreases, which could be due to the adsorption of intermediate specie (CO) on the surface. Between current decrease and second burst of current, the current slightly increased due to OH adsorption. The current increase induces the mass decrease and vice versa. Jackman *et al.* [141] experimentally observed that the saturation adsorption coverage of CO molecules was about 1.0×10^{15} atoms/platinum cm^2 and it is in agreement with theoretical value of 1.31×10^{15} atoms/cm^2.

An EIS has the usefulness of the studying oscillatory electrochemical systems. Figure 6.5(a) shows the Bode plot at the potential of +0.70 V. This profile adequately reveals that phase angle drastically changes from -180 ° to +180 ° at a frequency of 0.2 Hz. This drastic phase change results in a counter-clockwise profile, which negative real axis was intersected in the Nyquist plot, as shown in Figure 6.5(c). At the potential of +0.65 V, the impedance plot shown in Figure 6.5(b) exhibits a clockwise capacitive-inductive loop indicating dynamically-stable stationary operating points. Figure 6.5(c) shows that at the potential of +0.75 V, the impedance profile becomes counter-clockwise loop. The detailed shape of the Nyquist plot allows information to be gathered on the mechanistic origin of the oscillatory behavior, which can be used to predict the dynamical stability of oscillatory systems. Based on the electrochemical nature of the activatory and inhibitory variables and their interplay, electrochemical oscillators can be divided into

two classes. In the first class the positive feedback mechanism is due to a current potential characteristic. In the second class, the shape is hidden due to a different interplay of the electrochemical variables [142]. The model is classified as a hidden negative differential resistance (HNDR) oscillator based upon the dynamic response of the system. Experimental observations exhibit the HCHO oxidation on the platinum belonging to the HNDR oscillator.

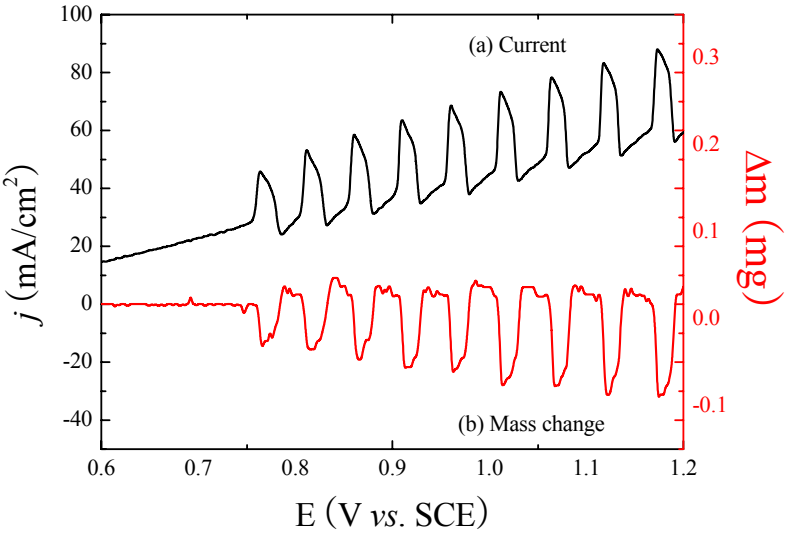

Figure 6.4. Linear sweep voltammogram (a) and *in-situ* mass change (b) of platinized platinum in 1 M HCHO + 1 M H_2SO_4 (scan rate of 20 mV/s) [135].

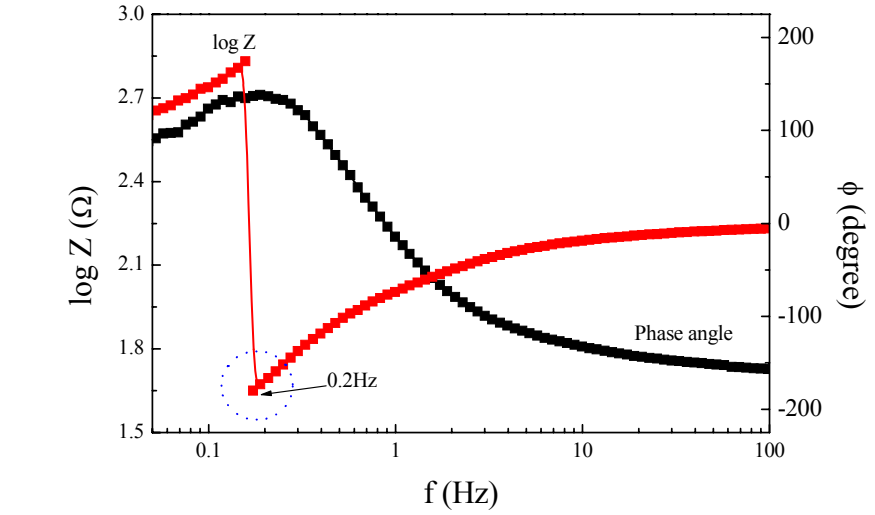

(a)

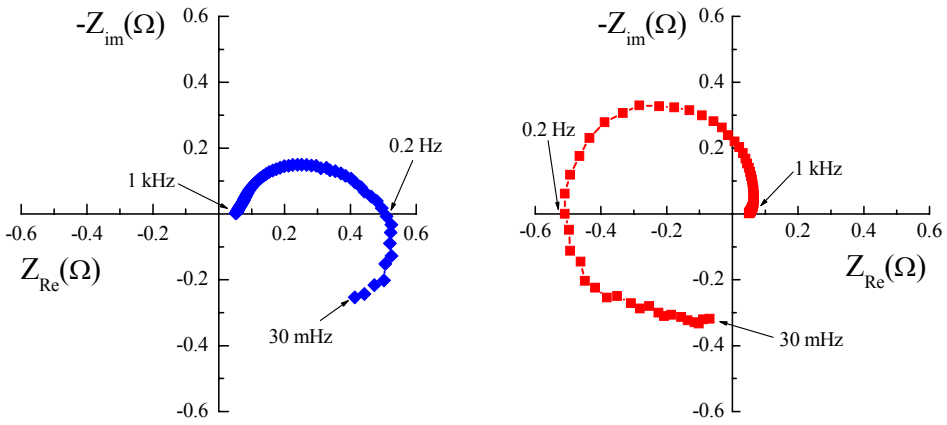

(b) (c)

Figure 6.5. Electrochemical impedance behavior of formaldehyde oxidation at a platinized platinum electrode: Bode plot (a) and Nyquist plots measured below (b) and at (c) oscillation potential [135] .

6.3. Self-rhythmic motion of IPMC

In general, when a constant electric field is imposed on IPMCs in the presence of small organic molecules, such as HCHO, IPMCs exhibit their periodic deformation due to the electrochemical oscillation. Figure 6.6 shows schematic illustrations of the conventional operation and the self-oscillatory operation of IPMCs. The self-oscillatory operation may allow us to simplify the driving electronics of IPMC systems and can lead to a significant reduction of the payload. Under a constant electric field, appropriately-conditioned IPMC systems exhibited a regular periodic bending movement. The self-oscillatory IPMC system, under specific conditions, could be a useful means to minimize the use of complex electronics in many engineering applications.

Figure 6.7(b) depicts the oscillatory mechanical deformation of the IPMC sample, while Figure 6.7(a) displays the potential oscillation during cyclic voltammetry. As mentioned in section 6.2, during the oxidation of formaldehyde, the intermediate (CO) of the reaction strongly binds to the platinum surface of the IPMC and blocks the active sites. Since platinum is particularly vulnerable to a poisoning effect, the platinum in both the anode and the cathode can be poisoned by CO in an acidic media. Platinum preferentially adsorbs OH, which then oxidizes the CO on adjacent platinum sites to CO_2. These simultaneous adsorption and desorption phenomena result in the oscillatory potentials. These potential can be used as a driving source of IPMCs.

In order to investigate oscillatory phenomena as a function of applied currents, CPs were conducted in three different concentrations of HCHO. Figure 6.8 ~ Figure 6.10 show the galvanostatic linear sweep voltammograms and corresponding deflections of a platinum-IPMC in three different concentrations of HCHO. The oscillations start at approximately

7 mA/cm^2. The results from the galvanostatic linear sweep voltammograms are redrawn in Figure 6.11. Figure 6.11 shows current dependence of oscillation frequency of the platinum-IPMC with three different concentrations of formaldehyde with scan rate of 1 mA/s. The frequency increase with an increasing current density and keep a constant value of approximately 0.11 ~ 0.13 Hz up to 14 mA/cm^2 for all three concentrations. After the current density of 14 mA/cm^2, in 1 M HCHO, the frequency decrease with an increasing current density; in 2 M HCHO, keep the constant value regardless an increasing current density; in 3 M HCHO, increase with an increasing current density.

Figure 6.12 ~ Figure 6.14 show chronopotentiograms and corresponding deflection data of a platinum-IPMC in three different concentrations of HCHO under constant current of 2.5, 5, 10, 20, and 40 mA/cm^2 with a scan rate of 1 mA/s. Maximum potential difference and maximum deflection difference of the oscillations with three different concentrations of HCHO are summarized in Table 6.1 and Figure 6.15. Maximum potential differences increase with an increasing current density up to 7 mA/cm^2 and keep almost constant values. Maximum deflection differences also increase with an increasing current density up to 7 mA/cm^2. However, maximum defection decreases with an increasing current density where the tests are completed. Base on the results, the largest deflection of 2.86 mm is obtained at 10 mA/cm^2 in 1 M HCHO.

A relationship between corresponding potential and deflection can be seen in Figure 6.16. As a result, the deflection of self-oscillatory IPMC is affected by the corresponding potential of the electrode surface, creating a linear relationship.

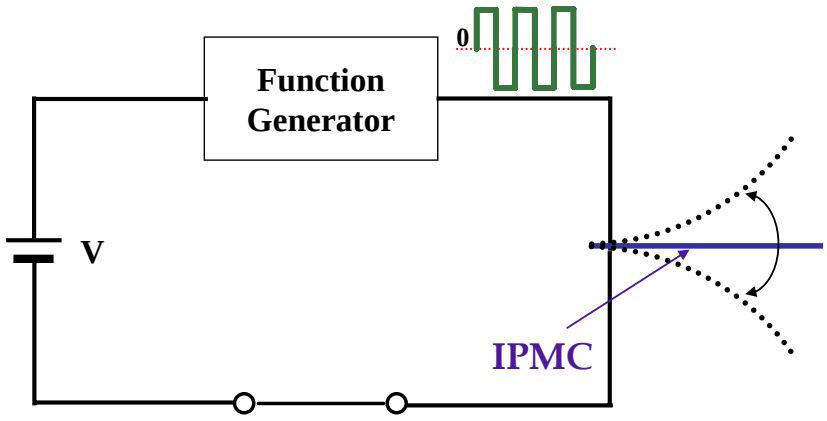

(a)

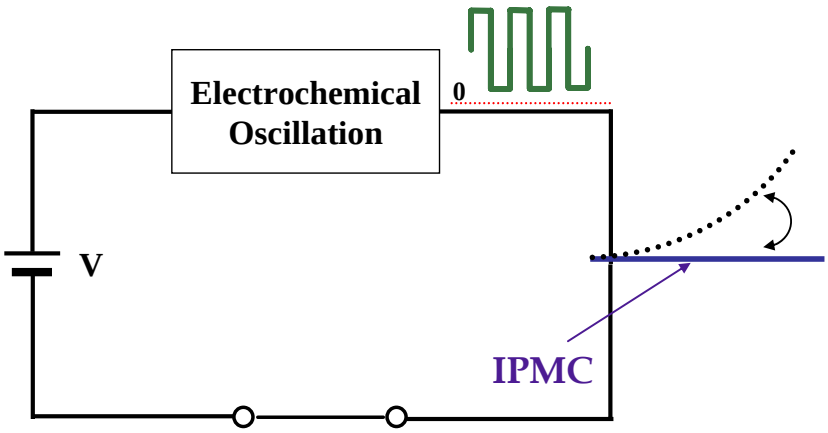

(b)

Figure 6.6. Schematic illustrations of conventional (a) and self-oscillatory (b) operations of IPMCs.

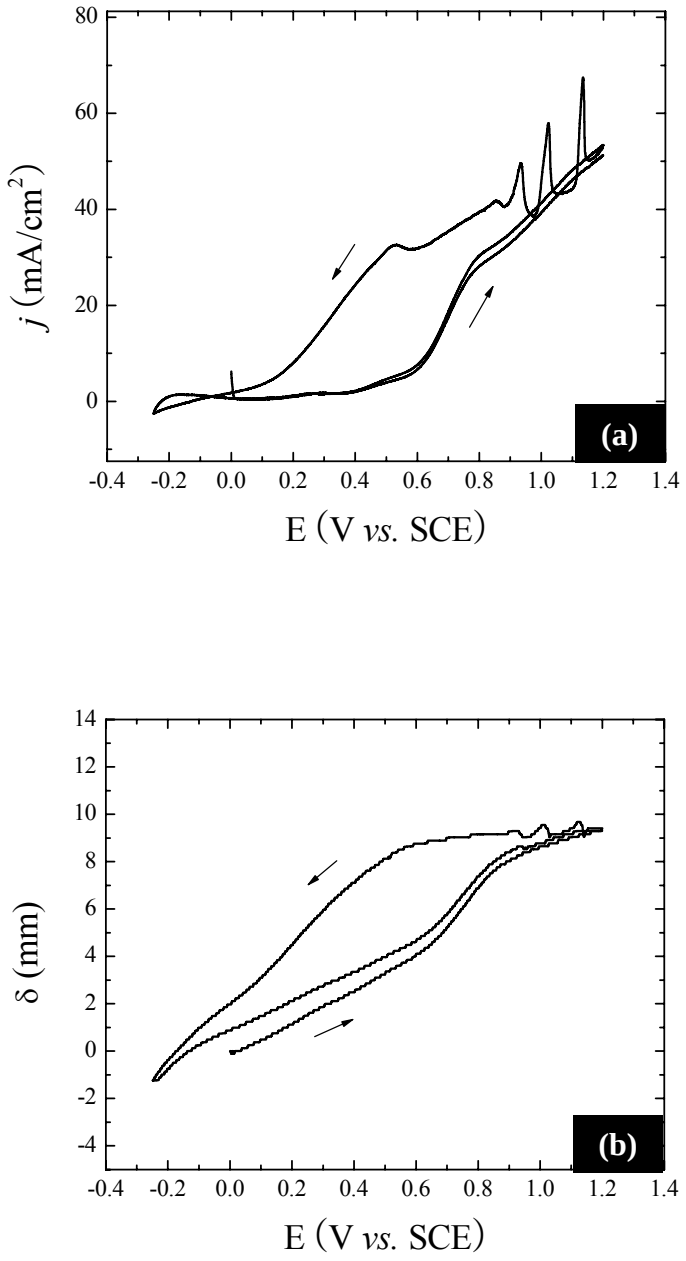

Figure 6.7. Cyclic voltammograms (a) and corresponding deflection (b) in 1 M HCHO + 3 M H_2SO_4 solution (scan rate of 20 mV/s).

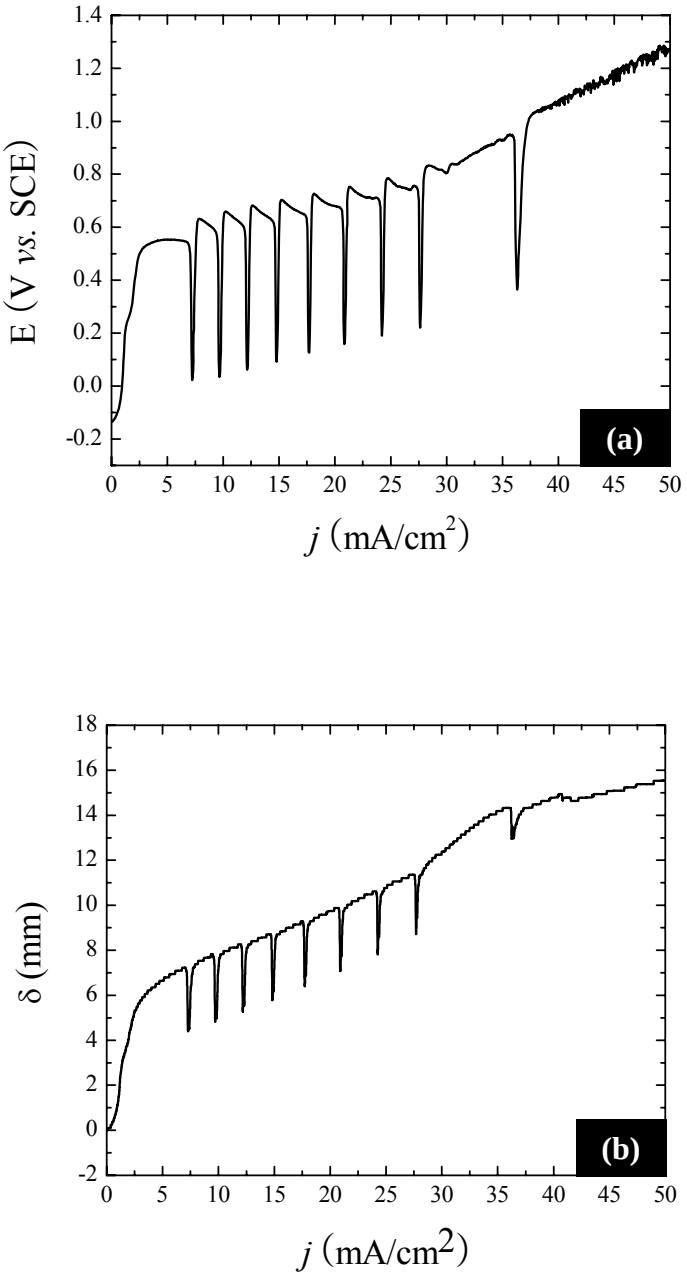

Figure 6.8. Galvanostatic linear sweep voltammogram of a platinum-IPMC in 1 M HCHO + 3 M H_2SO_4 (scan rate of 1 mA/s).

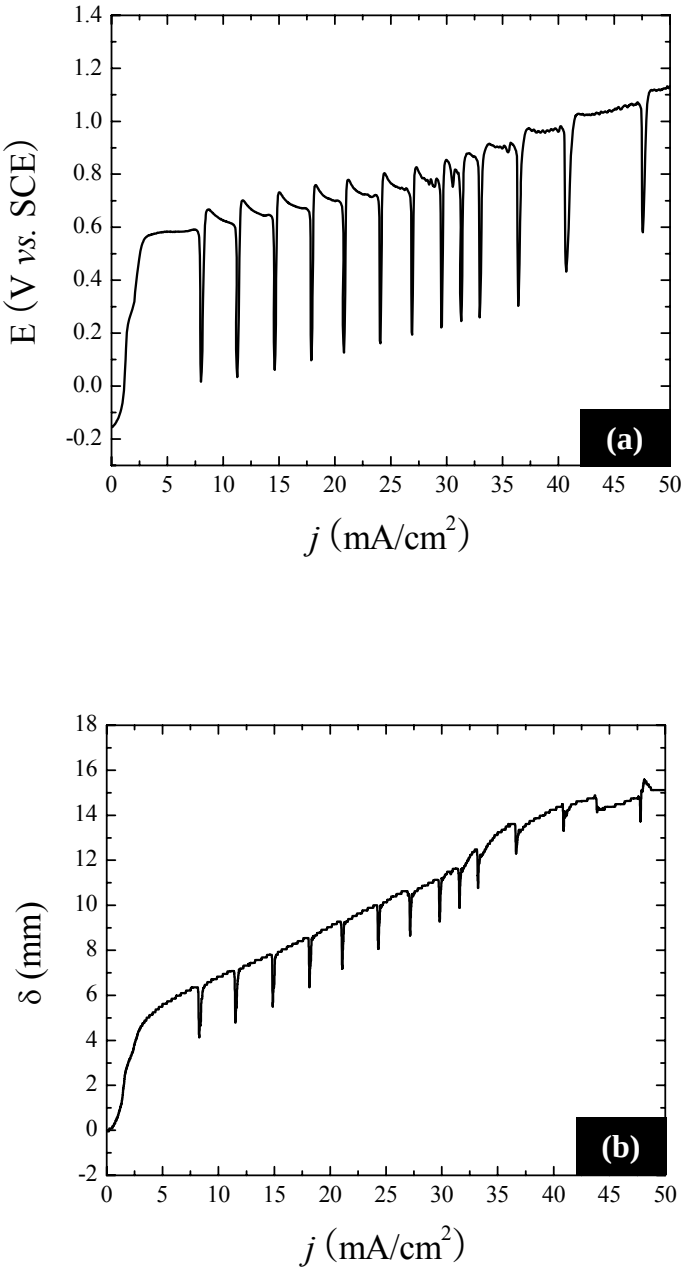

Figure 6.9. Galvanostatic linear sweep voltammogram of a platinum-IPMC in 2 M HCHO + 3 M H_2SO_4 (scan rate of 1 mA/s).

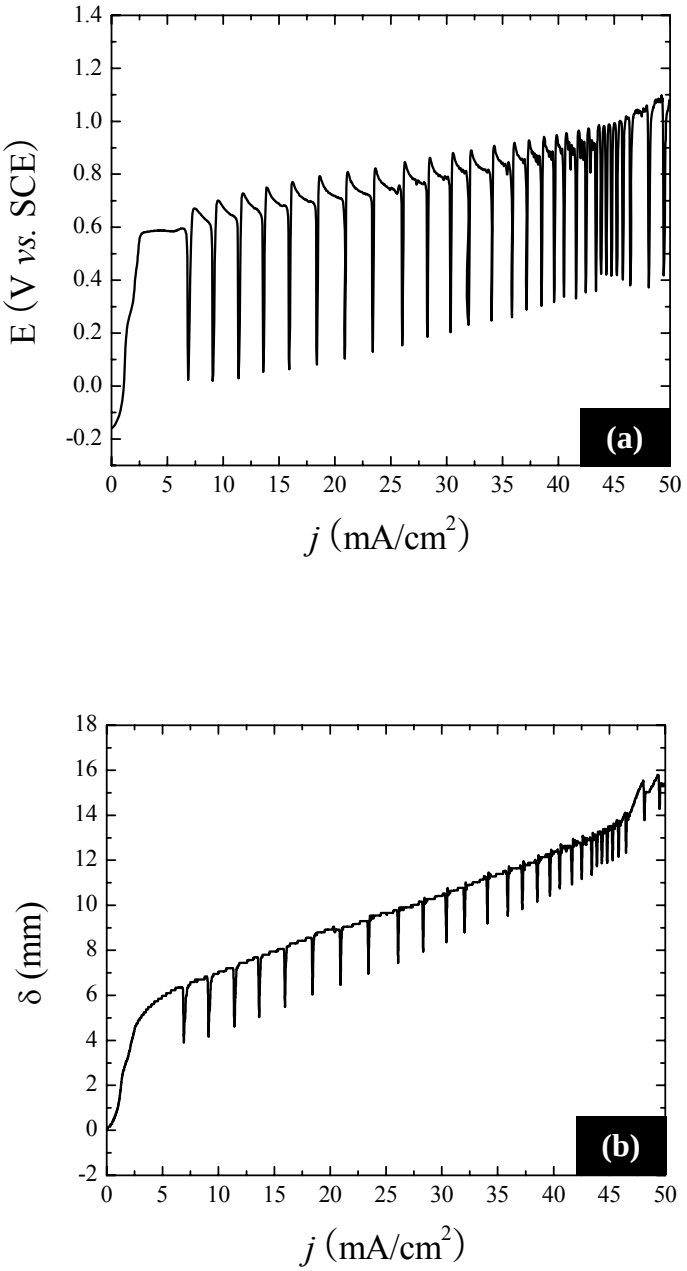

Figure 6.10. Galvanostatic linear sweep voltammogram of a platinum-IPMC in 3 M HCHO + 3 M H_2SO_4 (scan rate of 1 mA/s).

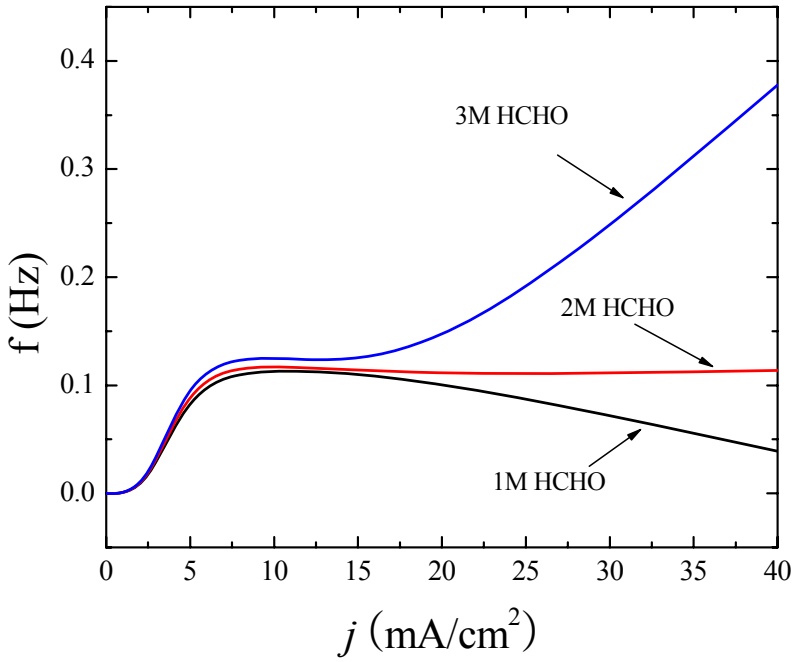

Figure 6.11. Current dependence of oscillation frequency of the platinum-IPMC with three different concentrations of HCHO (scan rate of 1 mA/s).

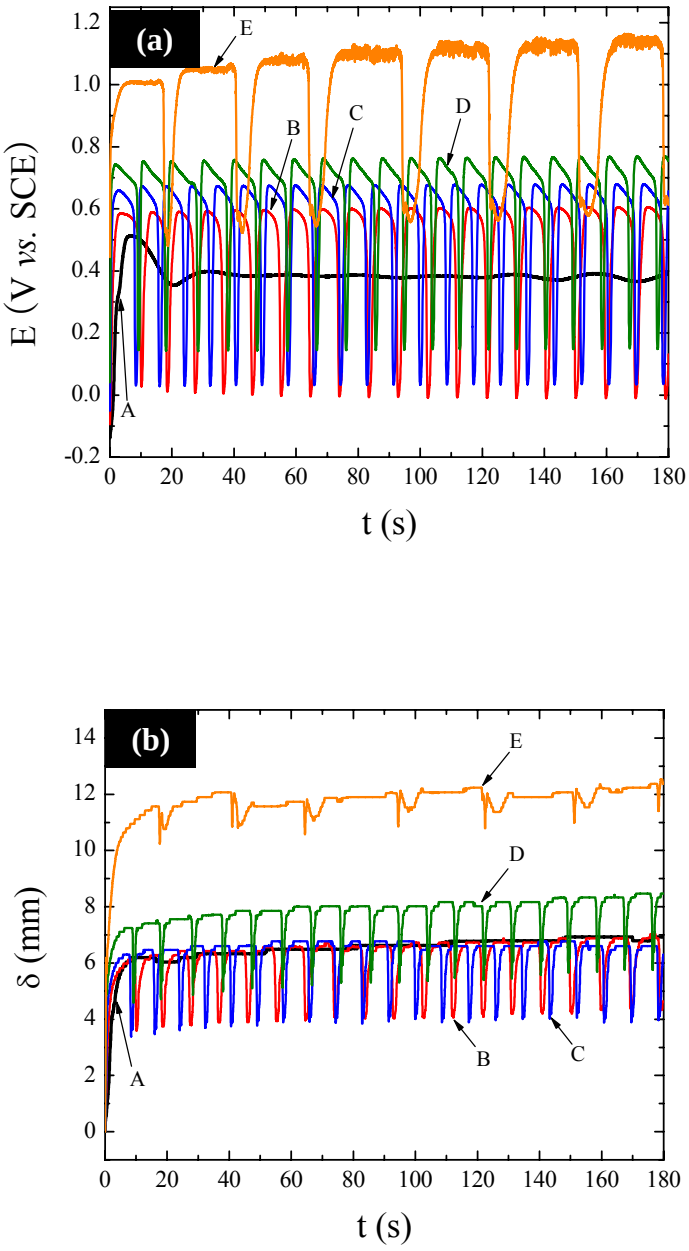

Figure 6.12. Chronopotentiogram (a) and corresponding deflection data (b) of a platinum-IPMC in 1 M HCHO + 3 M H_2SO_4 under constant current of 2.5 (A), 5 (B), 10 (C), 20 (D), and 40(E) mA/cm^2 (scan rate of 1 mA/s).

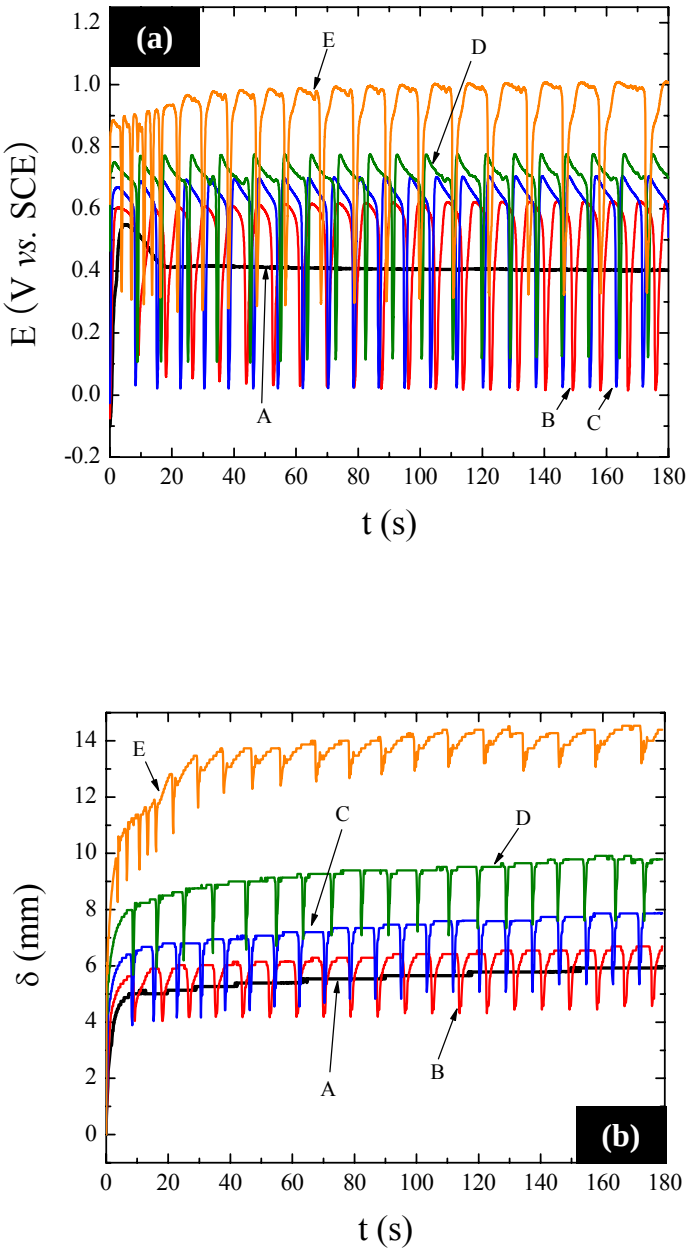

Figure 6.13. Chronopotentiogram (a) and corresponding deflection data (b) of a platinum-IPMC in 2 M HCHO + 3 M H_2SO_4 under constant current of 2.5 (A), 5 (B), 10 (C), 20 (D), and 40(E) mA/cm^2 (scan rate of 1 mA/s).

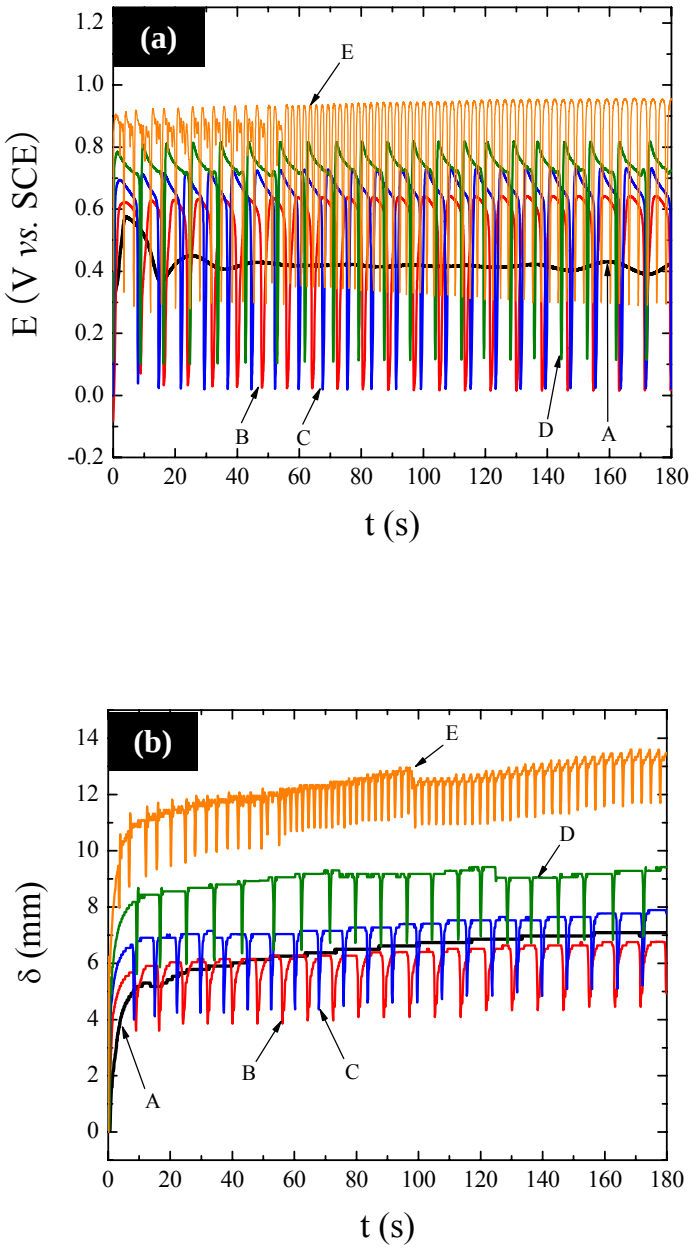

Figure 6.14. Chronopotentiogram (a) and corresponding deflection data (b) of a platinum-IPMC in 3 M HCHO + 3 M H_2SO_4 under constant current of 2.5 (A), 5 (B), 10 (C), 20 (D), and 40(E) mA/cm^2 (scan rate of 1 mA/s).

Table 6.1. Maximum potential difference and maximum deflection difference of the oscillations with three different concentrations of HCHO.

j (mA/cm^2) / c of HCHO	ΔE_{max} (V *vs.* SCE)					$\Delta \delta_{max}$ (mm)				
	2.5	5	10	20	40	2.5	5	10	20	40
1 M	0	0.60	0.63	0.61	0.54	0	2.54	2.86	2.62	1.48
2 M	0	0.61	0.67	0.66	0.68	0	2.10	2.52	2.18	1.33
3 M	0	0.62	0.71	0.71	0.67	0	2.30	2.56	2.35	1.64

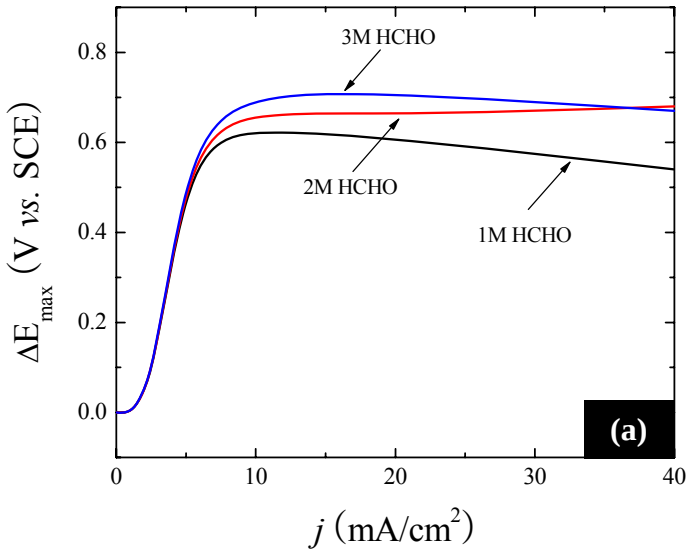

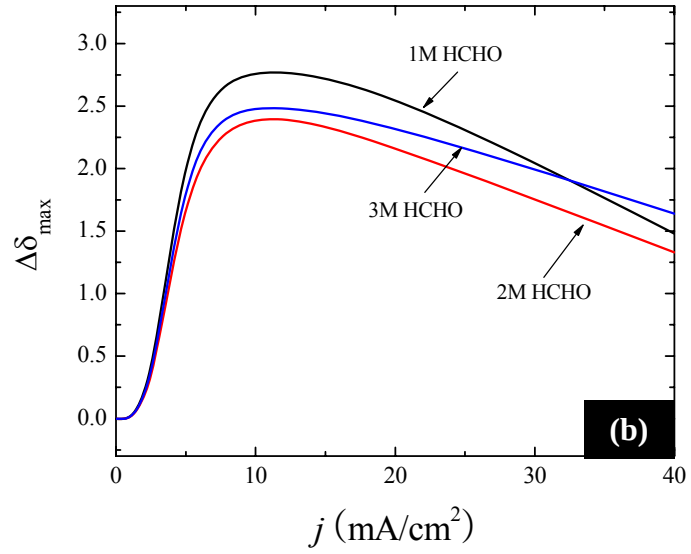

Figure 6.15. Maximum potential difference (a) and maximum deflection difference (b) of the oscillations with three different concentrations of HCHO

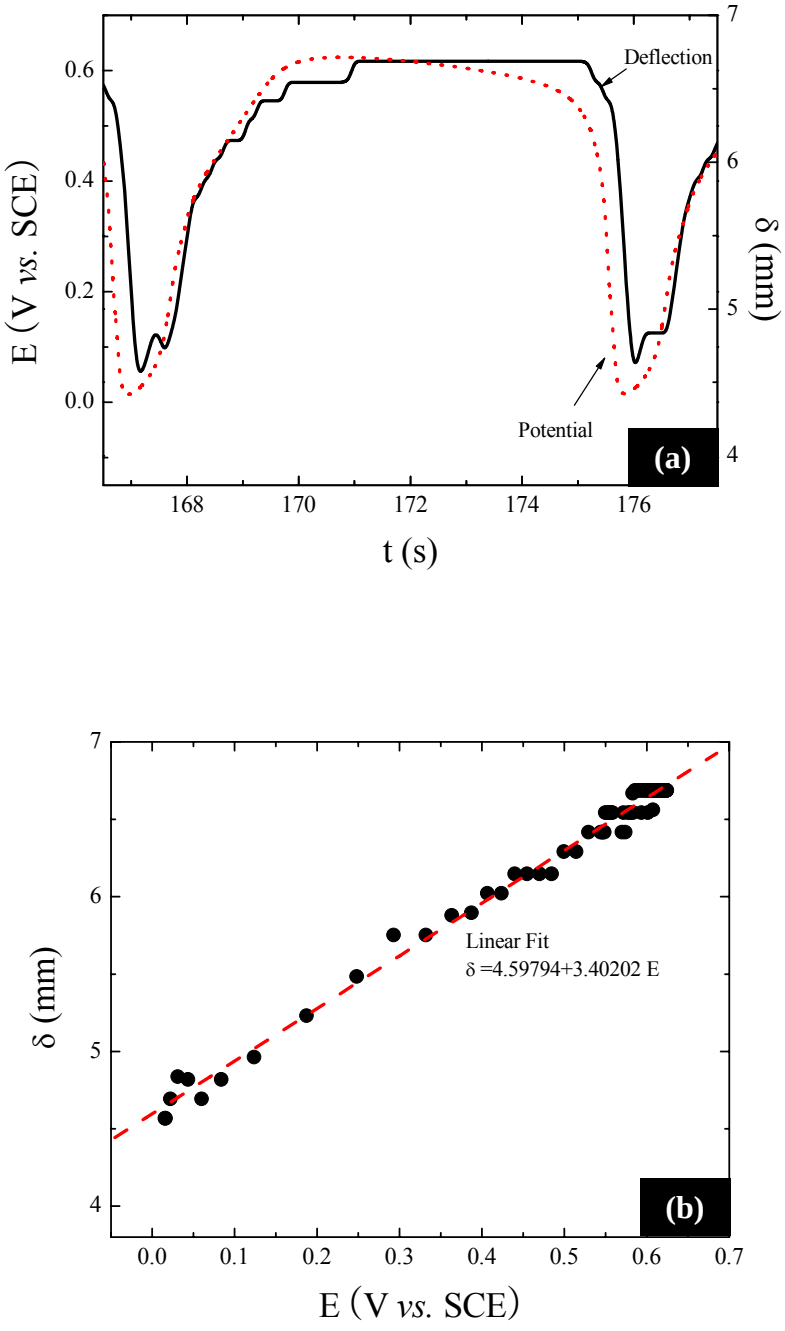

Figure 6.16. One oscillation peak (a) and a relationship between corresponding potential and deflection of the peak for 2 M HCHO under constant current of 5 mA/cm^2.

6.4. Effect of type of small organic molecules

As mentioned in previous sections, electrochemical oscillations during electrooxidation of small organic molecules (SOMs) under specific conditions are usually observed. Obviously, the oscillations obtained from an HCHO system can be useful for a self-oscillatory IPMC. The system requires diversity and performance improvement for proper application.

It is well-documented that HCOOH shows electrochemical oscillation phenomena during oxidation [125, 136, 138]. However, a feasibility test of HCOOH is required for self-oscillatory IPMC. The CV of HCOOH was conducted. In addition, alcohols, such as CH_3OH, C_2H_5OH, and C_3H_7OH, were tested. Figure 6.17 shows cyclic voltammograms of a platinized platinum electrode in three different alcohol solutions. The impact of type of alcohols on the activity of the platinized platinum electrode can be seen in Figure 6.17. The activity increased as expected with a decreasing molecular weight. Three current peaks appear in the cyclic voltammograms in these alcohols but an oscillation peak is not observed in the ranges of 0 V to +1.4 V (*vs.* SCE). It is determined that adsorbed CO coming from these organic molecules converts into CO_2 without oscillation phenomena. Figure 6.18 shows the cyclic voltammograms of a platinum-IPMC with three different concentrations of HCOOH. The oscillation peaks increase with an increasing concentration of HCOOH, but the number of peaks is the same. For further investigation, galvanostatic linear sweep voltammetry was performed. Figure 6.19 shows galvanostatic linear sweep voltammograms. Oscillation peaks are shown in a narrower range of applied current and the number of oscillations is also smaller than in the HCHO system.

Seemingly, the HCOOH system is not proper for a self-oscillatory IPMC with high frequency.

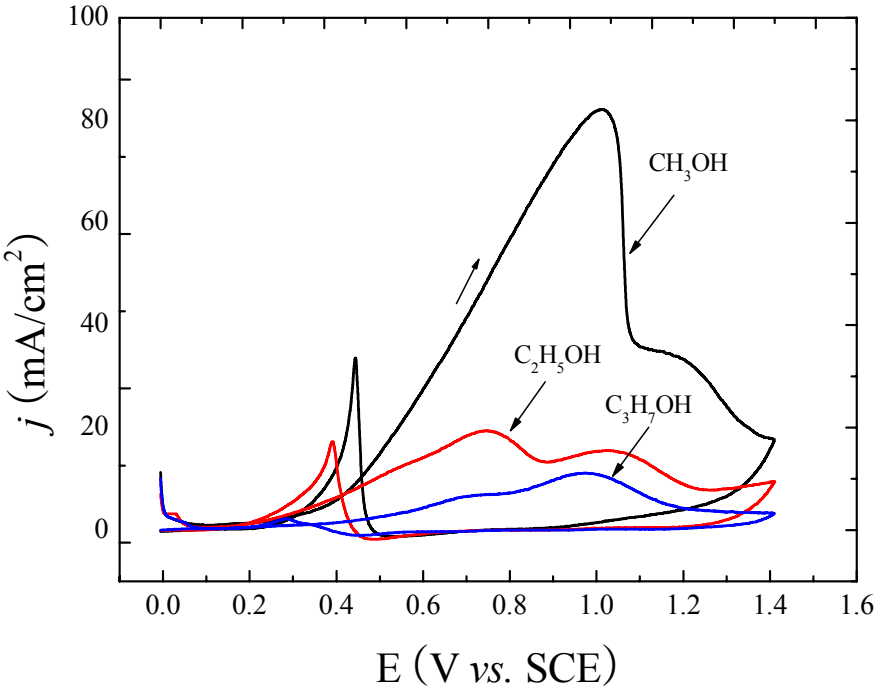

Figure 6.17. Cyclic voltammograms of platinized platinum electrode in various alcohol solutions (scan rate of 20 mV/s).

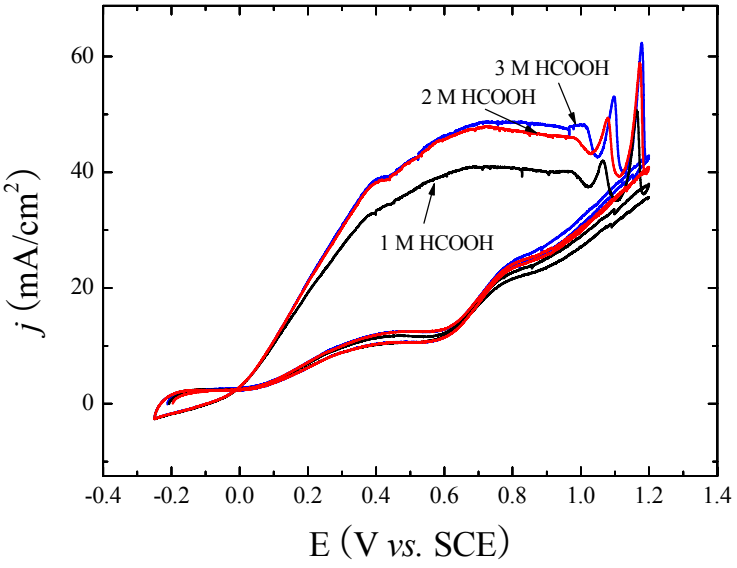

Figure 6.18. Cyclic voltammograms of the platinum-IPMC with three different concentrations of HCOOH (scan rate of 20 mV/s).

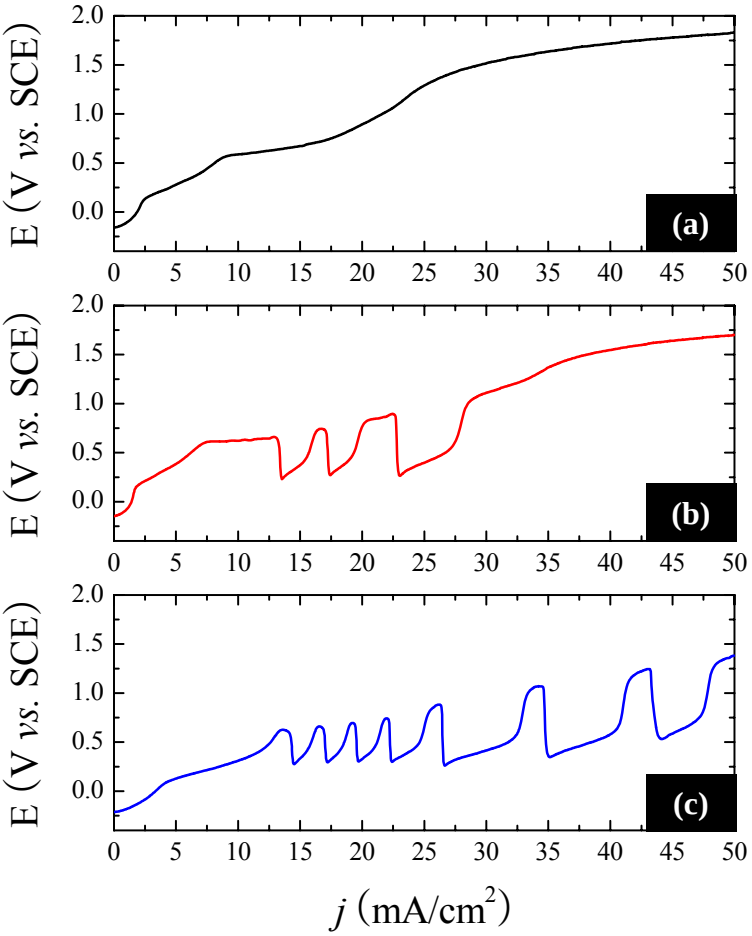

Figure 6.19. Galvanostatic linear sweep voltammograms of the platinum-IPMC in 1 M (a), 2 M (b), and 3 M (c) HCOOH + 3 M H_2SO_4 (scan rate of 1 mA/s).

CHAPTER 7:

MODELING OF IPMC ACTUATOR

This chapter will be discussing how an analytical model for an IPMC actuator, which can exhibit varying deflection along the actuator, is developed as an effective design tool. The model factors in an equivalent circuit model, beam theory, and surface chemistry. The developed model was validated by comparing the resulting data to that from the experiments. The practical free deflection of the IPMC is often the result of several physical factors interacting simultaneously. This chapter focuses on the development of an analytical model to predict the free deflection of an IPMC.

The modeling of the IPMC actuator is a multiphysics task since it involves electricity, chemistry, dynamics, and control. The coupling obtained in such a model is often highly non-linear. Due to its complexity and its nonlinear behavior, the IPMC's predictability and modeling is very difficult and its overall behavior is still not fully agreed upon by researchers. Consequently, there have been many models, based on numerous parameters involved with IPMCs, which have been proposed for the behavior of the material. The model studied in this chapter is separated by the two categories: 1) electrochemical model and 2) electromechanical model. It can be expected that the resulting model enables the incorporation of these characteristics into a system design. The understanding of the motion and relevant mechanism is the basis for controlling the actuator. After deriving a mathematical model that accounts for electrical, chemical,

electrochemical, mechanical properties, and geometric parameters of the IPMC, it was compared against the experimental data for its verification.

7.1. An equivalent circuit model of IPMC

The EIS was used to predict an electrochemical circuit model of IPMC as mentioned in Chapter 4. As shown in Figure 4.20, the IPMC in the double layer potential region was represented by an RLC equivalent circuit model. To simplify the mathematical equations, the inductance assumed negligible. Then, IPMCs are both inherently resistive and capacitive, allowing for the material to be modeled using an equivalent RC circuit (see Figure 4.18) which will describe the charging/discharging behavior of the IPMCs. The proposed model includes two resistors and two capacitors, which primarily account for the effective electrodes on the surface of the IPMC. A resistor was placed between the two RC circuits to account for the material between the electrodes. The resistance was mainly due to ion migration through the polymer matrix. The capacitances, C_1 and C_2, were set equal to each other by assuming that the IPMC electrode surfaces were prepared identically throughout the manufacturing process. The values of R_1 and R_2 were also set equal to each other for the same reason and will remain as constants, along with the value for the resistor across the middle, R_e, throughout the testing. Current flowing in capacitors and resistors depends on rate of voltage change across the capacitor and resistor. Equation 7.1 can be obtained using the differential equation describing a parallel RC circuit with a step function input (see Appendix E) [143]. The charge in Equation 7.2 can be obtained by the integration of Equation 7.1.

$$i(t) = V\left[\frac{R_e + 2R_1}{R_e(2R_1 + R_e)} e^{-\left(\frac{2R_1+R_e}{R_1C_1R_e}\right)t}\right] \tag{7.1}$$

$$Q(t) = V\frac{R_1C_1}{2R_1 + R_e}\left[1 - e^{-\left(\frac{2R_1+R_e}{R_1C_1R_e}\right)t}\right] \tag{7.2}$$

As can be observed in Chapter 4, the IPMC often exhibits a slow relaxation toward the cathode side after a quick bending toward the anode side at the initial stage. The second assumption of this model is that this relaxation phenomena associated with the bending curvature of the IPMC does not occur during actuation.

7.2. Electromechanical model of IPMC

Since the thickness of IPMC in cantilever configuration is much less than its length, the elastica theory adequately describes the large and non-linear deflections. The deformations are due mainly to internal bending moments (M). An expression for the internal bending moment of the IPMC actuator can be derived by integrating the uniform stress (σ) acting over the cross-sectional area of the platinum layers in relation to the distance from the neutral axis *y*, and the actuator width (*w)*. Note that the tensile stress is directly related to the distance above the neutral axis. The compressive stress is also directly related to the distance below the neutral axis. There are several assumptions; a) the IPMC actuator is linearly elastic, b) the neutral axis for bending of the IPMC is inextensible, c) the effects of Poisson's ratio and transverse shear deformations are

negligible, and d) Young's modulus of the IPMC is the same for compression and tension and the relationship is the same. [144, 145].

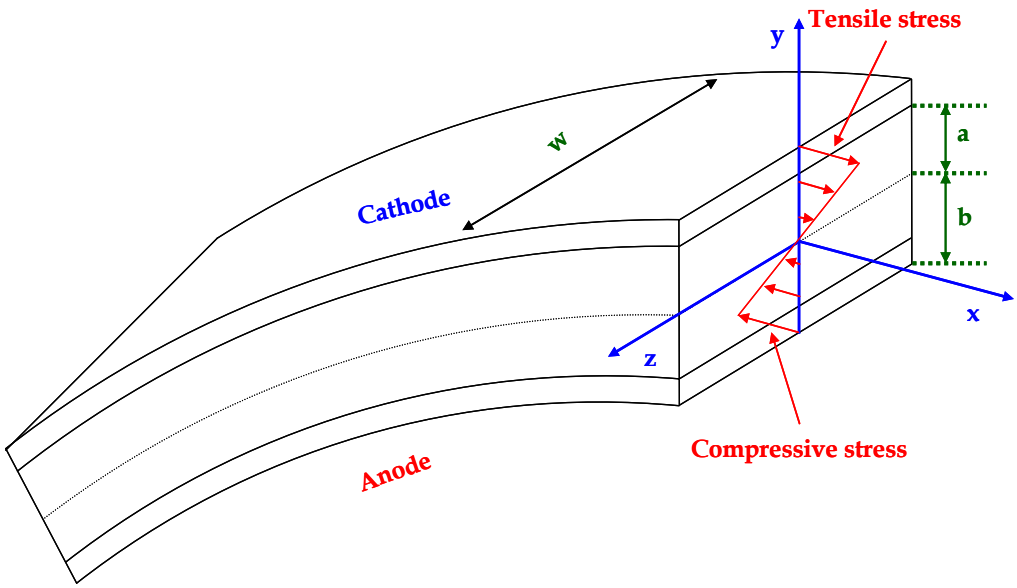

Figure 7.1. Schematic diagram of stress distribution in the IPMC during bending.

According to the experimental results shown in Figure 7.2, the forces generated from the IPMC are affected by the corresponding current on the electrode surface, showing a linear relationship. It could be assumed that the applied charge is proportional to the corresponding current. Therefore, assuming that the relationship between the applied charge and the uniform stress of the IPMC is pseudo-linear, because the deformation of the IPMC originated from generated stress, the stress can be defined as

$$\sigma \cong c_{\text{mod}} \cdot Q \tag{7.3}$$

where c_{mod} is an experimentally obtained modeling parameter.

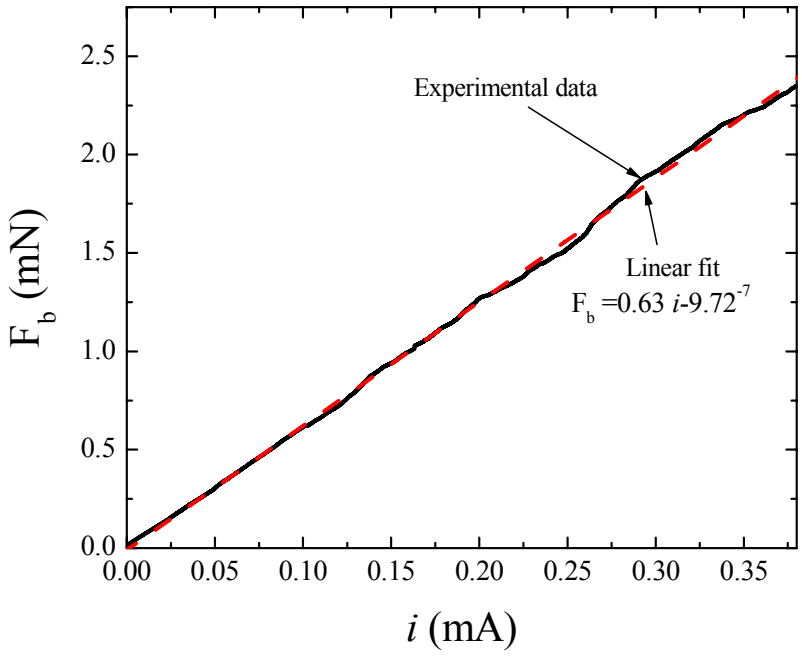

Figure 7.2. Linear relationship between the current and the force during actuation. *Note that this graph was obtained from Figure 5.13.

Substituting Equations 7.2 and 7.3, the bending moment can be expressed as the following linear model that relates the input charge and bending moment.

$$M = \left(w\sigma \int_a^b y dy \right) - \left(w\sigma \int_{-b}^{-a} y dy \right) = \frac{wQ}{c_{\text{mod}}} \left(b^2 - a^2 \right) \tag{7.4}$$

where σ, w, b, and a denote the uniform stress, the width, the half thickness of the IPMC, and the half thickness of the membrane material, respectively. $\overline{YI}$, the weighted flexural rigidity, is given by [144]

$$\overline{YI} = \left\{ Y_b \frac{2w(b^3 - a^3)}{3} + Y_a \frac{2wa^3}{3} \right\} \tag{7.5}$$

The classical Bernoulli-Euler beam theory can be expressed by the non-linear differential equation [144]. The radius of the curvature is related to the derivatives of the deflection and can be written as:

$$\frac{1}{r} = \frac{M}{\overline{YI}} = \frac{\dfrac{d^2 v}{dx^2}}{\left[1 + \left(\dfrac{dv}{dx} \right)^2 \right]^{3/2}} = \frac{\dfrac{wR_1 C_1 V \left(b^2 - a^2 \right)}{c_{\text{mod}} (2R_1 + R_e)}}{\left\{ Y_b \dfrac{2w(b^3 - a^3)}{3} + Y_a \dfrac{2wa^3}{3} \right\}} \cdot \left[1 - e^{-\left(\frac{2R_1 + R_e}{R_1 C_1 R_e} \right) t} \right] \tag{7.6}$$

where *r* is the radius of curvature and dx and dv are the differential distances in the horizontal and vertical axis, respectively.

The resulting differential equation could be solved using the Matlab-ode23 toolbox to get the theoretical bending curve of the sample IPMC actuator, as a function of the distance from the surface. A computer simulation was performed for Equation 7.6 to study the IPMC bending under the applied voltages from +1 to +4 V. Table 7.1 shows the simulation and material parameters used in this computational study. Note that the viscoelastic property of the IPMC is ignored and the model does not incorporate the relaxation behavior of IPMC. Accordingly, for Nafion™ 117, Young's modulus of 200 MPa was used [146] in this simulation. Figure 7.3 shows a large defelection simulation of the IPMC for the step input voltages from +1 to +4 V. The simulation results closely follow the experimental results of platinum-IPMC solvated with [bmim][PF_6].

Table 7.1. Parameters used in the simulations of the IPMC model.

Parameters	Units	Description	Value
l	m	length of IPMC	40.5E-3 m
w	m	width of IPMC	5E-3 m
h_N	m	thickness of Nafion™	200E-6 m
h_{Pt}	m	thickness of Pt	10E-1 m
Y_N	Pa	modulus for Nafion™	50E6 Pa
Y_{Pt}	Pa	modulus for electrode	169E9 Pa
R_1 and R_2,	Ω	resistance of electrode	10
R_e	Ω	resistance of electrolyte	50
C_1 and C_2	F	double layer capacitance	0.02
τ_1	s	time constant, $R_1R_eC/(R_e+2R_1)$	0.143
τ_2	s	time constant	10
ρ_{Pt}	kg/m^3	density of Pt	21,500
ρ_N	kg/m^3	density of Nafion™	2,600

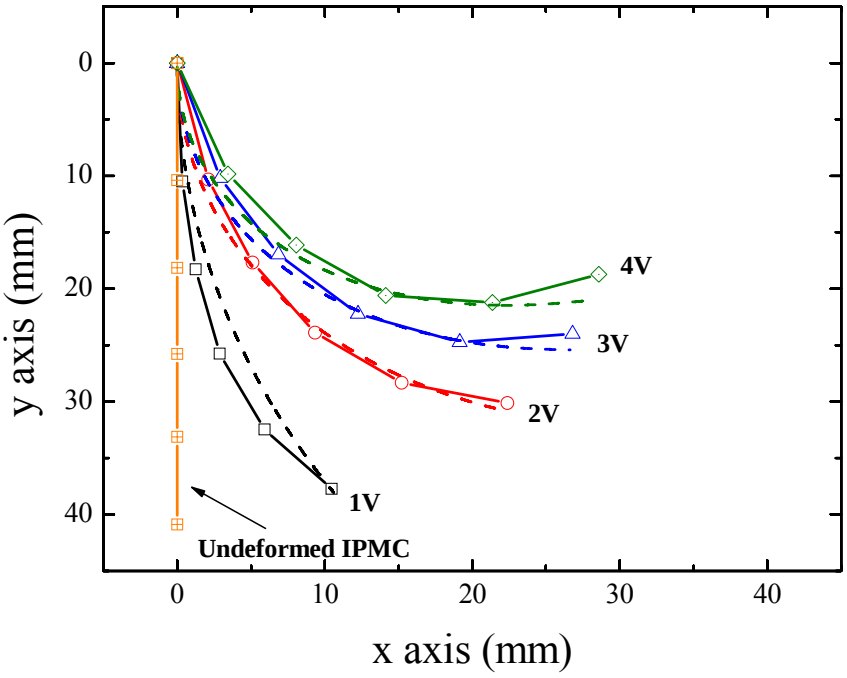

Figure 7.3. Maximum deflection under various applied voltages (1~4 V). Experimental results (-symbol-) and simulation results (dashed line).

7.3. Non-linear dynamic model for self-oscillatory IPMC

By describing the electrochemical oscillation of formaldehyde on platinum-IPMC, three important variables are included: coverage of intermediates (CO and OH), electrode potential (E), and electrochemical kinetic rate (k_i) [137]. In this study, a model was developed for adequately describing the self-oscillatory motion that exhibits non-linear dynamics. It can be assumed that the current is mostly carried by reactive intermediates (CO) and, CO and OH are responsible for blocking the platinum surface sites at lower potentials while they react with each other at higher potentials. Due to this reaction, the total applied current is the sum of the currents resulting from electrochemical reaction and the charging into an electric double layer. The coupled ordinary differential equations in the first approximation can be expressed as [136]:

$$\dot{\theta}_{CO} = k_2(1-\theta_{CO}-\theta_{OH}) - k_4\theta_{CO}\cdot\theta_{OH} \tag{7.7}$$

$$\dot{\theta}_{OH} = k_3\theta_{CO}(1-\theta_{CO}-\theta_{OH}) - k_{-3}\theta_{OH} - k_4\theta_{CO}\cdot\theta_{OH} \tag{7.8}$$

$$\dot{E} = \frac{1}{C_1}\left[i - 2FS_{Pt}\{k_1(1-\theta_{CO}-\theta_{OH}) + k_4\theta_{CO}\cdot\theta_{OH}\}\right] \tag{7.9}$$

$$k_i(E) = \exp[s_i(E-E_i)] \tag{7.10}$$

where θ_{CO} and θ_{OH} are the adsorption coverage of CO and OH, F is the Faraday constant, s_i is a modeling coefficient, and S_{Pt} is the number of sites on a unit surface area of platinum (1.67×10^{-19} mol/cm^2 [141]). Subscripts, one to four, are denoted in Equations 7.7 to 7.10.

With the experimentally adjusted parameters, including $k_{i=1..4}$ and $E_{i=1..4}$, and data presented in Figure 6.13, the simulation was conducted under an applied current of 10 mA/cm^2. The experimental results are given in Figure 6.9 where the simulation results are also compared to the experimental data. In general, the simulation results of shape, oscillation amplitude, and oscillation period show agreement with the experimental data. The solution of Equation 7.9, which simulates bending curves of the IPMC in initial, maximum, and minimum positions, is shown in Figure 7.5. Applied potentials were obtained from the simulated data of Figure 7.4. The deflection of this particular oscillation follows between the curves of (b) and (c) in Figure 7.5. The calculated results indicate that the maximum deflection between states (b) and (c) is approximately 2.2 mm. In this case, the model slightly underpredicts the oscillatory deformation. The general behavior of self-oscillatory IPMC is highly repeatable and shows regular periodic phenomena in both experimental and simulated results.

Table 7.2. Parameters used in simulations of self-oscillatory IPMC model.

Parameters	Units	Description	Value
a_1	V^{-1}	Modeling coefficient of reaction (7.7)	10
a_2	V^{-1}	Modeling coefficient of reaction (7.8)	-10
a_3	V^{-1}	Modeling coefficient of reaction (7.9)	+9
a_{rev3}	V^{-1}	Modeling coefficient of reverse reaction (7.9)	-9
a_4	V^{-1}	Modeling coefficient of reaction (7.10)	+20
j	mA/cm^2	current density	+10
F	C/mol	Faraday constant	96,485
E_1	V	Potential of reaction (7.7)	+0.165
E_2	V	Potential of reaction (7.8)	+0.3
E_3	V	Potential of reaction (7.9)	+0.01
E_{rev3}	V	Potential of reverse reaction (7.9)	+0.55
E_4	V	Potential of reaction (7.10)	+0.75
S_{Pt}	mol/cm^2	The number of sites of Pt surface	1.67×10^{-19}

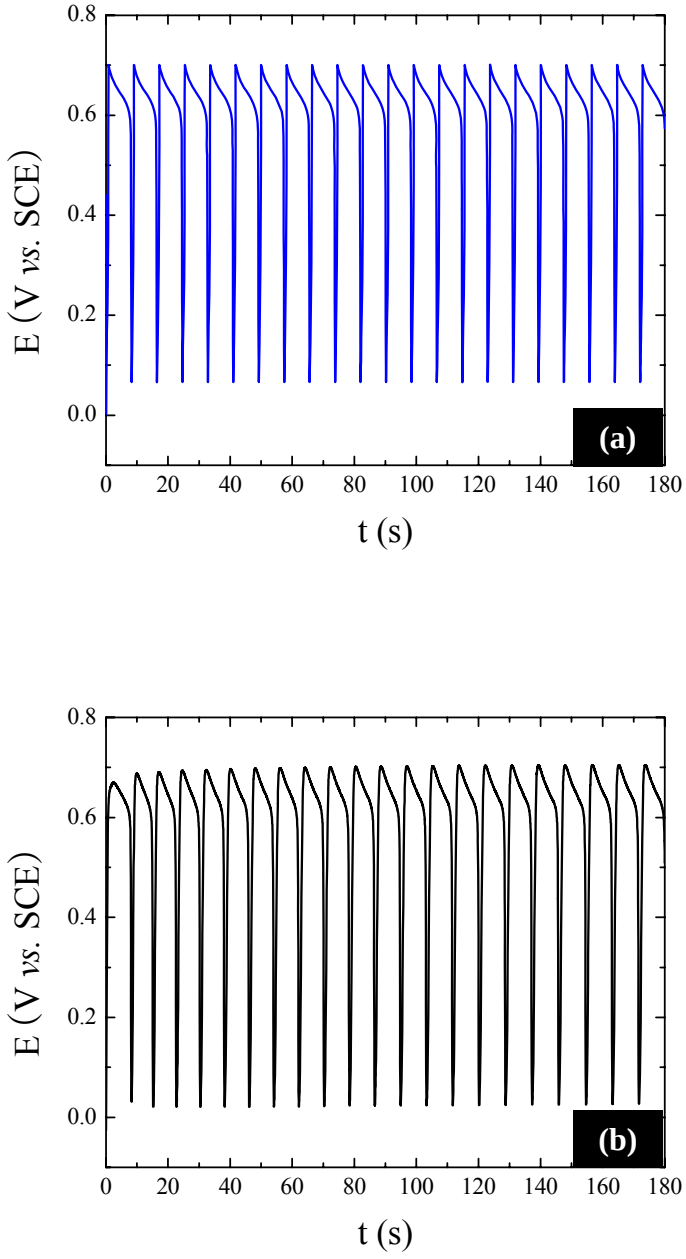

Figure 7.4. Simulated (a) and observed oscillation patterns (b) of the platinum-IPMC in 2 M HCHO + 3 M H_2SO_4 under applied current of 10 mA/cm^2.

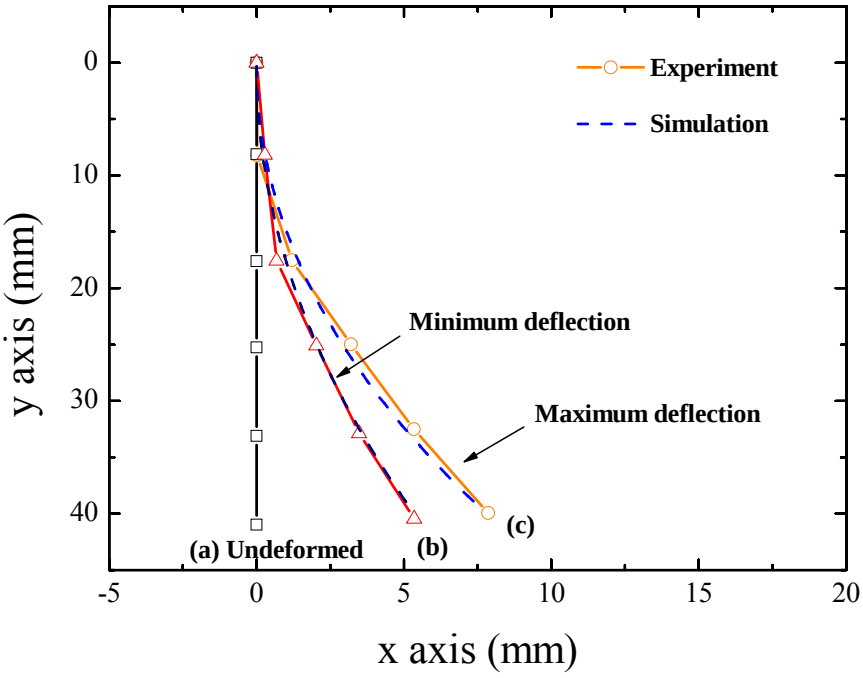

Figure 7.5. Simulated bending curve with oscillation patterns an IPMC in 2 M HCHO + 3 M H_2SO_4 under an applied current of 10 mA/cm^2. Experimental results (-symbol-) and simulation results (dashed line).

CHAPTER 8:

CONCLUSIONS AND RECOMMENDATIONS

8.1. Conclusions

Ionic Polymer-Metal Composites (IPMCs) are soft electroactive polymers based upon ion-exchange membranes. IPMC actuators are capable of operating in both water and air environments. This work explored the electrochemical and electromechanical characteristics of IPMCs. Practical approaches were established to obtain more accurate data and improved actuation performance. As a result of the tension test, the hydrated samples showed decreased break strain values due to the water molecules, which molecules lead to lower break stress. In particular, nano-sized gold particles contributed to a significant increase in the Young's modulus and the tensile strength of the dried gold-IPMC. From the DSC results, the first Tg was assigned to the polymeric matrix of Nafion™ and, the second Tg was associated with the region of crystalline melting of the Nafion™. The significant increase on the Tg of platinum-IPMC and gold-IPMC was caused by the platinum and gold metal.

In this study, the origin of the relaxation phenomena of IPMC's was investigated. The experimental results clearly showed that the relaxation phenomena were caused by the overpotential of the electrode surface. Overpotential values of approximately +1 V were measured for the platinum-IPMC. With applied potentials over +1 V, the IPMCs started showing relaxation phenomena. These findings can be explained by the catalytic

activities of the platinum surface. In the room temperature ionic liquid (RTIL) system, the IPMC deflections continuously increased, without relaxation for in-air operation. The RTIL system showed not only a larger and more stable bending motion but also seemingly eliminated the relaxation phenomena. In addition, the efficiency of IPMCs in an RTIL system was significantly improved because the input power was mostly used in actuation; on the other hand, the efficiency of hydrated IPMCs was significantly low because they consumed input power in electrochemical reactions during actuation.

An intriguing new feature of the IPMC, "spontaneous rhythmic motion," was introduced. A surface modification technique that provokes a self-oscillatory motion of IPMCs was investigated. When a constant electric field was imposed on a platinum-IPMC in the presence of HCHO, the IPMC exhibited periodic deformation due to the electrochemical oscillation. Maximum deflection of the self-oscillatory IPMC was obtained under the applied current of 10 mA/cm^2. The self-oscillatory IPMC system, under specific conditions, could be a useful means to minimize the use of complex electronics in many small-scale applications.

Finally, an analytical model was developed to predict the free deflection of a self-oscillatory IPMC. The model in this study was verified with experimental data. It has been demonstrated that the bending curve model was valid for various applied potentials. The general behavior of self-oscillatory IPMC was highly repeatable and showed regular periodic phenomena in both experimental and simulated results.

Furthermore, the contributions of this research include progress in understanding the actuation mechanism of IPMCs. The results can be used as a basis for controlling the actuator, and the proposed systems, such as an RTIL and self-oscillatory IPMCs, will

have an impact far beyond the realm of the current limitations for application. In addition, the model developed can be expected to enable the incorporation of physical characteristics into a system design.

8.2. Recommendations for future study

Future studies include further characterization of the material including possible applications. To date, platinum and gold have been recognized as the most suitable electrode materials for an IPMC. However, platinum and gold themselves are known to be rapidly poisoned on the surface by strongly adsorbed species that are coming from the dissociation of water. There is a general need to improve the catalytic activity for the aqueous environments. However, candidate metals with sufficient stability in aqueous medium are rather limited. Making an alloy, which give allowable tolerance for electrochemical reactions, can be an effective way to reduce the effect of poisoning. Moreover, the cost reduction problem and the efficiency of IPMC materials are concerns for commercialization. One possible way is to decrease the precious metal content of the electrodes. Progress in efficiency can be mainly accomplished by utilization of either a more stable electrode material or a more durable membrane material, which can be achieved by increasing the physical strength of the membrane. The membranes have been fabricated from numerous polymers, such as polystyrene, polymethacrylate, and tetrafluoroethylene. Ionic fixed charge groups are added to the polymer backbone by a variety of means, including chemical treatments and radiation grafting. Proper membranes must be developed in order to generate the required force for practical applications of IPMCs.

The softness and flexibility of IPMCs are definite advantages that can be utilized in biomedical applications. For these applications, the components of the specific IPMC must be biocompatible. In general, biocompatible materials must be capable of being used in or on the human body without eliciting a rejection response from the surrounding body tissues. For this, a protective coating of the IPMC may be required to prevent the rejection and dehydration of the electrolyte.

The modeling of the IPMC actuator is a multi-physics task since it involves electrical, chemical, and mechanical properties. A back-diffusion parameter is also being incorporated into the model to account for the relaxation phenomena. Once completed, the model will be capable of modeling the performance of whole IPMC systems. The multiphysics model can be used to predict actuation of those IPMCs and possibly contribute to the significant reduction in the cost of experiments.

REFERENCES

[1] Y. Bar-Cohen, S. Leary, A. Yavrouian, K. Oguro, S. Tadokoro, J. Harrison, J. Smith, and J. Su, "Challenges to the application of IPMC as actuators of planetary mechanisms," presented at Smart Structures and Materials, Newport, CA, 2000.

[2] Y. Bar-Cohen and S. Leary, "Electroactive Polymers (EAP) Characterization Methods," presented at Electroactive Polymer Actuators and Devices, Smart Structures and Materials, 2000.

[3] K. Oguro, Y. Kawami, and H. Takenaka, "Bending of an ion-conducting polymer film-electrode composite by an electric stimulus at low voltage," *Journal of Micromachine Society*, vol. 5, pp. 27-30, 1992.

[4] K. Sadeghipour, R. Salomon, and S. Neogi, "Development of a Novel Electrochemically Active Membrane and Smart Material Based Vibration Sensor/Damper," *Smart Materials and Structures*, vol. 1, pp. 172-179, 1992.

[5] S. Guo, T. Fukuda, K. Kosuge, F. Arai, K. Oguro, and M. Negoro, "Micro Catheter System with Active Guide Wire," presented at IEEE ICRA, 1995.

[6] S. Guo, T. Nakamura, and T. Fukuda, "Design and Characteristic Evaluation of Micropump Using ICPF Actuator," presented at 7th International Symposium on Micro Machine and Human Science, 1996.

[7] K. Asaka, K. Oguro, Y. Nishimura, M. Mizuhata, and H. Takenaka, "Bending of polyelectrolyte membrane-platinum pomposites by electric etimuli Part I. Response characteristics to various waveforms," *Polymer*, vol. 27, pp. 436-440, 1995.

[8] M. Sharhinpoor, Y. Bar-Cohen, J. O. Simpson, and J. Simth, "Ionic Polymer-Metal Composites (IPMCs) as Biomimetic Sensors, Actuators, and Artificial Muscles- a Review," *Smart Materials and Structures*, vol. 7, pp. R15-30, 1998.

[9] Y. Abe, A. Mochizuki, T. Kawashima, S. Yamashita, K. Asaka, and K. Oguro, "Effect on bending behaviour of bounter bation bpecies in berfluorinated bulfonate bembrane-blatinum bomposite," *Polymers for Advanced Technologies*, vol. 9, pp. 520-526, 1998.

[10] K. Asaka, N. Fujiwara, K. Oguro, K. Onishi, and S. Sewa, "State of water and ionic conductivity of solid polymer electrolyte membranes in relation to polymer actuators," *Journal of Electroanalytical Chemistry*, vol. 505, pp. 24-32, 2001.

[11] K. Onishi, S. Sewa, K. Asaka, N. Fujiwara, and K. Oguro, "The effects of counter ions on characterization and performance of a solid polymer electrolyte actuator," *Electrochimica Acta*, vol. 46, pp. 1233-1241, 2001.

[12] K. Asaka and K. Oguro, "Bending of polyelectrolyte membrane platinum composites by electric stimuli Part II. Response kinetics," *Journal of Electroanalytical Chemistry*, vol. 480, pp. 186-198, 2000.

[13] M. Shahinpoor and K. J. Kim, "Effects of Counter-Ions on the Performance of IPMCs," presented at Electroactive Polymer Actuators and Devices, Smart Structures and Materials, 2000.

[14] B. Henderson, S. Lane, M. Shahinpoor, K. J. Kim, and D. Leo, "Evaluation of Ionic Polymer-Metal Composites for Use as Near-DC Mechanical Sensors," presented at AIAA Space 2001-Conference and Exposition, Albuquerque, NM, 2001.

[15] N. Fujiwara, K. Asaka, Y. Nishimura, K. Oguro, and E. Torikai, "Preparation of Gold-Solid Polymer Electrolyte Composites as Electric Stimuli-Responsive Materials," *Chemistry of Materials*, vol. 12, pp. 1750-1754, 2000.

[16] M. Shahinpoor and K. J. Kim, "Ionic polymer-metal composites: I. Fundamentals " *Smart Materials and Structure*, vol. 10, pp. 819-833, 2001.

[17] M. Uchida and M. Taya, "Solid Polymer Electrolyte Actuator using Electrode Reaction," *Polymer*, vol. 42, pp. 9281-9285, 2001.

[18] K. Asaka and N. Fujiwara, "Electric deformation response of anion-exchange membrane/gold composites," *Electrochimica Acta*, vol. 48, pp. 3465-3471, 2003.

[19] W. Lu, A. G. Fadeev, B.Qi, B. R. Mattes, G. Wallace, J. Ding, G. Spinks, J. Mazurkiewicz, D.R.MacFarlane, S. Forsyth, and M. Forsyth, "Use of Ionic Liquids For π-Conjugated Polymer Electrochemical Devices," *Science*, vol. 297, pp. 983-987, 2002.

[20] M. D. Bennett and D. J. Leo, "Hybrid Actuation in Coupled Ionic/Conducting Polymer Devices," presented at Materials Research Society, 2004.

[21] M. D. Bennett, D. J. Leo, G. L. Wilkes, F. L. Beyer, and T. W. Pechar, "A model of charge transport and electromechanical transduction in ionic liquid-swollen Nafion membranes," *Polymer*, vol. 47, pp. 6782-6796, 2006.

[22] X. Bao, Y. Bar-Cohen, and S.-S. Lih, "Measurements and macro models of Ionomeric Polymer-Metal Composites (IPMC)," presented at Proceedings of the SPIE Smart Structures and Materials Symposium, EAPAD Conference, San Diego, 2002.

[23] E. T. Enikov and G. S. Seo, "Analysis of water and proton fluxes in ion-exchange polymer-metal composite (IPMC) actuators subjected to large external potentials," *Sensors and Actuators A: Physical*, vol. 122, pp. 264-272, 2005.

[24] C. Bonomo, L. Fortuna, S. Graziani, and D. Mazza, "A Circuit to Model an Ionic Polymer-Metal Composite as Actuator," presented at International Symposium Circuits and Systems, 2004.

[25] C. Bonomo, L. Fortuna, P. Giannone, and S. Graziani, "A circuit to model the electrical behavior of an ionic polymer-metal composite," *IEEE Transactions on Circuits and Systems--I: Fundamental Theory and Applications*, vol. 53, pp. 338-350, 2006.

[26] J. W. Paquette, K. J. Kim, J.-D. Nam, and Y. Tak, "An Equivalent Circuit Model for Ionic Polymer-Metal Composites and Their Performance Improvement by a Clay-Based Polymer Nano-Composite Technique," *Journal of Intelligent Materials Systems and Structures*, vol. 14, pp. 633-642, 2003.

[27] S. Tadokoro, "An Actuator Model of ICPF For Robotic Applications On the Basis of Physico-Chemical Hypothese," presented at IEEE, ICRA, 2000.

[28] S. Nemat-Nasser and J. Y. Li, "Electromechanical Response of Ionic Polymer Metal Composites," presented at Electroactive Polymer Actuators and Devices, Smart Structures and Materials, 2000.

[29] R. Kanno, A. Kurata, M. Hattori, S. Tadokoro, and T. Takamori, "Characteristics and Modeling of ICPF Actuator," presented at Japan-USA Symposium on Flexible Automation, 1994.
[30] M. Shahinpoor, "Electro-mechanics of Iono-elastic Beams as Electrically Controllable Artificial Muscles," presented at Electroactive Polymer Actuators and Devices, Smart Structures and Materials, 1999.
[31] K. M. Newbury and D. J. Leo, "Linear Electromechanical Model of Ionic Polymer Transducers -Part I: Model Development," *Journal of Intelligent Material Systems and Structures*, vol. 14, pp. 333-342, 2003.
[32] E. T. Enikov and B. J. Nelson, "Electrotransport and Deformation Model of Ion Exchange Membrane Based Actuators," presented at Electroactive Polymer Actuators and Devices, Smart Structures and Materials, 2000.
[33] Y. Xiao and K. Bhattacharya, "Modeling Electromechanical Properties of Ionic Polymers," presented at Electroactive Polymer Actuators and Devices, Smart Structures and Materials, 2001.
[34] S. Nemat-Nasser, "Micromechanics of Actuation of Ionic Polymer-metal Composites," *Journal of Applied Physics*, vol. 92, pp. 2899-2915, 2002.
[35] P. G. De Gennes, K. Okumura, M. Shahinpoor, and K. J. Kim, "Mechanoelectric Effects in Ionic Gels," *Europhysics Letters*, vol. 50, pp. 513-518, 2000.
[36] Y. Toi and S.-S. Kang, "Finite element analysis of two-dimensional electrochemical-mechanical response of ionic conducting polymer-metal composite beams," *Computers & Structures*, vol. 83, pp. 2573-2583, 2005.
[37] N. Walsby, S. Hietala, S. L. Maunu, F. Sundholm, T. Kallio, and G. Sundholm, "Water in Different Poly(styrene sulfonic acid)-Grafted Fluoropolymers," *Journal of Applied Polymer Science*, vol. 86, pp. 33-42, 2002.
[38] DuPont, "DuPont™ Nafion® PFSA Membranes N-112, NE-1135, N-115, N-117, NE-1110 perfluorosulfonic acid polymer," 2002.
[39] D. Nilsson, T. Kugler, P.-O. Svensson, and M. Berggren, "An all-organic sensor-transistor based on a novel electrochemical transducer concept printed electrochemical sensors on paper," *Sensors and Actuators B: Chemical*, vol. 86, pp. 193-197, 2002.
[40] S. C. Yeo and A. Eisenberg, "Physical Properties and Supermolecular Structure of Perfluorinated Ion-Containing (Nafion) Polymers,". *Journal of Applied Polymer Science,*, vol. 21, pp. 875-898, 1977.
[41] DuPont, "Nafion: Physical and Chemical Properties."
[42] M. R. Tant, K. A. Mauritz, and G. L. Wilkes, *Ionomers: Synthesis, Structure, Properties, and Applications*: Kluwer Academic Pub, 1997.
[43] A. Sacca, A. Carbone, R. Pedicini, G. Portale, L. D'Ilario, A. Longo, A. Martorana, and E. Passalacqua, "Structural and electrochemical investigation on re-cast Nafion membranes for polymer electrolyte fuel cells (PEFCs) application," *Journal of Membrane Science*, vol. 278, pp. 105-113, 2006.
[44] R. S. Yeo and H. L. Yeager, *Modern Aspects of Electrochemistry*. New York: Plenum Press, 1985.
[45] A. Katchalsky, "Rapid Swelling and Deswelling of Reversible Gels of Polymeric Acids by Ionization," *Experientia*, vol. 5, pp. 319-320, 1949.

[46] T. D. Gierke, G. E. Munn, and F. G. Wilson, "Morphology in Nafon Peruorinated Membrane Products, as Determined by Wide- and Small-angle X-ray Studies," presented at ACS Symposium Series, 180, 1982.
[47] T. A. Zawodzinski, M. Neeman, L. O. Sillerud, and S. Gottesfeld, "Detrmination of Water Diffusion Coefficients in Perfluorosulfonate Ionomeric Membranes," *Journal of Physical Chemistry*, vol. 95, pp. 6040-6044, 1991.
[48] J. Divisek, M. Eikerling, V. Mazin, H. Schmitz, U. Stimming, and Y. M. Volfkovich, "A Study of Capillary Porous Structure and Sorption Properties of Nafion Proton Exchange Membranes Swollen in Water," *Journal of Electrochemical Society*, vol. 145, pp. 2677-2683, 1998.
[49] T. A. Zawodzinski, C. Derouin, S. Radzinski, R. J. Sherman, and V. T. Smith, "Water Uptake by and Transport Through Nafion 117 Membranes," *Journal of the Electrochemical Society*, vol. 140, pp. 1041-1047, 1993.
[50] A. Havranek and K. Wippermann, "Determination of proton conductivity in anode catalyst layers of the direct methanol fuel cell (DMFC)," *Journal of Electroanalytical Chemistry*, vol. 567, pp. 305-315, 2004.
[51] S. Slade, S. A. Campbell, T. R. Ralph, and F. C. Walshc, "Ionic Conductivity of an Extruded Nafion 1100 EW Series of Membranes," *Journal of The Electrochemical Society*, vol. 149, pp. A1556-A1564, 2002.
[52] I. A. Levitsky, P. Kanelos, and W. B. Euler, "Electromechanical actuation of composite material from carbon nanotubes and ionomeric polymer," *Journal of Chemical physics*, vol. 121, pp. 1058-1065, 2004.
[53] S. J. Paddison, D. W. Reagor, and T. A. Zawodzinski, "High Frequency Dielectric Studies of Hydrated Nafion," *Journal of Electroanalytical Chemistry*, vol. 459, pp. 91-97, 1998.
[54] DuPont, "DuPont™ Teflon® PTFE 640 fluoropolymer resin," 2005.
[55] W. B. Floriano, "Dielectric Constant and Density of Water as a Function of Pressure at Constant Temperature," *Brazilian Journal of Physics*, vol. 34, pp. 38-41, 2004.
[56] T. D. Gierke, G. E. Munn, and F. C. Wilson, "The Morphology in Nafion Perfluorinated Membrane Products, as Determined by Wide-Angle and Small-Angle X-ray Studies," *Journal of Polymer Science, Polymer Physics Edition*, vol. 19, pp. 1687-1704, 1981.
[57] W. Y. Hsu and T. D. Gierke, "Ion transport and clustering in nafion perfluorinated membranes," *Journal of Membrane Science*, vol. 13, pp. 307-326, 1983.
[58] T. A. Davis, J. D. Genders, and D. Pletcher, *First Course in Ion Permeable Membranes*. Romsey, England Electrochemical Consultancy 1997.
[59] P. D. Beattie, F. P. Orfino, V. I. Basura, K. Zychowska, J. Ding, C. Chuy, J. Schmeisser, and S. Holdcroft, "Ionic conductivity of proton exchange membranes," *Journal of Electroanalytical Chemistry*, vol. 503, pp. 45-56, 2001.
[60] S. Mannino, M. Rossi, and S. Ratti, "Amperometric Detection of Sugars in Food at a Nafion-Copper Modified Electrode," *Electroanalysis*, vol. 3, pp. 711-714, 1991.

[61] O. I. Eriksen, E. Aksnes, and I. M. Dahl, "Facilitated transport of ethene through Nafion membranes. Part II. Glycerine treated, water swollen membranes," *Journal of Membrane Science*, vol. 85, pp. 99-106, 1993.

[62] Y.-L. Chen and T.-C. Chou, "Metals and Alloys Bonded on Solid Polymer Electrolyte for Electrochemical Reduction of Pure Benzaldehyde without Liquid Supporting Electrolyte," *Journal of Electroanalytical Chemistry*, vol. 360, pp. 247-259, 1993.

[63] K. Oguro, Fujiwara, N., Asaka, K., Onishi, K.,Sewa, S., "Polymer electrolyte actuator with gold electrodes " presented at Electroactive Polymer Actuators and Devices, Newport Beach, CA, 1999.

[64] H. Nakajima, Y. Takakuwa, H. Kikuchi, K. Fujikawa, and H. Kita, "Metal electrodes bonded on solid polymer electrolyte membranes (SPE)--IV. Morphological features and electrical resistance of Pt- and Au-SPE electrodes," *Electrochimica Acta*, vol. 32, pp. 791-798, 1987.

[65] P. Millet, M. Pineri, and R. Durand, "New Solid Polymer Electrolyte Composites for Water Electrolysis," *Journal of Applied Electrochemistry*, vol. 19, pp. 162-166, 1989.

[66] R. Jiang, Y. Zhang, S. Swier, X. Wei, C. Erkey, H. R. Kunz, and J. M. Fenton, "Preparation via Supercritical Fluid Route of Pd-Impregnated Nafion Membranes which Exhibit Reduced Methanol Crossover for DMFC," *Electrochemical and Solid-State Letters*, vol. 8, pp. A611-A615 2005.

[67] S. Parra, L. Henao, E. Mielczarski, J. Mielczarski, P. Albers, E. Suvorova, J. Guindet, and J. Kiwi, "Synthesis, Testing, and Characterization of a Novel Nafion Membrane with Superior Performance in Photoassisted Immobilized Fenton Catalysis " *Langmuir*, vol. 20, pp. 5621-5629, 2004.

[68] S. Sabhi and J. Kiwi, "Degradation of 2,4-dichlorophenol by immobilized iron catalysts," *Water Research*, vol. 35, pp. 1994-2002, 2001.

[69] B. J. Akle, M. D. Bennett, and D. J. Leo, "High-strain ionomeric-ionic liquid electroactive actuators," *Sensors and Actuators A: Physical*, vol. 126, pp. 173-181, 2006.

[70] P. Nandakumar, C. Vijayan, Y. v. G. S. Murti, K. Dhanalakshmi, and G. Sundararajan, "Proton exchange mechanism of synthesizing CdS quantum dots in Nafion," *Indian Journal of Pure and Applied Physics*, vol. 37, pp. 239-241, 1999.

[71] D. Pletcher and F. C. Walsh, *Industrial Electrochemistry*, 2 ed: Kluwer Academic, 1990.

[72] M. Shahinpoor and K. J. Kim, "Ionic Polymer-Metal Composites: III. Modeling and Simulation as Biomimetic Sensors, Actuators, Transducers, and Artificial Muscles," *Smart Materials and Structures*, vol. 13, pp. 1362–1388, 2004.

[73] P. S. Fedkiw and W. Her, "An Impregnation-Reduction Method to Prepare Electrodes on Nafion SPE," *Journal of Electrochemical Society*, vol. 136, pp. 899-900, 1989.

[74] M. W. Verbrugge, E. W. Schneider, R. S. Conell, and R. F. Hill, "The Effect of Temperature on the Equilibrium and Transport Properties of Saturated Poly(perfluorosulfonic acid) Membranes," *Journal of Electrochemical Society*, vol. 139, pp. 3421-3428, 1992.

[75] B. P. Block and J. C. Bailar, "The Reaction of Gold(III) with Some Bidentate Coordinating Groups," *Journal of American Chemistry Society*, vol. 73, pp. 4722-4725, 1951.
[76] K. J. Kim and M. Shahinpoor, "Ionic Polymer-Metal Composites - II. Manufacturing Techniques," *Smart Materials and Structures*, vol. 12, pp. 65-79, 2003.
[77] R. Liu, W. Her, and P. S. Fedkiw, "In situ electrode formation on a Nafion membrane by chemical platinization," *Journal of Electrochemical Society*, vol. 139, pp. 15-23, 1992.
[78] K. Onishi, S. Sewa, K. Asaka, N. Fujiwara, and K. Oguro, "Morphology of Electrodes and Bending Response of the Polymer Electrolyte Aactuator," *Electrochimica Acta*, vol. 46, pp. 737–743, 2000.
[79] H. Takenaka, E. Torikai, Y. Kawami, and N. Wakabayashi, "Solid Polymer Electrolytes Water Electrolysis," *The International Journal of Hydrogen Energy*, vol. 7, pp. 397, 1982.
[80] S. J. C. Cleghorn and J. A. Kolde., "Developing More Durable, Cost Effective MEAs," *Scientific Study*, 2002.
[81] R. A. Dunlap, *The Golden Ratio and Fibonacci Numbers* World Scientific Publishing Company 1998.
[82] Y. Kawano, Y. Wang, R. A. Palmer, and S. R. Aubuchon, "Stress-Strain Curves of Nafion Membranes in Acid and Salt Forms," *Polimeros: Ciencia e Tecnologia*, vol. 12, pp. 96-101, 2002.
[83] ASTM, "D 638: Standard test method for tensile properties of plastics," 2001.
[84] ASTM, "D 882: Standard test method for tensile properties of plastics sheeting," 2001.
[85] K. P. Menard, *Dynamic mechanical analysis: a practical introduction*. New York: CRC Press, 1999.
[86] K. J. Kim, D. Leo, J. Madden, Z. Ounaies, E. Smela, and D. F. Infante, "Standard Testing Methods for Extensional and Bending Electroactive Polymer Actuators," presented at ASME 2005 International Mechanical Engineering Congress and Exposition, Orlando, FL, 2005.
[87] B. Daniel and M. D. Ward, "Measurement of Interfacial Processes at Electrode Surfaces with the Electrochemical Quartz Crystal Microbalance," *Chemical Reviews*, vol. 92, pp. 1355-1379, 1992.
[88] M. Shahinpoor, "Ionic polymer-conductor composites as biomimetic sensors, robotic actuators and artificial muscles--a review," *Electrochimica Acta*, vol. 48, pp. 2343-2353, 2003.
[89] C. L. Petersen, T. M. Hansen, P. Boggild, A. Boisen, O. Hansen, T. Hassenkam, and F. Grey, "Scanning microscopic four-point conductivity probes," *Sensors and Actuators A: Physical*, vol. 96, pp. 53-58, 2002.
[90] J. T. Uan-Zo-li, "The Effects of Structure, Humidity and Aging on the Mechanical Properties of Polymeric Ionomersfor Fuel Cell Applications," in *Materials Science and Engineering*, vol. Master of science. Blacksburg, Virginia: Virginia Polytechnic Institute and State University, 2001.

[91] Y. Tang, A. M. Karlsson, M. H. Santare, M. Gilbert, S. Cleghorn, and W. B. Johnson, "An experimental investigation of humidity and temperature effects on the mechanical properties of perfluorosulfonic acid membrane," *Materials Science and Engineering: A*, vol. 425, pp. 297-304, 2006.
[92] H. B. Lee, G. Khang, and J. H. Lee, *The Biomedical Engineering Handbook*, 2 ed: CRC Press, 2000.
[93] S. de Almeida and Y. Kawano, "Thermal behavior of Nafion membranes," *Journal of Thermal Analysis and Calorimetry*, vol. 58, pp. 569-577, 1999.
[94] D. R. Lide, *CRC Handbook of Chemistry and Physics*, 84 ed: CRC Press, 2004.
[95] M. Ahmad, "Flexible Vinyl Resiliency Property Enhancement With Hollow Thermoplastic Microspheres," *Journal of Vinyl and Additive Technology*, vol. 7, pp. 156-161, 2001.
[96] A. J. Bard and L. R. Faulkner, *Electrochemical Methods: Fundamentals and Applications*, 2 ed. New York: Wiley, 2000.
[97] D. Kim, I. Jung, J. Lee, I. Oh, H. Ha, and Y. Tak, "Investigation of hydrogen adsorption behaviours in the presence of methanol and dissolved oxygen using electrochemical quartz crystal microbalance," *Electrochimica Acta*, vol. 50, pp. 693-697, 2004.
[98] D. Kim and K. J. Kim, "Experimental Investigation on Electrochemical Properties of Ionic Polymer-Metal Composite," *Journal of Intelligent Materials Systems and Structures* vol. 17, pp. 449-454 2006.
[99] J. R. Macdonald, *Impedance Spectroscopy: Emphasizing Solid Materials and Systems*: Wiley-Interscience, 1987.
[100] H. Ma, C. Liu, J. Liao, Y. Su, X. Xue, and W. Xing, "Study of ruthenium oxide catalyst for electrocatalytic performance in oxygen evolution," *Journal of Molecular Catalysis A: Chemical*, vol. 247, pp. 7-13, 2006.
[101] D. Harrington, "Stability and Inductive Behaviour in Electrochemical Impedance," presented at Corrosion and Prevention, 2000.
[102] J.-D. Kim, Y.-I. Park, K. Kobayashi, M. Nagai, and M. Kunimatsu, "Characterization of CO tolerance of PEMFC by ac impedance spectroscopy," *Solid State Ionics*, vol. 140, pp. 313-325, 2001.
[103] J. Bisquert, H. Randriamahazaka, and G. Garcia-Belmonte, "Inductive behaviour by charge-transfer and relaxation in solid-state electrochemistry," *Electrochimica Acta*, vol. 51, pp. 627-640, 2005.
[104] Y. Bar-Cohen, S. Leary, A. Yavrouian, K. Oguro, S. Tadokoro, J. Harrison, J. Smith, and J. Su, "Challenges to the Transition of IPMC Artificial Muscle Actuators to Practical Application," presented at MRS Symposium: FF: Electroactive Polymers, Boston, 1999.
[105] W. Yim, K. J. Kim, J. Paquette, and D. Kim, "Operation of Ionic Polymer-Metal Composites in Water," presented at SPIE: Smart Structures and Materials, San Diego, 2005.
[106] J. Paquette and K. J. Kim, "Ionomeric Electroactive Polymer Artificial Muscle for Naval Applications," *IEEE: Journal of Oceanic Engineering*, vol. 29, pp. 729-737, 2004.

[107] K. Mallavarapu, K. Newbury, and D. Leo, "Feedback Control of the Bending Response of Ionic Polymer-Metal Composite Actuators," presented at Electroactive Polymer Actuators and Devices, Smart Structures and Materials, 2001.
[108] Y. Bar-Cohen, *Electroactive polymer (EAP) actuators as artificial muscles - Reality, potential and challenges*: SPIE Press, 2001.
[109] H. Tamagawa, F. Nogata, and S. Popovic, "Roles of Ag redox reaction and water absorption inducing the Selemion bending," *Journal of Membrane Science*, vol. 251, pp. 145-150, 2005.
[110] H. Tamagawa and F. Nogata, "Bending response of dehydrated ion exchange polymer membranes to the applied voltage," *Journal of Membrane Science*, vol. 243, pp. 229-234, 2004.
[111] W. Xu, E. I. Cooper, and C. A. Angell, "Ionic Liquids:Ion Mobilities, Glass Temperatures, and Fragilities," *Journal of Physical Chemistry*, vol. 107, pp. 6170 -6178, 2003.
[112] K. A. Fletcher, S. Pandey, I. K. Storey, A. E. Hendricks, and S. Pandey, "Selective fluorescence quenching of polycyclic aromatic hydrocarbons by nitromethane within room temperature ionic liquid 1-butyl-3-methylimidazolium hexafluorophosphate," *Analytica Chimica Acta*, vol. 453, pp. 89-96, 2002.
[113] S. Carda-Broch, A. Berthod, and D. W. Armstrong, "Solvent properties of the 1-butyl-3-methylimidazolium hexafluorophosphate ionic liquid," *Analytical and Bioanalytical Chemistry*, vol. 375, pp. 191-199, 2003.
[114] P. K. Mandal, S. Saha, R. Karmakar, and A. Samanta, "Solvation dynamics in room temperature ionic liquids: Dynamic Stokes shift studies of fluorescence of dipolar molecules," *Current Science*, vol. 90, pp. 301-310, 2006.
[115] P. Bonhote, A. P. Dias, N. Papageorgiou, K. Kalyanasundaram, and M. Gratzel, "Hydrophobic, Highly Conductive Ambient-Temperature Molten Salts," *Inorg. Chem.*, vol. 35, pp. 1168-1178, 1996.
[116] J. Jacquemin, P. Husson, V. Majer, and M. F. C. Gomes, "Low-pressure solubilities and thermodynamics of solvation of eight gases in 1-butyl-3-methylimidazolium hexafluorophosphate," *Fluid Phase Equilibria*, vol. 240, pp. 87-95, 2006.
[117] Y. U. Paulechka, G. J. Kabo, A. V. Blokhin, O. A. Vydrov, J. W. Magee, and M. Frenkel, "Thermodynamic Properties of 1-Butyl-3-methylimidazolium Hexafluorophosphate in the Ideal Gas State," *Journal of Chemical & Engineering Data*, vol. 48, pp. 457-462, 2003.
[118] D. L. Compton and J. A. Laszlo, "Direct electrochemical reduction of hemin in imidazolium-based ionic liquids," *Journal of Electroanalytical Chemistry*, vol. 520, pp. 71-78, 2002.
[119] J. M. Gere, *Mechanics of Materials*, 5 ed. Pacific Grove: Brooks/Cole, 2001.
[120] J. Eskhult, M. Herranen, and L. Nyholm, "On the origin of the spontaneous potential oscillations observed during galvanostatic deposition of layers of Cu and Cu2O in alkaline citrate solutions," *Journal of Electroanalytical Chemistry*, vol. 594, pp. 35-49, 2006.

[121] B. Miller and A. Chen, "Oscillatory instabilities during the electrochemical oxidation of sulfide on a Pt electrode," *Journal of Electroanalytical Chemistry*, vol. 588, pp. 314-323, 2006.
[122] S. Malkhandi, A. Bonnefont, and K. Krischer, "Strictly potentiostatic current oscillations during bulk CO electro-oxidation on platinum in the presence of inhibiting anions," *Electrochemistry Communications*, vol. 7, pp. 710-716, 2005.
[123] Q.-K. Yu, Y. Miyakita, S. Nakabayashi, and R. Baba, "Magnetic field effect on electrochemical oscillations during iron dissolution," *Electrochemistry Communications*, vol. 5, pp. 321-324, 2003.
[124] S. Chen, D. Lee, and M. Schell, "Enhancement of the electrochemical oxidation of formic acid. Effects of anion adsorption and variation of rotation rate," *Electrochimica Acta*, vol. 46, pp. 3481-3492, 2001.
[125] T. J. Schmidt, B. N. Grgur, N. M. Markovic, and P. N. RossJr, "Oscillatory behavior in the electrochemical oxidation of formic acid on Pt(100): rotation and temperature effects," *Journal of Electroanalytical Chemistry*, vol. 500, pp. 36-43, 2001.
[126] J. Grzanna, H. Jungblut, and H. J. Lewerenz, "A model for electrochemical oscillations at the Si | electrolyte contact: Part I. Theoretical development," *Journal of Electroanalytical Chemistry*, vol. 486, pp. 181-189, 2000.
[127] J. Grzanna, H. Jungblut, and H. J. Lewerenz, "A model for electrochemical oscillations at the Si | electrolyte contact: Part II. Simulations and experimental results," *Journal of Electroanalytical Chemistry*, vol. 486, pp. 190-203, 2000.
[128] S. Chen, T. Noles, and M. Schell, "Effects of anions on chemical instabilities in the oxidation of formic acid," *Electrochemistry Communications*, vol. 2, pp. 171-174, 2000.
[129] M. Itagaki, T. Mori, and K. Watanabe, "Channel flow double electrode study on electrochemical oscillation during copper dissolution in acidic chloride solution," *Corrosion Science*, vol. 41, pp. 1955-1970, 1999.
[130] Y. Mukouyama, S. Nakanishi, H. Konishi, and Y. Nakato, "Electrochemical oscillations of a new type in an H_2O_2+H_2SO_4 | Pt-electrode system, appearing by addition of small amounts of halide ions," *Journal of Electroanalytical Chemistry*, vol. 473, pp. 156-165, 1999.
[131] D. H. Wang, F. X. Gan, and J. Y. Zou, "New electrochemical oscillations induced by the adsorption-desorption of organic corrosion inhibitor on Fe in H2SO4 solutions," *Electrochimica Acta*, vol. 43, pp. 2241-2244, 1998.
[132] S. Majoni and J. Janek, "Periodic electrochemical oscillations at a solid-solid electrode," *Solid State Ionics*, vol. 85, pp. 247-250, 1996.
[133] K. Krischer, M. Lubke, W. Wolf, M. Eiswirth, and G. Ertl, "Oscillatory dynamics of the electrochemical oxidation of H_2 in the presence of Cu^{2+}: Structure sensitivity and the role of anions," *Electrochimica Acta*, vol. 40, pp. 69-81, 1995.
[134] K. Krischer, "Spontaneous formation of spatiotemporal patterns at the electrode | electrolyte interface," *Journal of Electroanalytical Chemistry*, vol. 501, pp. 1-21, 2001.

[135] I. Jung, D. Kim, I. Oh, H. Ha, J. Lee, and Y. Tak, "Electrochemical Oscillations in the HCHO Oxidation on a Pt Electrode," *Journal of Industrial and Engineering Chemistry*, vol. 9, pp. 159-162, 2003.
[136] P. Strasser, M. Eiswirth, and G. Ertl, "Oscillatory Instabilities during Formic Acid Oxidation on Pt(100), Pt(110) and Pt(111) under Potentiostatic Control. II. Model Calculations," *Journal of Chemical Physics*, vol. 107, pp. 991-1003, 1997.
[137] H. Okamoto and N. Tanaka, "Potential Oscillation Mechanism for Formaldehyde Oxidation on Platinum," *Electrochimica Acta*, vol. 38, pp. 503-509, 1993.
[138] V. Kertész, G. Inzelt, C. Barbero, R. Kötz, and O. Haas, "Probe Beam Deflection Studies of Electrochemical Oscillations during Galvanostatic Oxidation of Formic Acid at a Platinum Electrode," *Journal of Electroanalytical Chemistry*, vol. 392, pp. 91-95, 1995.
[139] D. Kim, I. Jung, J. Lee, I. Oh, H. Ha, S. Hong, and Y. Tak, "Investigation of hydrogen adsorption behaviors in the presence of methanol and dissolved oxygen using electrochemical quartz crystal microbalance," *Electrochimica Acta*, vol. 50, pp. 693-697, 2004.
[140] S. Nakabayashi, I. Yagi, N. Sugiyama, K. Tamura, and K. Uosaki, "Reaction Pathway of Four-electron Oxidation of Formaldehyde on Platinum Electrode as Observed by in situ Optical Spectroscopy," *Surface Science*, vol. 386, pp. 82-88, 1997.
[141] T. E. Jackman, J. A. Davies, D. P. Jackson, W. N. Unertl, and P. R. Norton, "The Pt(110) phase Transition: A Study by Rutherford Backscattering, Nuclear Microanalysis, LEED and Thermal Desorption Spectroscopy," *Surface Science*, vol. 120, pp. 389, 1982.
[142] M. T. M. Koper, "Stability Study and Categorization of Electrochemical Oscillators by Impedance Spectroscopy," *Journal of Electroanalytical Chemistry*, vol. 409, pp. 175-182, 1996.
[143] J. W. Paquette, "Ionic Polymer-Metal Composites: Fabrication, Modeling, and Experimentation," vol. M.S. thesis: University of Nevada, Reno, 2003.
[144] R. R. Craig, Jr., *Mechanics of Materials* 2ed. NY: John Wiley & Sons, 2000.
[145] T. Belendez, M. Perez-Polo, C. Neipp, and A. Belendez, "Numerical and Experimental Analysis of Large Deflections of Cantilever Beams Under a Combined Load," *Physica Scripta.*, vol. T118, pp. 61-65, 2005.
[146] H. Tamagawa, K. Yagasaki, and F. Nogata, "Mechanical Charateristics of Ionic Polymer-Metal Composite in the processing of self-bending " *Journal of Applied Physics*, vol. 92, pp. 7614-7618, 2002.
[147] C. Bonomo, L. Fortuna, P. Giannone, and S. Graziani, "A Method to Characterize the Deformation of an IPMC Sensing Membrane," *Sensors and Actuator A: Physical*, vol. 123-124, pp. 146-154, 2005.
[148] K. J. Kim, J. W. Paquette, D. J. Leo, and K. M. Farinholt, *Ionic Polymer-Metal Composite for Sensory Applications, Encyclopedia of Sensors*: American Scientific Press 2006.
[149] E. Biddiss and T. Chau, "Electroactive polymeric sensors in hand prostheses: Bending response of an ionic polymer metal composite," *Medical Engineering & Physics*, vol. 28, pp. 568-578, 2006.

[150] K. Choe, "Polyacrylonitrile as an Actuator Material: Properties, Characterizations and Applications," in *Mechanical Engineering*, vol. MS thesis: University of Nevada, Reno, 2004.
[151] N. S. Nise, *Control Systems Engineering* Redwood City: The Benjamin/Cummings Publishing Company, 1995.
[152] H. Coleman and W. G. Steele, *Experimentation and Uncertainty Analysis for Engineers* John Wiley & Sons, 1989.
[153] Radiometer-Analytical, "Voltalab catalogue."
[154] Transducers-technique, "Product catalogue."
[155] Instron, "Certification of test (07-Apr-06)," 2006.
[156] TA-instruments, "Certificate of calibration (TACC-06-358)," 2006.
[157] Perkin-Elmer, "Product catalogue."

APPENDICES

Appendix A. Fabrication of IPMCs

1. Pretreatment of Nafion™

1) Clean the membrane in an ultrasonic water bath cleaner.

2) Immerse the membrane in DI water to swell the membrane.

3) Boil the membrane in 3 % H_2O_2 to remove organic impurities.

4) Rinse the membrane in DI water.

5) Boil the membrane in 1 M H_2SO_4 to eliminate the metallic impurities.

6) Final washing.

2. Metal Compositing/Coating Processes

Platinum-IPMC

1) Immerse a swollen membrane in 10 ~ 20 mM $Pt(NH_3)_4Cl_2 \cdot xH_2O$ solution.

2) Rinse the membrane with DI water and put in reducing solution in pH 9 ~ 10 (consisting of NH_4OH and $NaBH_4$) in a water bath.

3) Boil the IPMC in 1 M H_2SO_4 to ensure the complete elimination of basic impurities.

4) Rinse the IPMC in DI water.

5) (Optional process) put in reducing solution in pH 9 ~ 10 (consisting of $Pt(NH_3)_4Cl_2 \cdot xH_2O$, $H_2NOHHC1$, $H_2NNH_2.H_2O$, and NH_4OH).

6) Rinse the IPMC with DI water.

Gold-IPMC

1) Synthesis of Gold (III) dichloro phenanthroline [75]

2) Immerse a swollen membrane in 10 ~ 20 mM $[Au(phen)Cl_2]^+$ (Gold(III) dichloro phenanthroline).

3) Rinse the membrane with DI water and put in reducing solution in pH 6 ~ 7 (consisting of Na_2SO_3).

4) Rinse the IPMC with DI water.

Appendix B. Sensory Behavior of the IPMC

IPMC sensory systems have been extensively investigated due to their unique properties such as softness, light weight, and flexibility [4, 16, 147, 148]. IPMC systems can convert inner reaction energy to an electrical signal under an applied force. Electromechanical sensors systems can be potentially used in medical and industrial applications [149]. The IPMC sensor was mechanically deformed and vibrates using a rotary hammer connected to a controllable-speed DC motor which is driven by a power amplifier. The power supply amplifier (Techron Model 5507) was used to change the speeds of the DC motor. To acquire the sensing signal of the IPMC, an Op-Amp based-charge amplifier which converts short-circuit charge to a voltage output signal was used. The setup for the IPMC sensor is shown in Fig. B.1. Fig. B.2 shows the sensing output voltage of an IPMC and deflection for different thicknesses of the IPMC sample (10 mm wide x 50 mm long). Two different IPMC samples using Nafion™ 117 (0.2 mm thick) and Nafion™ 1110 (0.28 mm thick) were tested. The resulting data shown in Figure C.2 indicate that bending deflection decreases as the thickness of the sensor increases; conversely, as the thickness of the IPMC samples increases the bending deflection decreases as mentioned by prior works [24, 28, 147, 148]. Increasing the thickness of the sample, the mass of the sample increases, and, there is a decrease in the characteristic frequency and higher voltage outputs. Fig. B.3 shows a good linear relationship between the sensing output voltage and the velocity of bending for Nafion™ 117 and Nafion™ 1110. This linear relationship could indicate that an IPMC may be a good candidate as a reliable velocity sensor.

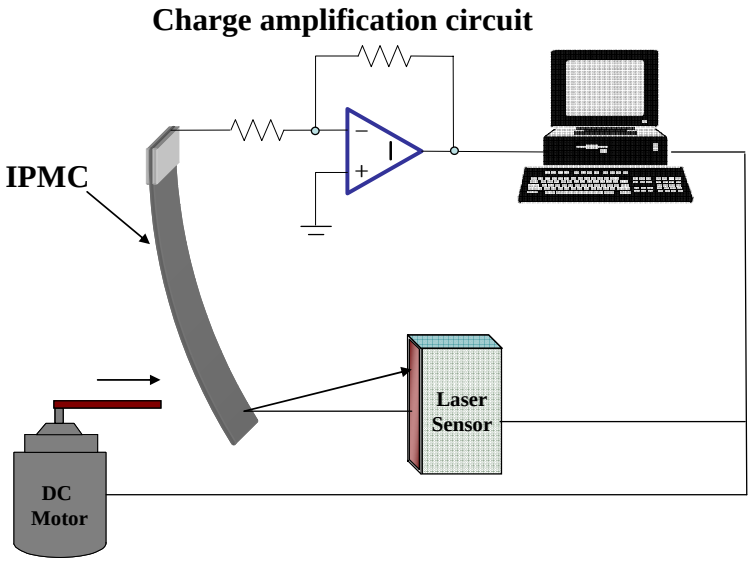

(a)

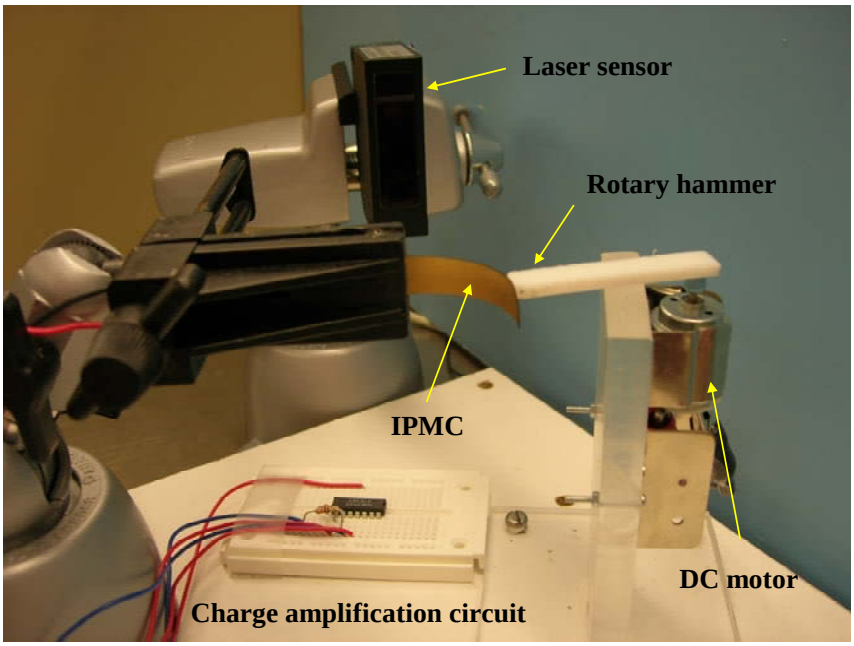

(b)

Fig. B.1. Schematic diagram (a) and experimental setup (b) for IPMC velocity sensing in air.

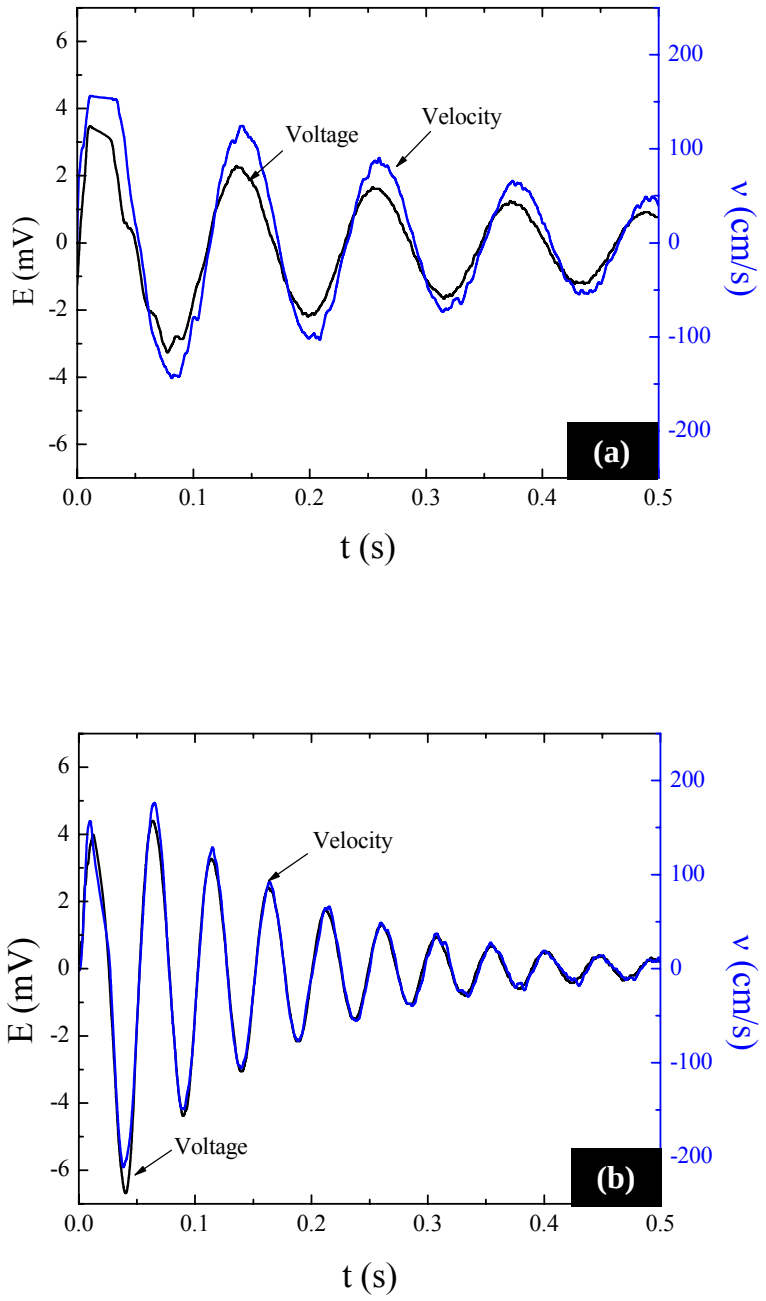

Fig. B.2. Sensing output and velocity of different thicknesses: Nafion™ 117 base platinum-IPMC (a) and Nafion™ 1110 based platinum-IPMC (b).

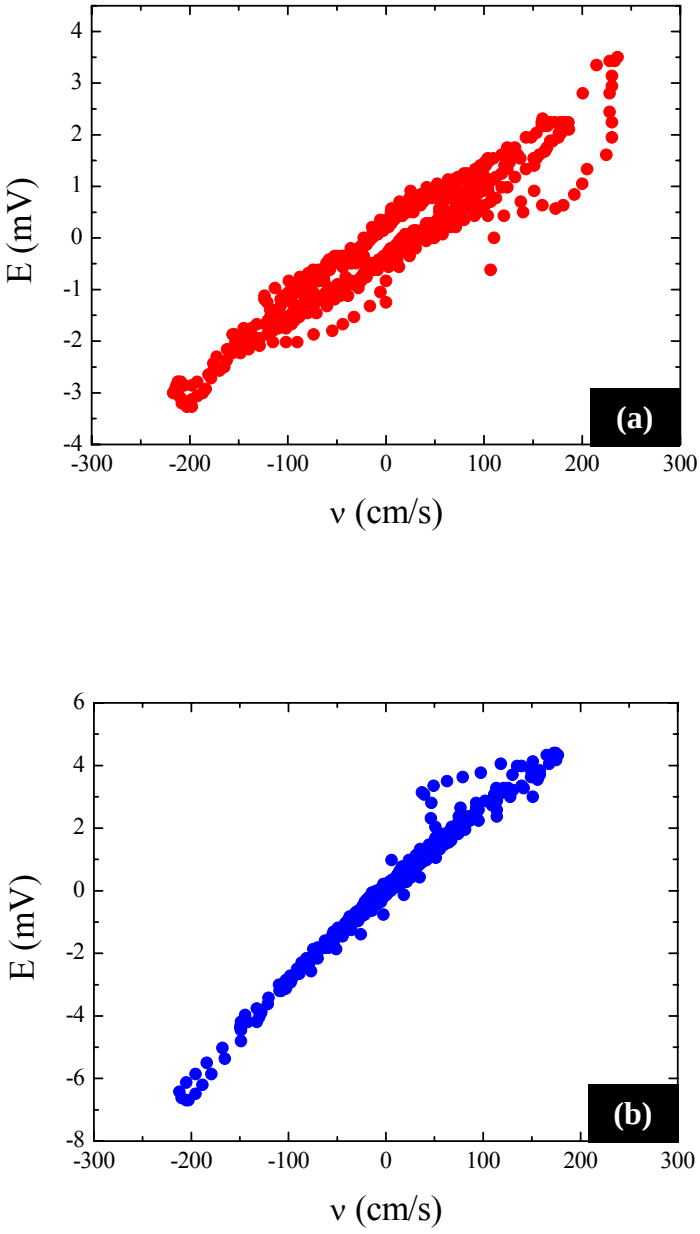

Fig. B.3. The relationship between the sensor output voltage and the velocity: Nafion™ 117 based platinum-IPMC (a) and Nafion™ 1110 based platinum-IPMC (b).

Appendix C. Summary of Performance Capability of IPMC Actuator

Comparing performance capability of IPMC actuator with traditional actuators is necessary to understand and to identify the IPMC actuator application. Performance characteristics of IPMC actuator used in this study provided in Fig. C.1 and Fig. C.2 where other actuator technologies are also described [150].

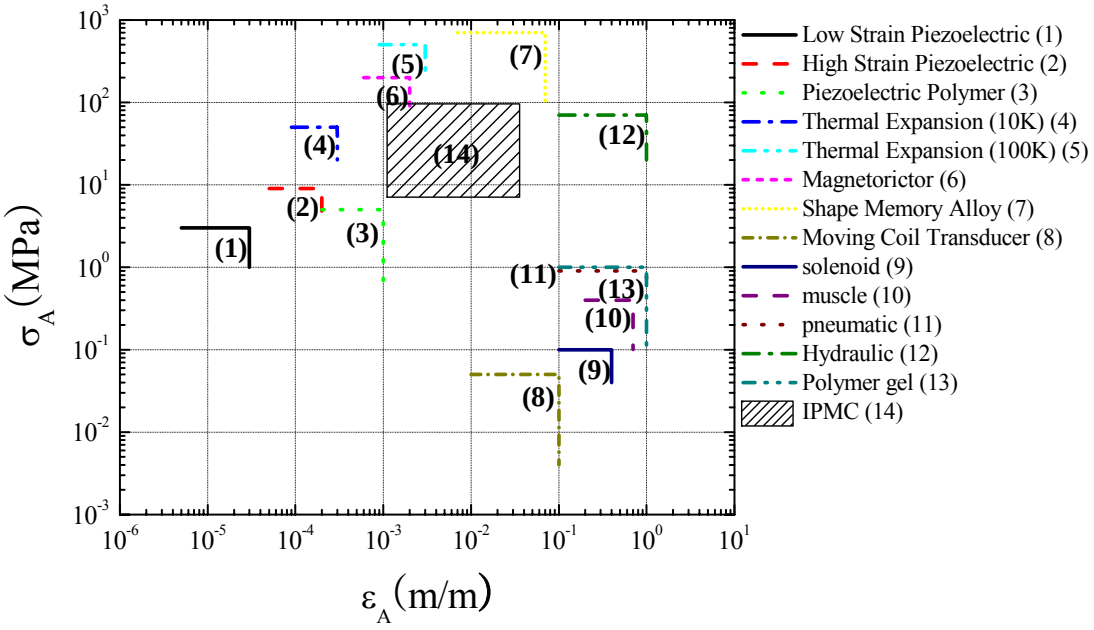

Fig. C.1. Actuation stress (σ) versus actuation strain (ε) for various actuators.

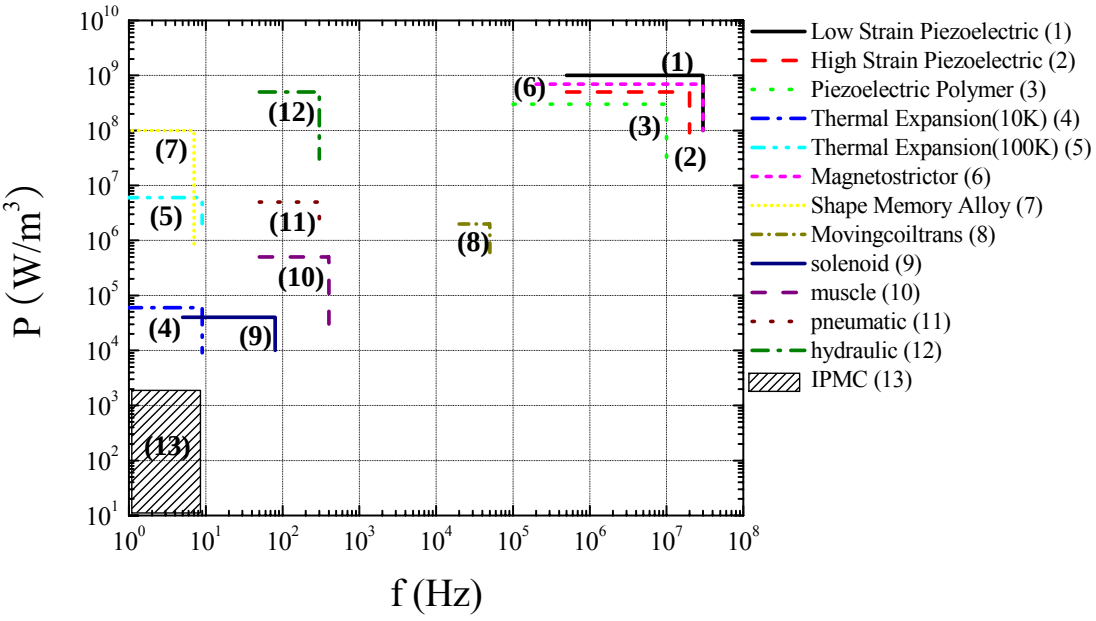

Fig. C.2. Volumetric power (P) versus frequency (f) for various actuators.

Appendix D. Matlab Code for the Proposed Models

Beam model

```
function beam
 clc;clear all;
 xx = [0 50];
v0 = [0 0];
[x,v] = ode23(@equ,xx,v0);
 ang=-(pi)/2;
xxx = cos(ang)*(x-0)-sin(ang)*(v(:,1)-0)+0;
yyy = sin(ang)*(x-0)+cos(ang)*(v(:,1)-0)+0;
figure(1)
plot(xxx,-yyy),axis([0 45 0 45]);,hold on
xlabel ('Horizontal Position (mm)')
ylabel ('Vertical Deflection (mm)')
%save text
fid = fopen('bmodelX.txt','wt');   %file name
fprintf(fid,'%f %f\n',xxx);
fclose(fid);
fid = fopen('bmodelY.txt','wt');   %file name
fprintf(fid,'%f %f\n',xxx);
fclose(fid);
disp('done')
```

```
function  x_dot = equ(x,v)
%Dimension of IPMC
L=40.5;                 %Length in milimeter
b=10;                   %Width in milimeter
hm=100e-6;              %Half of Thickness of Nafion in milimeter
hip=hm+10e-6;           %One side of Thickness of IPMC in milimeter
cmod=0.27;              %coefficient
%properties of Materials
Ee=169000;              %Elastic modulus in MPa of electrode
Em=50;                  %Elastic modulus in MPa of Nafion
%Equivalent circuit parameters
R1=10;
Re=50;
C1=0.02;
%Operation conditions
V=2;                    %volts
tau1=10;
%Equations
tau2=-(Re+2*R1)*tau1/(R1*C1*Re);
Q=V*((R1*C1)/(2*R1+Re))*(1-exp(tau2));
const = 3*alfa*Q*(hip+hm)/(2*b*L*(Ee*(hip^3-hm^3)+Em*hm^3));
x1 = v(1);
x2 = v(2);
```

```
x1_dot = x2;

x2_dot = ((1+x2^2)^(3/2))*const;

x_dot = [x1_dot x2_dot]';
```

Electrochemical oscillation model

```
function Chaotic_Oscillation_Systems

clc;clear all;clf

 x0 = 0.;

y0 = 0.;

e0 = 0.5;

tt = [0 180];

[t,xye] = ode15s(@diff_equ,tt,[x0 y0 e0]);

disp('Done')

figure(1)

plot(t,xye(:,3));

%save text

fid = fopen('smodelX.txt','wt');   %file name

fprintf(fid,'%f %f\n',vx);

fclose(fid);

fid = fopen('smodelY.txt','wt');   %file name

fprintf(fid,'%f %f\n',vy);

fclose(fid);

function diff_xye = diff_equ(t,xye)
```

```
x = xye(1);

y = xye(2);

e = xye(3);

%model parameter

i = 10;

j = 50.26;

a1 = 10;

a2 = -11;

a3 = 9;

a_3 = -9;

a4 = 20;

 e1 = 0.2;

e2 = 0.3;

e3 = 0.01;

e_3 = 0.512;

e4 = 0.77;

k1 = exp(a1*(e-e1));

k2 = exp(a2*(e-e2));

k3 = exp(a3*(e-e3));

k_3 = exp(a_3*(e-e_3));

k4 = exp(a4*(e-e4));

x_dot = (k2*(1-x-y) - k4*x*y);

y_dot = (k3*x*(1-x-y) - k_3*y - k4*x*y);
```

```
e_dot = (i - j*( k1*(1-x-y)+k4*x*y ));

diff_xye = [x_dot y_dot e_dot]';
```

Appendix E. Relationship of Electrical Components

Voltage, current, charge, impedance, and admittance relationship for capacitors, resistors, and inductors [151]

	Capacitor	Resistor	Inductor
Voltage-Current	$v(t) = \frac{1}{C}\int_0^t i(t)dt$	$v(t) = i(t)R$	$v(t) = L\frac{di(t)}{dt}$
Current-Voltage	$i(t) = C\frac{dv(t)}{dt}$	$i(t) = \frac{1}{R}v(t)$	$i(t) = \frac{1}{L}\int_0^t v(t)dt$
Voltage-Charge	$v(t) = \frac{1}{C}q(t)$	$v(t) = R\frac{dq(t)}{dt}$	$v(t) = L\frac{d^2q(t)}{dt^2}$
Impedance: Z(s)	$\frac{1}{Cs}$	R	Ls
Admittance: Y(s)	Cs	$\frac{1}{R} = G$	$\frac{1}{Ls}$

Appendix F. Error/Uncertainty Analysis

No measurement of a physical quantity can be entirely accurate. Most measurements are subject to more than one type of error. It is important to verify how much the measured value is likely to deviate from the unknown, true value of the quantity.

Image processing method

For the image processing method used in this study, the images that were taken by a CCD camera need to be processed to calculate the position of each target points marked on the IPMC. Most image file formats use 8 bits to store pixel values. To approximate the single data point for the centroid of the marker, the centroidal point was considered as the actual position of data. The image processing program calculated the centroid of the marker. The image data (pixel value) were scaled in SI unit using calibration

The root-sum-square (RSS) fundamentally assumes that all of the uncertainties have normal probability distributions that are all statistically independent. The total uncertainty in the strain measurement is determined using a standard RSS uncertainty analysis and can be can be represented by [152]

$$U_{RSS} = \left[\sum_{i=1}^{n} \left(\frac{\partial f}{\partial x_i} U_{x_i} \right)^2 \right]^{1/2} \qquad \text{(F.1)}$$

where, U_x is the measure of individual uncertainty

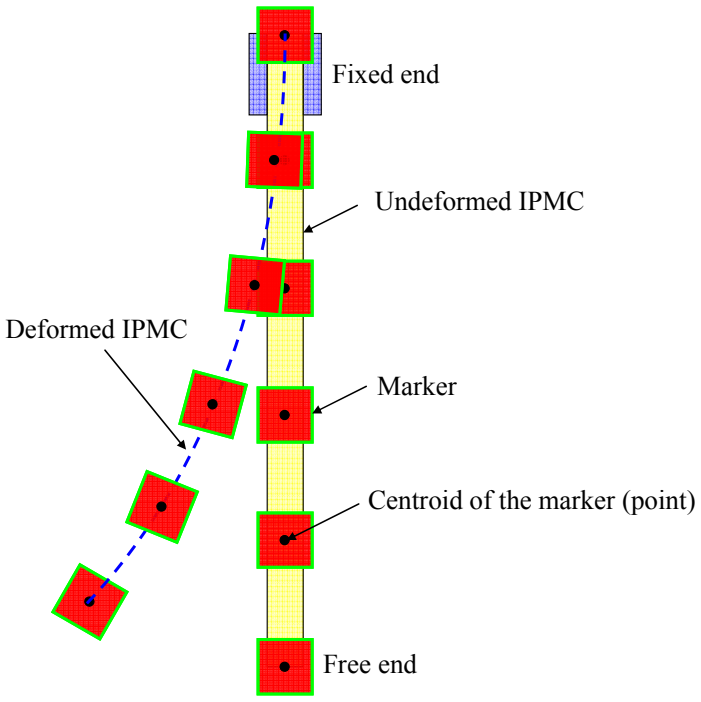

Fig. F.1. Image processing technique for marker tracking.

Tab. F.1. Experimental data for relationship between pixel and distance.

i	Pixel	mm/pixel
1	66	0.122727
2	68	0.119118
3	69	0.117391
4	69	0.117391
5	68	0.119118

$$\delta(mm) = 0.11915 \pm 0.00128\, pixel \qquad \text{(F.2)}$$

Thus total uncertainty in the deflection and the image processing method is as follows:

$$\left(\frac{\sigma_\delta}{\delta}\right)^2 = (9.74294 \times 10^{-4} / 0.11915)^2 = 6.69 * 10^{-5}$$

$$\frac{\sigma_\delta}{\delta} = 0.008177$$

where σ_δ is standard deviation of the deflection

The deflection measurement would have to be made with an uncertainty of less than 0.82%. Base on both of the uncertainty analysis and the calibration for this method, 100-pixel is equivalent to 11.915 mm length of actual object.

Other instruments

Specifications for major techniques used in this study are provided in Tab. F.2 ~ Tab. F.6.

Tab. F.2. Specifications of Voltalab 80 [153].

Voltammetry	Potential range	±4 V
	Current range	10 nA ~ 1 A
	Accuracy	±0.2 %
	Resolution	0.003 %
EIS	Frequency range	1mHz ~ 100kHz
	Accuracy	±0.5%
	Resolution	12.5 & 250 μV

Tab. F.3. Specifications of 10 g-load cell [154].

Nonlinearity	0.05%
Hysteresis	0.05%
Nonrepeatability	0.05%
Zero Balance	1.0%
Safe Overload	150 %
Deflection Inches	0.1 mm

Tab. F.4. Specifications of 100 N-load cell for Instron™ 5565 [155].

Accuracy	±0.35 %
Uncertainty of applied force	0.0661 %

Tab. F.5. Specifications of DSC Q10 [156].

Repeatability value of T	±1.5˚C
Repeatability value of ΔH	±2.0 J/g

Tab. F.6. Specifications of Pyris Diamond DMA [157].

Measurement Range	10^5 ~ 10^{12} Pa
Temperature Range	-150 ~ 600˚C
Scanning Rate	0.01 ~ 20˚C /min
Maximum Load	Static: ±10 N Dynamic: ±8 N
Frequency	Sine Wave Oscillation: 0.01 ~ 100 Hz